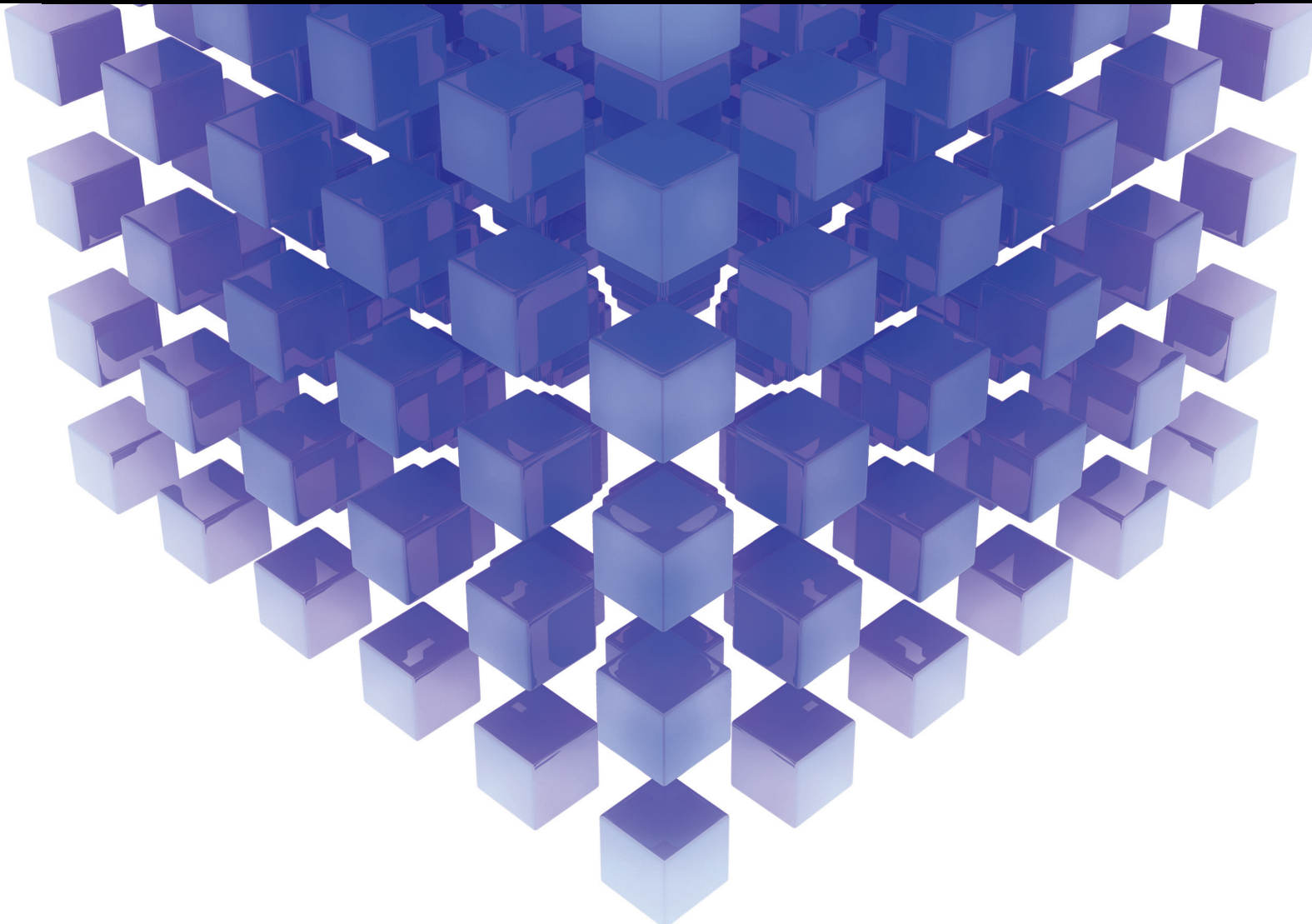


Trends in Analysis and Design of Nonlinear Control Systems with Applications to Engineering Problems 2021

Lead Guest Editor: Raúl Villafuerte-Segura

Guest Editors: Baltazar Aguirre-Hernández, Rosalba Galván-Guerra, and
Manuel Arias-Montiel



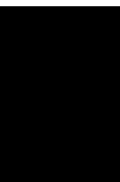


**Trends in Analysis and Design of Nonlinear
Control Systems with Applications to
Engineering Problems 2021**

Mathematical Problems in Engineering

**Trends in Analysis and Design of
Nonlinear Control Systems with
Applications to Engineering Problems
2021**


Lead Guest Editor: Raúl Villafuerte-Segura
Guest Editors: Baltazar Aguirre-Hernández,
Rosalba Galván-Guerra, and Manuel Arias-Montiel



Copyright © 2022 Hindawi Limited. All rights reserved.

This is a special issue published in “Mathematical Problems in Engineering.” All articles are open access articles distributed under the Creative Commons Attribution License, which permits unrestricted use, distribution, and reproduction in any medium, provided the original work is properly cited.

Chief Editor

Guangming Xie , China

Academic Editors

Kumaravel A , India
Waqas Abbasi, Pakistan
Mohamed Abd El Aziz , Egypt
Mahmoud Abdel-Aty , Egypt
Mohammed S. Abdo, Yemen
Mohammad Yaghoub Abdollahzadeh
Jamalabadi , Republic of Korea
Rahib Abiyev , Turkey
Leonardo Acho , Spain
Daniela Addessi , Italy
Arooj Adeel , Pakistan
Waleed Adel , Egypt
Ramesh Agarwal , USA
Francesco Aggogeri , Italy
Ricardo Aguilar-Lopez , Mexico
Afaq Ahmad , Pakistan
Naveed Ahmed , Pakistan
Elias Aifantis , USA
Akif Akgul , Turkey
Tareq Al-shami , Yemen
Guido Ala, Italy
Andrea Alaimo , Italy
Reza Alam, USA
Osamah Albahri , Malaysia
Nicholas Alexander , United Kingdom
Salvatore Alfonzetti, Italy
Ghous Ali , Pakistan
Nouman Ali , Pakistan
Mohammad D. Aliyu , Canada
Juan A. Almendral , Spain
A.K. Alomari, Jordan
José Domingo Álvarez , Spain
Cláudio Alves , Portugal
Juan P. Amezcua-Sanchez, Mexico
Mukherjee Amitava, India
Lionel Amodeo, France
Sebastian Anita, Romania
Costanza Arico , Italy
Sabri Arik, Turkey
Fausto Arpino , Italy
Rashad Asharabi , Saudi Arabia
Farhad Aslani , Australia
Mohsen Asle Zaem , USA

Andrea Avanzini , Italy
Richard I. Avery , USA
Viktor Avrutin , Germany
Mohammed A. Awadallah , Malaysia
Francesco Aymerich , Italy
Sajad Azizi , Belgium
Michele Baccocchi , Italy
Seungik Baek , USA
Khaled Bahlali, France
M.V.A Raju Bahubalendruni, India
Pedro Balaguer , Spain
P. Balasubramaniam, India
Stefan Balint , Romania
Ines Tejado Balsera , Spain
Alfonso Banos , Spain
Jerzy Baranowski , Poland
Tudor Barbu , Romania
Andrzej Bartoszewicz , Poland
Sergio Baselga , Spain
S. Caglar Baslamisli , Turkey
David Bassir , France
Chiara Bedon , Italy
Azeddine Beghdadi, France
Andriette Bekker , South Africa
Francisco Beltran-Carbajal , Mexico
Abdellatif Ben Makhlof , Saudi Arabia
Denis Benasciutti , Italy
Ivano Benedetti , Italy
Rosa M. Benito , Spain
Elena Benvenuti , Italy
Giovanni Berselli, Italy
Michele Betti , Italy
Pietro Bia , Italy
Carlo Bianca , France
Simone Bianco , Italy
Vincenzo Bianco, Italy
Vittorio Bianco, Italy
David Bigaud , France
Sardar Muhammad Bilal , Pakistan
Antonio Bilotta , Italy
Sylvio R. Bistafa, Brazil
Chiara Boccaletti , Italy
Rodolfo Bontempo , Italy
Alberto Borboni , Italy
Marco Bortolini, Italy

Paolo Boscariol, Italy
Daniela Boso , Italy
Guillermo Botella-Juan, Spain
Abdesselem Boulkroune , Algeria
Boulaïd Boulkroune, Belgium
Fabio Bovenga , Italy
Francesco Braghin , Italy
Ricardo Branco, Portugal
Julien Bruchon , France
Matteo Bruggi , Italy
Michele Brun , Italy
Maria Elena Bruni, Italy
Maria Angela Butturi , Italy
Bartłomiej Błachowski , Poland
Dhanamjayulu C , India
Raquel Caballero-Águila , Spain
Filippo Cacace , Italy
Salvatore Caddemi , Italy
Zuowei Cai , China
Roberto Caldelli , Italy
Francesco Cannizzaro , Italy
Maosen Cao , China
Ana Carpio, Spain
Rodrigo Carvajal , Chile
Caterina Casavola, Italy
Sara Casciati, Italy
Federica Caselli , Italy
Carmen Castillo , Spain
Inmaculada T. Castro , Spain
Miguel Castro , Portugal
Giuseppe Catalanotti , United Kingdom
Alberto Cavallo , Italy
Gabriele Cazzulani , Italy
Fatih Vehbi Celebi, Turkey
Miguel Cerrolaza , Venezuela
Gregory Chagnon , France
Ching-Ter Chang , Taiwan
Kuei-Lun Chang , Taiwan
Qing Chang , USA
Xiaoheng Chang , China
Prasenjit Chatterjee , Lithuania
Kacem Chehdi, France
Peter N. Cheimets, USA
Chih-Chiang Chen , Taiwan
He Chen , China
























Kebing Chen , China
Mengxin Chen , China
Shyi-Ming Chen , Taiwan
Xizhong Chen , Ireland
Xue-Bo Chen , China
Zhiwen Chen , China
Qiang Cheng, USA
Zeyang Cheng, China
Luca Chiapponi , Italy
Francisco Chicano , Spain
Tirivanhu Chinyoka , South Africa
Adrian Chmielewski , Poland
Seongim Choi , USA
Gautam Choubey , India
Hung-Yuan Chung , Taiwan
Yusheng Ci, China
Simone Cinquemani , Italy
Roberto G. Citarella , Italy
Joaquim Ciurana , Spain
John D. Clayton , USA
Piero Colajanni , Italy
Giuseppina Colicchio, Italy
Vassilios Constantoudis , Greece
Enrico Conte, Italy
Alessandro Contento , USA
Mario Cools , Belgium
Gino Cortellessa, Italy
Carlo Cosentino , Italy
Paolo Crippa , Italy
Erik Cuevas , Mexico
Guozeng Cui , China
Mehmet Cunkas , Turkey
Giuseppe D'Aniello , Italy
Peter Dabnichki, Australia
Weizhong Dai , USA
Zhifeng Dai , China
Purushothaman Damodaran , USA
Sergey Dashkovskiy, Germany
Adiel T. De Almeida-Filho , Brazil
Fabio De Angelis , Italy
Samuele De Bartolo , Italy
Stefano De Miranda , Italy
Filippo De Monte , Italy

José António Fonseca De Oliveira
Correia , Portugal
Jose Renato De Sousa , Brazil
Michael Defoort, France
Alessandro Della Corte, Italy
Laurent Dewasme , Belgium
Sanku Dey , India
Gianpaolo Di Bona , Italy
Roberta Di Pace , Italy
Francesca Di Puccio , Italy
Ramón I. Diego , Spain
Yannis Dimakopoulos , Greece
Hasan Dinçer , Turkey
José M. Domínguez , Spain
Georgios Dounias, Greece
Bo Du , China
Emil Dumic, Croatia
Madalina Dumitriu , United Kingdom
Premraj Durairaj , India
Saeed Eftekhari Azam, USA
Said El Kafhali , Morocco
Antonio Elipse , Spain
R. Emre Erkmen, Canada
John Escobar , Colombia
Leandro F. F. Miguel , Brazil
FRANCESCO FOTI , Italy
Andrea L. Facci , Italy
Shahla Faisal , Pakistan
Giovanni Falsone , Italy
Hua Fan, China
Jianguang Fang, Australia
Nicholas Fantuzzi , Italy
Muhammad Shahid Farid , Pakistan
Hamed Faruqi, Iran
Yann Favennec, France
Fiorenzo A. Fazzolari , United Kingdom
Giuseppe Fedele , Italy
Roberto Fedele , Italy
Baowei Feng , China
Mohammad Ferdows , Bangladesh
Arturo J. Fernández , Spain
Jesus M. Fernandez Oro, Spain
Francesco Ferrise, Italy
Eric Feulvarch , France
Thierry Floquet, France

















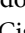








Eric Florentin , France
Gerardo Flores, Mexico
Antonio Forcina , Italy
Alessandro Formisano, Italy
Francesco Franco , Italy
Elisa Francomano , Italy
Juan Frausto-Solis, Mexico
Shujun Fu , China
Juan C. G. Prada , Spain
HECTOR GOMEZ , Chile
Matteo Gaeta , Italy
Mauro Gaggero , Italy
Zoran Gajic , USA
Jaime Gallardo-Alvarado , Mexico
Mosè Gallo , Italy
Akemi Gálvez , Spain
Maria L. Gandarias , Spain
Hao Gao , Hong Kong
Xingbao Gao , China
Yan Gao , China
Zhiwei Gao , United Kingdom
Giovanni Garcea , Italy
José García , Chile
Harish Garg , India
Alessandro Gasparetto , Italy
Stylianos Georgantzinou, Greece
Fotios Georgiades , India
Parviz Ghadimi , Iran
Ştefan Cristian Gherghina , Romania
Georgios I. Giannopoulos , Greece
Agathoklis Giaralis , United Kingdom
Anna M. Gil-Lafuente , Spain
Ivan Giorgio , Italy
Gaetano Giunta , Luxembourg
Jefferson L.M.A. Gomes , United Kingdom
Emilio Gómez-Déniz , Spain
Antonio M. Gonçalves de Lima , Brazil
Qunxi Gong , China
Chris Goodrich, USA
Rama S. R. Gorla, USA
Veena Goswami , India
Xunjie Gou , Spain
Jakub Grabski , Poland

Antoine Grall , France
George A. Gravvanis , Greece
Fabrizio Greco , Italy
David Greiner , Spain
Jason Gu , Canada
Federico Guarracino , Italy
Michele Guida , Italy
Muhammet Gul , Turkey
Dong-Sheng Guo , China
Hu Guo , China
Zhaoxia Guo, China
Yusuf Gurefe, Turkey
Salim HEDDAM , Algeria
ABID HUSSANAN, China
Quang Phuc Ha, Australia
Li Haitao , China
Petr Hájek , Czech Republic
Mohamed Hamdy , Egypt
Muhammad Hamid , United Kingdom
Renke Han , United Kingdom
Weimin Han , USA
Xingsi Han, China
Zhen-Lai Han , China
Thomas Hanne , Switzerland
Xinan Hao , China
Mohammad A. Hariri-Ardebili , USA
Khalid Hattaf , Morocco
Defeng He , China
Xiao-Qiao He, China
Yanchao He, China
Yu-Ling He , China
Ramdane Hedjar , Saudi Arabia
Jude Hemanth , India
Reza Hemmati, Iran
Nicolae Herisanu , Romania
Alfredo G. Hernández-Díaz , Spain
M.I. Herreros , Spain
Eckhard Hitzer , Japan
Paul Honeine , France
Jaromir Horacek , Czech Republic
Lei Hou , China
Yingkun Hou , China
Yu-Chen Hu , Taiwan
Yunfeng Hu, China
Can Huang , China
Gordon Huang , Canada
Linsheng Huo , China
Sajid Hussain, Canada
Asier Ibeas , Spain
Orest V. Iftime , The Netherlands
Przemyslaw Ignaciuk , Poland
Giacomo Innocenti , Italy
Emilio Insfran Pelozo , Spain
Azeem Irshad, Pakistan
Alessio Ishizaka, France
Benjamin Ivorra , Spain
Breno Jacob , Brazil
Reema Jain , India
Tushar Jain , India
Amin Jajarmi , Iran
Chiranjibe Jana , India
Łukasz Jankowski , Poland
Samuel N. Jator , USA
Juan Carlos Jáuregui-Correa , Mexico
Kandasamy Jayakrishna, India
Reza Jazar, Australia
Khalide Jbilou, France
Isabel S. Jesus , Portugal
Chao Ji , China
Qing-Chao Jiang , China
Peng-fei Jiao , China
Ricardo Fabricio Escobar Jiménez , Mexico
Emilio Jiménez Macías , Spain
Maolin Jin, Republic of Korea
Zhuo Jin, Australia
Ramash Kumar K , India
BHABEN KALITA , USA
MOHAMMAD REZA KHEDMATI , Iran
Viacheslav Kalashnikov , Mexico
Mathiyalagan Kalidass , India
Tamas Kalmar-Nagy , Hungary
Rajesh Kaluri , India
Jyotheeswara Reddy Kalvakurthi, India
Zhao Kang , China
Ramani Kannan , Malaysia
Tomasz Kapitaniak , Poland
Julius Kaplunov, United Kingdom
Konstantinos Karamanos, Belgium
Michal Kawulok, Poland

Irfan Kaymaz , Turkey
Vahid Kayvanfar , Qatar
Krzysztof Kecik , Poland
Mohamed Khader , Egypt
Chaudry M. Khalique , South Africa
Mukhtaj Khan , Pakistan
Shahid Khan , Pakistan
Nam-Il Kim, Republic of Korea
Philipp V. Kiryukhantsev-Korneev ,
Russia
P.V.V Kishore , India
Jan Koci , Czech Republic
Ioannis Kostavelis , Greece
Sotiris B. Kotsiantis , Greece
Frederic Kratz , France
Vamsi Krishna , India
Edyta Kucharska, Poland
Krzysztof S. Kulpa , Poland
Kamal Kumar, India
Prof. Ashwani Kumar , India
Michal Kunicki , Poland
Cedrick A. K. Kwuimy , USA
Kyandoghere Kyamakya, Austria
Ivan Kyrchei , Ukraine
Márcio J. Lacerda , Brazil
Eduardo Lalla , The Netherlands
Giovanni Lancioni , Italy
Jaroslaw Latalski , Poland
Hervé Laurent , France
Agostino Lauria , Italy
Aimé Lay-Ekuakille , Italy
Nicolas J. Leconte , France
Kun-Chou Lee , Taiwan
Dimitri Lefebvre , France
Eric Lefevre , France
Marek Lefik, Poland
Yaguo Lei , China
Kauko Leiviskä , Finland
Ervin Lenzi , Brazil
ChenFeng Li , China
Jian Li , USA
Jun Li , China
Yueyang Li , China
Zhao Li , China































Zhen Li , China
En-Qiang Lin, USA
Jian Lin , China
Qibin Lin, China
Yao-Jin Lin, China
Zhiyun Lin , China
Bin Liu , China
Bo Liu , China
Heng Liu , China
Jianxu Liu , Thailand
Lei Liu , China
Sixin Liu , China
Wanquan Liu , China
Yu Liu , China
Yuanchang Liu , United Kingdom
Bonifacio Llamazares , Spain
Alessandro Lo Schiavo , Italy
Jean Jacques Loiseau , France
Francesco Lolli , Italy
Paolo Lonetti , Italy
António M. Lopes , Portugal
Sebastian López, Spain
Luis M. López-Ochoa , Spain
Vassilios C. Loukopoulos, Greece
Gabriele Maria Lozito , Italy
Zhiguo Luo , China
Gabriel Luque , Spain
Valentin Lychagin, Norway
YUE MEI, China
Junwei Ma , China
Xuanlong Ma , China
Antonio Madeo , Italy
Alessandro Magnani , Belgium
Toqeer Mahmood , Pakistan
Fazal M. Mahomed , South Africa
Arunava Majumder , India
Sarfranz Nawaz Malik, Pakistan
Paolo Manfredi , Italy
Adnan Maqsood , Pakistan
Muazzam Maqsood, Pakistan
Giuseppe Carlo Marano , Italy
Damijan Markovic, France
Filipe J. Marques , Portugal
Luca Martinelli , Italy
Denizar Cruz Martins, Brazil

Francisco J. Martos , Spain
Elio Masciari , Italy
Paolo Massioni , France
Alessandro Mauro , Italy
Jonathan Mayo-Maldonado , Mexico
Pier Luigi Mazzeo , Italy
Laura Mazzola, Italy
Driss Mehdi , France
Zahid Mehmood , Pakistan
Roderick Melnik , Canada
Xiangyu Meng , USA
Jose Merodio , Spain
Alessio Merola , Italy
Mahmoud Mesbah , Iran
Luciano Mescia , Italy
Laurent Mevel , France
Constantine Michailides , Cyprus
Mariusz Michta , Poland
Prankul Middha, Norway
Aki Mikkola , Finland
Giovanni Minafò , Italy
Edmondo Minisci , United Kingdom
Hiroyuki Mino , Japan
Dimitrios Mitsotakis , New Zealand
Ardashir Mohammadzadeh , Iran
Francisco J. Montáns , Spain
Francesco Montefusco , Italy
Gisele Mophou , France
Rafael Morales , Spain
Marco Morandini , Italy
Javier Moreno-Valenzuela , Mexico
Simone Morganti , Italy
Caroline Mota , Brazil
Aziz Moukrim , France
Shen Mouquan , China
Dimitris Mourtzis , Greece
Emiliano Mucchi , Italy
Taseer Muhammad, Saudi Arabia
Ghulam Muhiuddin, Saudi Arabia
Amitava Mukherjee , India
Josefa Mula , Spain
Jose J. Muñoz , Spain
Giuseppe Muscolino, Italy
Marco Mussetta , Italy

Hariharan Muthusamy, India
Alessandro Naddeo , Italy
Raj Nandkeolyar, India
Keivan Navaie , United Kingdom
Soumya Nayak, India
Adrian Neagu , USA
Erivelton Geraldo Nepomuceno , Brazil
AMA Neves, Portugal
Ha Quang Thinh Ngo , Vietnam
Nhon Nguyen-Thanh, Singapore
Papakostas Nikolaos , Ireland
Jelena Nikolic , Serbia
Tatsushi Nishi, Japan
Shanzhou Niu , China
Ben T. Nohara , Japan
Mohammed Nouari , France
Mustapha Nourelfath, Canada
Kazem Nouri , Iran
Ciro Núñez-Gutiérrez , Mexico
Włodzimierz Ogryczak, Poland
Roger Ohayon, France
Krzysztof Okarma , Poland
Mitsuhiro Okayasu, Japan
Murat Olgun , Turkey
Diego Oliva, Mexico
Alberto Olivares , Spain
Enrique Onieva , Spain
Calogero Orlando , Italy
Susana Ortega-Cisneros , Mexico
Sergio Ortobelli, Italy
Naohisa Otsuka , Japan
Sid Ahmed Ould Ahmed Mahmoud , Saudi Arabia
Taoreed Owolabi , Nigeria
EUGENIA PETROPOULOU , Greece
Arturo Pagano, Italy
Madhumangal Pal, India
Pasquale Palumbo , Italy
Dragan Pamučar, Serbia
Weifeng Pan , China
Chandan Pandey, India
Rui Pang, United Kingdom
Jürgen Pannek , Germany
Elena Panteley, France
Achille Paolone, Italy

George A. Papakostas , Greece
Xosé M. Pardo , Spain
You-Jin Park, Taiwan
Manuel Pastor, Spain
Pubudu N. Pathirana , Australia
Surajit Kumar Paul , India
Luis Payá , Spain
Igor Pažanin , Croatia
Libor Pekař , Czech Republic
Francesco Pellicano , Italy
Marcello Pellicciari , Italy
Jian Peng , China
Mingshu Peng, China
Xiang Peng , China
Xindong Peng, China
Yuexing Peng, China
Marzio Pennisi , Italy
Maria Patrizia Pera , Italy
Matjaz Perc , Slovenia
A. M. Bastos Pereira , Portugal
Wesley Peres, Brazil
F. Javier Pérez-Pinal , Mexico
Michele Perrella, Italy
Francesco Pesavento , Italy
Francesco Petrini , Italy
Hoang Vu Phan, Republic of Korea
Lukasz Pieczonka , Poland
Dario Piga , Switzerland
Marco Pizzarelli , Italy
Javier Plaza , Spain
Goutam Pohit , India
Dragan Poljak , Croatia
Jorge Pomares , Spain
Hiram Ponce , Mexico
Sébastien Poncet , Canada
Volodymyr Ponomaryov , Mexico
Jean-Christophe Ponsart , France
Mauro Pontani , Italy
Sivakumar Poruran, India
Francesc Pozo , Spain
Aditya Rio Prabowo , Indonesia
Anchasa Pramuanjaroenkij , Thailand
Leonardo Primavera , Italy
B Rajanarayan Prusty, India

Krzysztof Puszynski , Poland
Chuan Qin , China
Dongdong Qin, China
Jianlong Qiu , China
Giuseppe Quaranta , Italy
DR. RITU RAJ , India
Vitomir Racic , Italy
Carlo Rainieri , Italy
Kumbakonam Ramamani Rajagopal, USA
Ali Ramazani , USA
Angel Manuel Ramos , Spain
Higinio Ramos , Spain
Muhammad Afzal Rana , Pakistan
Muhammad Rashid, Saudi Arabia
Manoj Rastogi, India
Alessandro Rasulo , Italy
S.S. Ravindran , USA
Abdolrahman Razani , Iran
Alessandro Reali , Italy
Jose A. Reinoso , Spain
Oscar Reinoso , Spain
Haijun Ren , China
Carlo Renno , Italy
Fabrizio Renno , Italy
Shahram Rezapour , Iran
Ricardo Rianza , Spain
Francesco Riganti-Fulginei , Italy
Gerasimos Rigatos , Greece
Francesco Ripamonti , Italy
Jorge Rivera , Mexico
Eugenio Roanes-Lozano , Spain
Ana Maria A. C. Rocha , Portugal
Luigi Rodino , Italy
Francisco Rodríguez , Spain
Rosana Rodríguez López, Spain
Francisco Rossomando , Argentina
Jose de Jesus Rubio , Mexico
Weiguo Rui , China
Rubén Ruiz , Spain
Ivan D. Rukhlenko , Australia
Dr. Eswaramoorthi S. , India
Weichao SHI , United Kingdom
Chaman Lal Sabharwal , USA
Andrés Sáez , Spain

Bekir Sahin, Turkey
Laxminarayan Sahoo , India
John S. Sakellariou , Greece
Michael Sakellariou , Greece
Salvatore Salamone, USA
Jose Vicente Salcedo , Spain
Alejandro Salcido , Mexico
Alejandro Salcido, Mexico
Nunzio Salerno , Italy
Rohit Salgotra , India
Miguel A. Salido , Spain
Sinan Salih , Iraq
Alessandro Salvini , Italy
Abdus Samad , India
Sovan Samanta, India
Nikolaos Samaras , Greece
Ramon Sancibrian , Spain
Giuseppe Sanfilippo , Italy
Omar-Jacobo Santos, Mexico
J Santos-Reyes , Mexico
José A. Sanz-Herrera , Spain
Musavarah Sarwar, Pakistan
Shahzad Sarwar, Saudi Arabia
Marcelo A. Savi , Brazil
Andrey V. Savkin, Australia
Tadeusz Sawik , Poland
Roberta Sburlati, Italy
Gustavo Scaglia , Argentina
Thomas Schuster , Germany
Hamid M. Sedighi , Iran
Mijanur Rahaman Seikh, India
Tapan Senapati , China
Lotfi Senhadji , France
Junwon Seo, USA
Michele Serpilli, Italy
Silvestar Šesnić , Croatia
Gerardo Severino, Italy
Ruben Sevilla , United Kingdom
Stefano Sfarra , Italy
Dr. Ismail Shah , Pakistan
Leonid Shaikhet , Israel
Vimal Shanmuganathan , India
Prayas Sharma, India
Bo Shen , Germany
Hang Shen, China

Xin Pu Shen, China
Dimitri O. Shepelsky, Ukraine
Jian Shi , China
Amin Shokrollahi, Australia
Suzanne M. Shontz , USA
Babak Shotorban , USA
Zhan Shu , Canada
Angelo Sifaleras , Greece
Nuno Simões , Portugal
Mehakpreet Singh , Ireland
Piyush Pratap Singh , India
Rajiv Singh, India
Seralathan Sivamani , India
S. Sivasankaran , Malaysia
Christos H. Skiadas, Greece
Konstantina Skouri , Greece
Neale R. Smith , Mexico
Bogdan Smolka, Poland
Delfim Soares Jr. , Brazil
Alba Sofi , Italy
Francesco Soldovieri , Italy
Raffaele Solimene , Italy
Yang Song , Norway
Jussi Sopanen , Finland
Marco Spadini , Italy
Paolo Spagnolo , Italy
Ruben Specogna , Italy
Vasilios Spitas , Greece
Ivanka Stamova , USA
Rafał Stanisławski , Poland
Miladin Stefanović , Serbia
Salvatore Strano , Italy
Yakov Strelniker, Israel
Kangkang Sun , China
Qiuqin Sun , China
Shuaishuai Sun, Australia
Yanchao Sun , China
Zong-Yao Sun , China
Kumarasamy Suresh , India
Sergey A. Suslov , Australia
D.L. Suthar, Ethiopia
D.L. Suthar , Ethiopia
Andrzej Swierniak, Poland
Andras Szekrenyes , Hungary
Kumar K. Tamma, USA






Yong (Aaron) Tan, United Kingdom
Marco Antonio Taneco-Hernández , Mexico
Lu Tang , China
Tianyou Tao, China
Hafez Tari , USA
Alessandro Tasora , Italy
Sergio Teggi , Italy
Adriana del Carmen Téllez-Anguiano , Mexico
Ana C. Teodoro , Portugal
Efstathios E. Theotokoglou , Greece
Jing-Feng Tian, China
Alexander Timokha , Norway
Stefania Tomasiello , Italy
Gisella Tomasini , Italy
Isabella Torricollo , Italy
Francesco Tornabene , Italy
Mariano Torrisi , Italy
Thang nguyen Trung, Vietnam
George Tsiatas , Greece
Le Anh Tuan , Vietnam
Nerio Tullini , Italy
Emilio Turco , Italy
Ilhan Tuzcu , USA
Efstratios Tzirtzilakis , Greece
FRANCISCO UREÑA , Spain
Filippo Ubertini , Italy
Mohammad Uddin , Australia
Mohammad Safi Ullah , Bangladesh
Serdar Ulubeyli , Turkey
Mati Ur Rahman , Pakistan
Panayiotis Vafeas , Greece
Giuseppe Vairo , Italy
Jesus Valdez-Resendiz , Mexico
Eusebio Valero, Spain
Stefano Valvano , Italy
Carlos-Renato Vázquez , Mexico
Martin Velasco Villa , Mexico
Franck J. Vernerey, USA
Georgios Veronis , USA
Vincenzo Vespri , Italy
Renato Vidoni , Italy
Venkatesh Vijayaraghavan, Australia

Anna Vila, Spain
Francisco R. Villatoro , Spain
Francesca Vipiana , Italy
Stanislav Vitek , Czech Republic
Jan Vorel , Czech Republic
Michael Vynnycky , Sweden
Mohammad W. Alomari, Jordan
Roman Wan-Wendner , Austria
Bingchang Wang, China
C. H. Wang , Taiwan
Dagang Wang, China
Guoqiang Wang , China
Huaiyu Wang, China
Hui Wang , China
J.G. Wang, China
Ji Wang , China
Kang-Jia Wang , China
Lei Wang , China
Qiang Wang, China
Qingling Wang , China
Weiwei Wang , China
Xinyu Wang , China
Yong Wang , China
Yung-Chung Wang , Taiwan
Zhenbo Wang , USA
Zhibo Wang, China
Waldemar T. Wójcik, Poland
Chi Wu , Australia
Qihong Wu, China
Yuqiang Wu, China
Zhibin Wu , China
Zhizheng Wu , China
Michalis Xenos , Greece
Hao Xiao , China
Xiao Ping Xie , China
Qingzheng Xu , China
Binghan Xue , China
Yi Xue , China
Joseph J. Yame , France
Chuanliang Yan , China
Xinggang Yan , United Kingdom
Hongtai Yang , China
Jixiang Yang , China
Mijia Yang, USA
Ray-Yeng Yang, Taiwan

Zaoli Yang , China
Jun Ye , China
Min Ye , China
Luis J. Yebra , Spain
Peng-Yeng Yin , Taiwan
Muhammad Haroon Yousaf , Pakistan
Yuan Yuan, United Kingdom
Qin Yuming, China
Elena Zaitseva , Slovakia
Arkadiusz Zak , Poland
Mohammad Zakwan , India
Ernesto Zambrano-Serrano , Mexico
Francesco Zammori , Italy
Jessica Zangari , Italy
Rafal Zdunek , Poland
Ibrahim Zeid, USA
Nianyin Zeng , China
Junyong Zhai , China
Hao Zhang , China
Haopeng Zhang , USA
Jian Zhang , China
Kai Zhang, China
Lingfan Zhang , China
Mingjie Zhang , Norway
Qian Zhang , China
Tianwei Zhang , China
Tongqian Zhang , China
Wenyu Zhang , China
Xianming Zhang , Australia
Xuping Zhang , Denmark
Yinyan Zhang, China
Yifan Zhao , United Kingdom
Debao Zhou, USA
Heng Zhou , China
Jian G. Zhou , United Kingdom
Junyong Zhou , China
Xueqian Zhou , United Kingdom
Zhe Zhou , China
Wu-Le Zhu, China
Gaetano Zizzo , Italy
Mingcheng Zuo, China


Contents

Optimal Position Fuzzy Control of an Underactuated Robotic Finger

Francisco J. Espinosa Garcia , Esther Lugo-González , Arturo Telléz-Velázquez , Manuel Arias-Montiel , and Marco Ceccarelli 






Research Article (12 pages), Article ID 2091337, Volume 2022 (2022)

SPMSM Sensorless Control System Based on ASMO

Yu Cao  and Chuang Liu





Research Article (11 pages), Article ID 6196321, Volume 2022 (2022)

A Novel Family of Exact Nonlinear Cascade Control Design Solutions for a Class of UAV Systems

Kristian Maya-Gress , Jorge Álvarez , Raúl Villafuerte-Segura , Hugo Romero-Trejo , and Miguel Bernal 

Research Article (15 pages), Article ID 2622571, Volume 2021 (2021)

Controlling the PVTOL Aircraft System with an Inverted Pendular Load by means of Nested Saturation Functions and GPI Controller

Cesar Alejandro Villaseñor Rios , Octavio Gutiérrez-Frías , Carlos Aguilar-Ibanez , and Miguel S. Suarez-Castanon 

Research Article (19 pages), Article ID 2295417, Volume 2021 (2021)

Analysis of Dynamic Characteristics of Tristable Piezoelectric Energy Harvester Based on the Modified Model

Dawei Man, Deheng Xu, Xingchen Kuang, Xiaofang Kang , Qinghu Xu, and Yu Zhang

Research Article (12 pages), Article ID 3832406, Volume 2021 (2021)

Research Article

Optimal Position Fuzzy Control of an Underactuated Robotic Finger

Francisco J. Espinosa Garcia ^{1,2}, Esther Lugo-González ³, Arturo Telléz-Velázquez ⁴,
Manuel Arias-Montiel ³ and Marco Ceccarelli ²

¹Postgraduate Division, Technological University of the Mixteca, Huajuapán de León 69000, Mexico

²LARM 2, University of Rome Tor Vergata, Rome 00133, Italy

³Institute of Electronics and Mechatronics, Technological University of the Mixteca, Huajuapán de León 69000, Mexico

⁴Institute of Computing, Technological University of the Mixteca, Huajuapán de León 69000, Mexico

Correspondence should be addressed to Manuel Arias-Montiel; mam@mixteco.utm.mx

Received 18 March 2022; Revised 27 May 2022; Accepted 28 June 2022; Published 20 July 2022

Academic Editor: Ardashir Mohammadzadeh

Copyright © 2022 Francisco J. Espinosa Garcia et al. This is an open access article distributed under the Creative Commons Attribution License, which permits unrestricted use, distribution, and reproduction in any medium, provided the original work is properly cited.

In this paper, the optimal position control of an underactuated robotic finger is presented. Two trajectories, one for the proximal and the other for the medial phalanx, are proposed in order to emulate the finger's flexion/extension movements. A Mandani fuzzy control is proposed due to the lack of a precise dynamical model of the system. In order to obtain the control parameters, an optimization strategy based on the membership functions is applied. Genetic algorithms (GA) are commonly used as an optimization method in diverse applications; however, in this case, the use of an autoadaptive differential evolution method is proposed in order to obtain a superior convergence behavior. Simulations of the virtual prototype are carried out using MATLAB/Simulink software to display the trajectory tracking. The results show that the maximum error between the proposed and obtained trajectories is $3.1352E - 04$ rad.

1. Introduction

Currently, control development for robotic hands continues to be a topic of interest as researchers seek to recreate human hand interaction with their environment when developing prototypes and their interaction with the environment. This objective is difficult to achieve due to the challenging nature of controlling robotic hands, as they are relatively complex mechatronic systems, which allow the user to hold, manipulate, and make use of different objects and tools. As a possible solution, some researchers have focused on improving control tasks in order to generate a robust grasp to reliably hold any object. In addition, the selection criteria of actuators are an important factor because the size, weight, and torque are variables that must be considered. Generally, the control systems have a closed-loop structure, since they seek to reduce errors so that the hand finger can maintain a specific desired position [1, 2], by using pneumatic [3–5] and

touch [6–8] sensors. In the literature, the most common control schemes are the proportional-integral-derivative (PID) control [9–11] and fuzzy control [12–14]. Controllers based on fuzzy logic are an alternative solution that does not require a mathematical model such as the PID [15]. A fuzzy logic controller (FLC) is a heuristic approach composed of a rules base proposed by the designer. The FLC is a nonlinear system with a knowledge based on fuzzy If-Then rules, and in most cases, the fuzzy rules are proposed by an expert who knows the process. In order to generate an output, membership functions are used to specify the degree of membership based on inputs. FLC must have a flexible behavior to adapt to various situations, as well as being robust to maintain the state of the desired output. The implementation of FLC is fairly common for solving problems, where (a) the systems are partially defined, (b) systems with variables that cannot be measured, and (c) system with large disturbances [12, 14, 16]. The principal fuzzy systems are Mandani and

Takagi-Sugeno. In particular, the Mandani systems use various techniques that allow fuzzy set membership function tuning, such as genetic algorithms (GA) [16], adaptive neural networks [17, 18], artificial bee colony optimization [19–21], ant colony optimization [22–24], and evolutionary algorithms [25–27].

Recently, fuzzy logic systems have been combined with nonlinear approaches in order to obtain adaptive control systems. Zhang et al. [28] proposed an FLC combined with sliding-mode technique for controlling underactuated systems. The authors provided a detailed stability analysis and a numerical example of a nonspecified system to prove the performance of the closed-loop system. However, the fuzzy system is not optimized. Li et al. [29] combined a fuzzy logic system with a back-stepping controller and a fuzzy state observer to solve the tracking problem for a class of uncertain nonlinear systems with unmodeled dynamics and disturbances. The stability of the systems is proven to be input-to-state practically stable based on the small-gain theorem, but the fuzzy logic system's membership functions are not optimized. Chang et al. [30] presented an adaptive fuzzy tracking control for a class of pure feedback and switched nonlinear systems with unknown gain. The authors did not provide details on the fuzzy system, such as the procedure to determine the membership functions.

Optimization methods have helped with the complex task of finding the appropriate parameter values and structure for the fuzzy systems. The most used algorithms for fuzzy systems optimization are GA because they are considered as global optimizers, unlike derivative methods that have the disadvantage of being prone to local minimum stagnation. They are also considered as good optimizers because of the existence of a population of potential solutions, which may be used to discard several local minima, meaning that there is a higher probability of finding the global minimum [31]. Several proposals search for optimal membership function parameters. For example, in [32] the authors proposed a methodology for optimizing a fuzzy controller for the speed of a permanent magnet synchronous motor (PMSM) without expert knowledge. For this approach, 14 variables are used for the optimization, 5 for the rule base parameters, 6 for the membership functions, and 3 for the scaling factors. A method for automatically generating fuzzy rules is presented for a system with 25 fuzzy rules needed, and each rule needs 3 bits [33]. A fuzzy controller applied to the wellhead back pressure control systems is optimized through the membership function, control rules, quantization, and scaling factors. The parameters are error, rate, scale, integral, and differential scale factors [34]. Despite this, there are other methods, such as the differential evolution (DE), which have more advantages compared to GA, one example being that they are more effective at searching for numerical problems and finding the optimum global solution [35, 36].

Motivated by the limitations of GA and other optimization methods, this paper presents the implementation of an auto adaptive differential evolution algorithm (AADE) [37] for optimizing the parameters of a fuzzy logic controller (FLC) for an underactuated robotic finger in order to track

the trajectory that represents the flexion-extension finger movements. This optimization algorithm does not require gradient information, which means that the optimization problem does not need to be differentiable. In addition, AADE is based on symmetrical discourses and fuzzy normalized systems, and the parameters F (factor scale) and Cr (crossover constant) show evidence of self-adaptation during the evolution phase, unlike GA or classical differential evolution (DE) algorithms, increasing its power and execution.

The remainder of this paper is organized as follows. In Section 1, a brief description of the prototype is presented. In Section 2, the development of the FLC and the application of AADE for parameter optimization is described. In Section 3, details of the numerical implementation of the optimized FLC are provided. Final remarks and some proposed future works for this research are given in Section 4.

2. Materials and Methods

2.1. Prototype Design. The robotic hand AMH-II (anthropomorphic metamorphic hand), originally presented in [38], has four fingers, all of which have three joints except for the thumb. The index, middle, and ring fingers are powered by an underactuated mechanism in order to use a single motor, thereby reducing the weight of the finger. This configuration allows the hand to perform the flexion/extension finger movements. The thumb has three joints, although only two of them are used for the flexion/extension movements, while the other one is used for the rotational movement. Details on the design and kinematic analysis of the AMH-II are presented in [38]. The virtual prototype is shown in Figure 1, and as can be observed, each finger has two motors to control movement. The motors employed are Pololu micromotors 100:1360 RPM 6V, and the joints are connected to these motors through a transmission system comprised of a worm-gear mechanism. The palm, unlike other robotics hands, can be moved through a motor fixed at the joint of the link, where the fingers are located and the link, where the thumb is located (thumb motor). Table 1 shows the ranges of motion for flexion/extension movements of the hand, corresponding to each finger joint (except for the thumb). Similarly, the movement measurements and ranges of the phalanges of the presented prototype are also shown.

2.2. Implemented Controller. For the control system, a Mandani fuzzy system was implemented, which includes a micro-motor that controls the position of the fingers. The transfer function corresponding to the servo motor used was obtained from [39].

$$G(s) = \frac{V(s)}{\theta(s)} = \frac{24}{s^2 + 24s + 10}, \quad (1)$$

where $V(s)$ is the input voltage applied to the motor, while $\theta(s)$ is the rotor position in radians (rads) after applying a specific voltage. This value is used as feedback as shown in the schematic diagram in Figure 2.

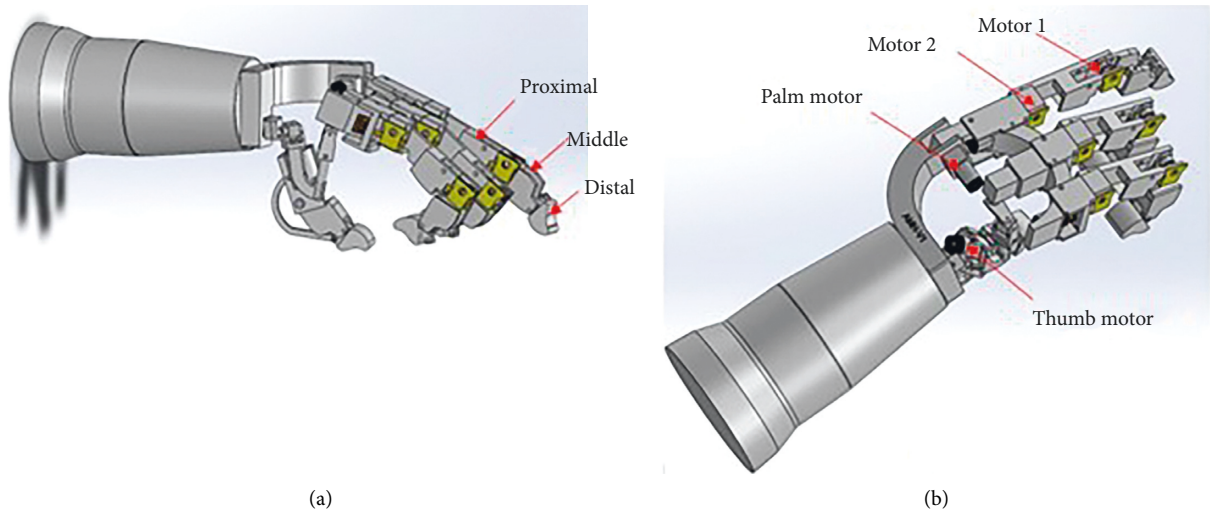


FIGURE 1: AMH-1: (a) phalanges of the hand and (b) motors' position.

TABLE 1: Ranges for flexion/extension movements comparison.

Phalanx	Length of the prototype (mm)	Range of human hand movement	Range of prototype movements
Distal (index and middle)	14	0–90°	0–85°
Middle (index and middle)	38.16	0–90°	0–75°
Proximal (index and middle)	41.89	0–90°	0–75°

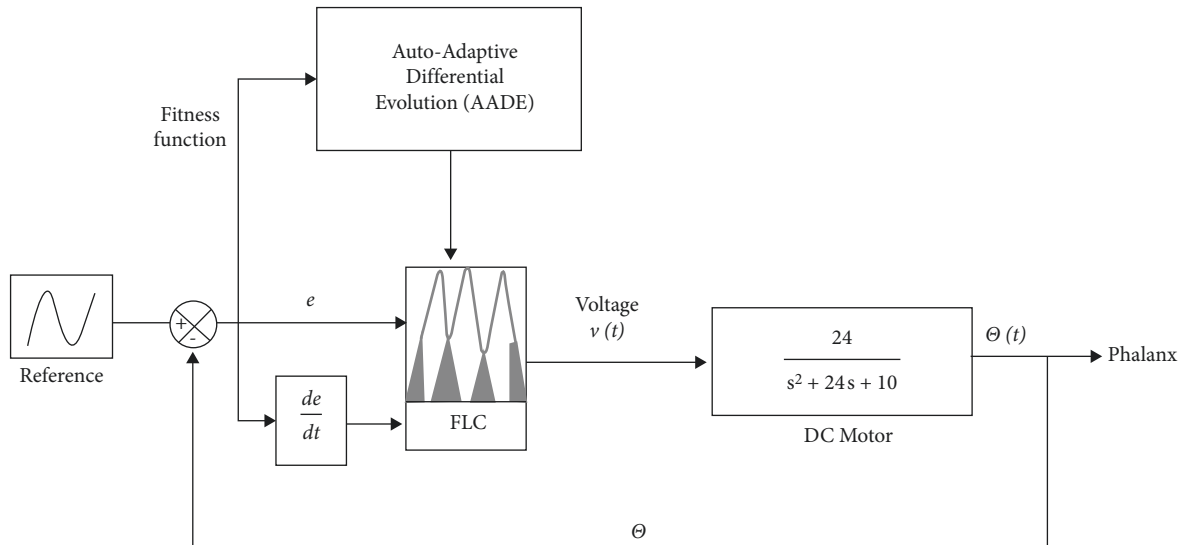


FIGURE 2: Block diagram of the control system.

The reference block represents the desired trajectory, while e and de are the error signal and its derivative, respectively, which serve as inputs for the fuzzy logic controller (FLC). This block sends a voltage signal to the motor block and its position is evaluated by the AADE so that the membership function parameters are changed to reduce the error.

The fuzzy system has three variables, error (e) and error change (c) are the inputs, and voltage (v) is the system output. Moreover, the variables have their own discourse universe range (Table 2) [37]. The configuration of the fuzzy

TABLE 2: Ranges for the fuzzy system.

Variable	Discourse ranges
Position error e	$[0, (\pi/2)]$
Error change c	$[0, (\pi/6)]$
Voltage v	$[-8.19, 8.19]$

system is established in 9 rules as shown in Table 3. Symbols NE, ZE, and PE are the linguistic terms for “negative error,” “zero error,” and “positive error”; NC, ZC, and PC are the linguistic terms for “negative change,” “zero change,” and

TABLE 3: Rules set.

Voltage	NC	ZC	PC
Position error			
NE	NV ⁽¹⁾	NV ⁽²⁾	PV ⁽³⁾
ZE	NV ⁽⁴⁾	ZV ⁽⁵⁾	PV ⁽⁶⁾
PE	PV ⁽⁷⁾	PV ⁽⁸⁾	PV ⁽⁹⁾

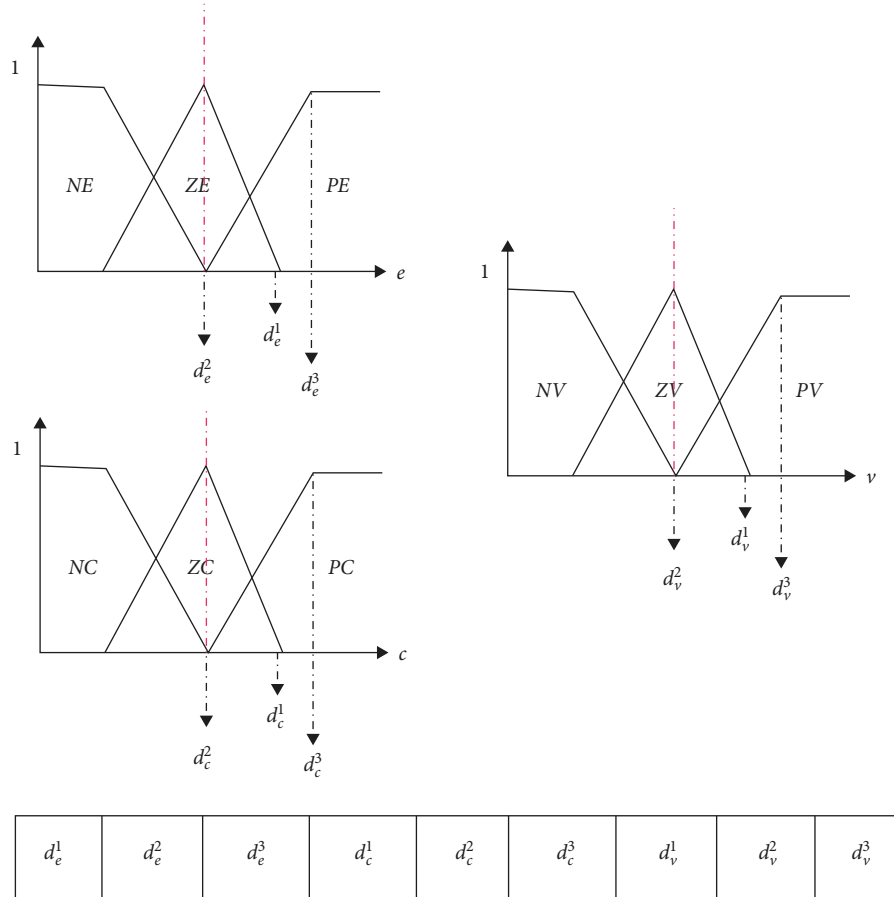


FIGURE 3: Example of a symmetrical variables.

“positive chance”; and NV, ZV, and PV are the linguistic terms for “negative voltage,” “zero voltage,” and “positive voltage.”

The fuzzy function proposed for the control is Gaussian for ZV, ZE, and ZC. Sigmoid functions were used, as were Z shape membership functions for NE, NC, and NV, and for the rest of the variables, the S shape function was implemented. Three parameters are needed in order to define a Gaussian function, while 2 parameters are needed for sigmoid functions. The optimization problem is then defined by 21 parameters. The number of variables requires a considerable amount of computation time and the use of resources for the optimization algorithm. Therefore, the following methodology was implemented in order to reduce the number of variables.

2.3. Methodology. In [37] a method for reducing the number of parameters for a fuzzy set control through the use of

symmetrical discourses was proposed. In basic terms, these variables can distribute several sets to the positive part of the discourse universe, and then reflect them all in the negative part. It is important to consider that not all the applications can be addressed with these variables, as it is preferable that every consequent action of the fuzzy system has the same magnitude in both positive and negative directions. In this case, the symmetrical discourses can be applied because the servomotors have the same range for the output in the positive and negative response.

For example, in Figure 3, different membership functions (MFs) are shown, all of which are symmetrical. The NULL or Zero set corresponding to the triangular function is located exactly in the middle of the discourse universe (red line) while the opening of the triangular function is varied, denoted as d_e^1 . In order to achieve a symmetric function, the provided value is changed to negative and as a result, the complete function is obtained. The parameters of S function are defined by d_e^2 and d_e^3 , and to obtain the Z function, the S

parameter functions are reflected. With this approach, the shape of the error sets can be defined with three parameters. This same approach is also applied for the change and voltage variables. When applying this method to the proposed problem, the number of parameters is reduced from 21 to 9.

In the methodology proposed in [37], GA was used as an optimization method, while in this paper the auto adaptive differential evolution proposed by [40] is used. This is because it tends to converge to the solution in fewer iterations (ten), and does not depend on the number of the population as with GA. A description of the algorithm is presented in the next section.

2.4. Autoadaptive Differential Evolution Algorithm (AADE). The AADE is a type of evolutionary algorithm used for multidimensional real-valued functions. This method does not require gradient information, which means that the optimization problem does not need to be differentiable. In addition, it has an efficient memory utilization as well as being effective and robust [36, 40–42]. The main feature of AADE is that parameters, such as F (factor scale) and Cr (crossover constant), show evidence of self-adaptation during an evolution phase, unlike GA or classical differential evolution (DE) algorithms, increasing its power and execution. Figure 4 summarizes the AADE operation flow chart. More specifically AADE's basic strategy can be described as shown below.

2.4.1. Population. The population is a vector x defined as

$$x = (x_1, x_2, \dots, x_D), \quad (2)$$

where D is the dimensionality of the function f . The variables domains are defined by their lower and upper bounds: $x_{j,\text{low}}$ and $x_{j,\text{upp}}$; $j \in \{1, \dots, D\}$. The initial population is selected randomly between the lower ($x_{j,\text{low}}$) and upper ($x_{j,\text{upp}}$) bounds defined for each variable x_j . The bounds are specified according to the user.

2.4.2. Mutation. In every iteration (generation) G , DE uses the mutation operation for producing the donor vector. For each target vector x_b , G , $i = 1, 2, 3, \dots, NP$, a mutant vector

$$U_{ji,G+1} = \begin{cases} U_{ji,G+1}, & \text{if } (\text{rand } b(j) \leq CR) \text{ or } j = \text{rnbr}(i), \\ x_{ji,G}, & \text{if } (\text{rand } b(j) > CR) \text{ and } j \neq \text{rnbr}(i), \end{cases} \quad j = 1, 2, \dots, D, \quad (5)$$

where $\text{rand } b(j)$ is the j th evaluation of a uniform random number generator within the range $[0, 1]$, which has to be determined by the user. $\text{rnbr}(i)$ is a randomly chosen index $\epsilon 1, 2, \dots, D$, which ensures that $U_{i,G+1}$ receives at least one parameter from $U_{i,G+1}$.

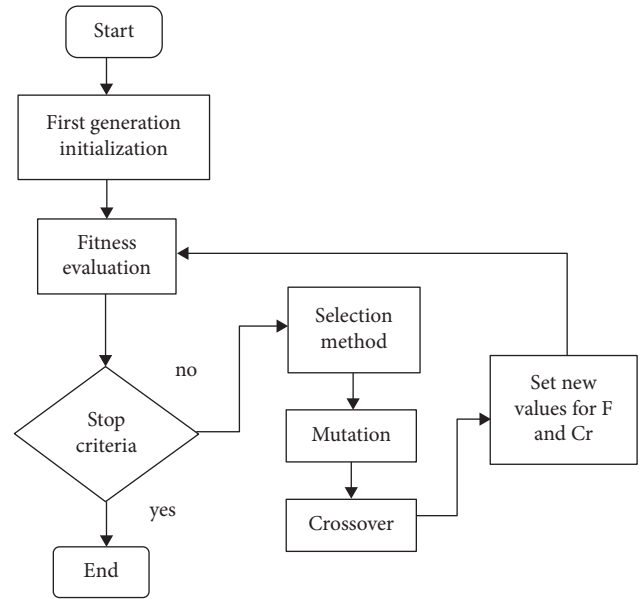


FIGURE 4: DE flow chart.

$v_i = \{v_{i,1}, v_{i,D}\}$ is generated according to a specific mutation scheme. The most widely used in differential evolution are

$$\begin{aligned} \frac{DE}{(\text{rand}/1v_i)} &= x_{r1} + F(x_{r2} + x_{r3}), \\ \frac{DE}{(\text{best}/1v_i)} &= x_{\text{best}} + F(x_{r1} + x_{r2}), \\ \frac{DE}{(\text{rand}/2v_i)} &= x_{r1} + F(x_{r2} + x_{r3}) + F(x_{r4} + x_{r5}), \end{aligned} \quad (3)$$

where r_1, r_2, r_3, r_4 , and r_5 are random integers within the range $[1, NP]$ and are different to index i ($r_1 \neq r_2 \neq r_3 \neq r_4 \neq r_5 \neq i$). F is a real and constant factor, which controls the amplification of the differential variation.

2.4.3. Crossover. The crossover operator is used to increase the perturbed parameter vectors' diversity. The trial vector

$$U_{i,G+1} = (U_{1i,G+1}, U_{1i,G+1}, \dots, U_{Di,G+1}), \quad (4)$$

is formed, where

2.4.4. Selection. The trial vector $U_{i,G+1}$ is compared to the target vector $x_{i,G}$ using the greedy criterion in order to decide whether or not it should become a member of generation $G + 1$. If vector $U_{i,G+1}$ yields a smaller cost function value than $x_{i,G}$, then $x_{i,G+1}$ is set to $U_{i,G+1}$; otherwise, the old value $x_{i,G}$ is retained.

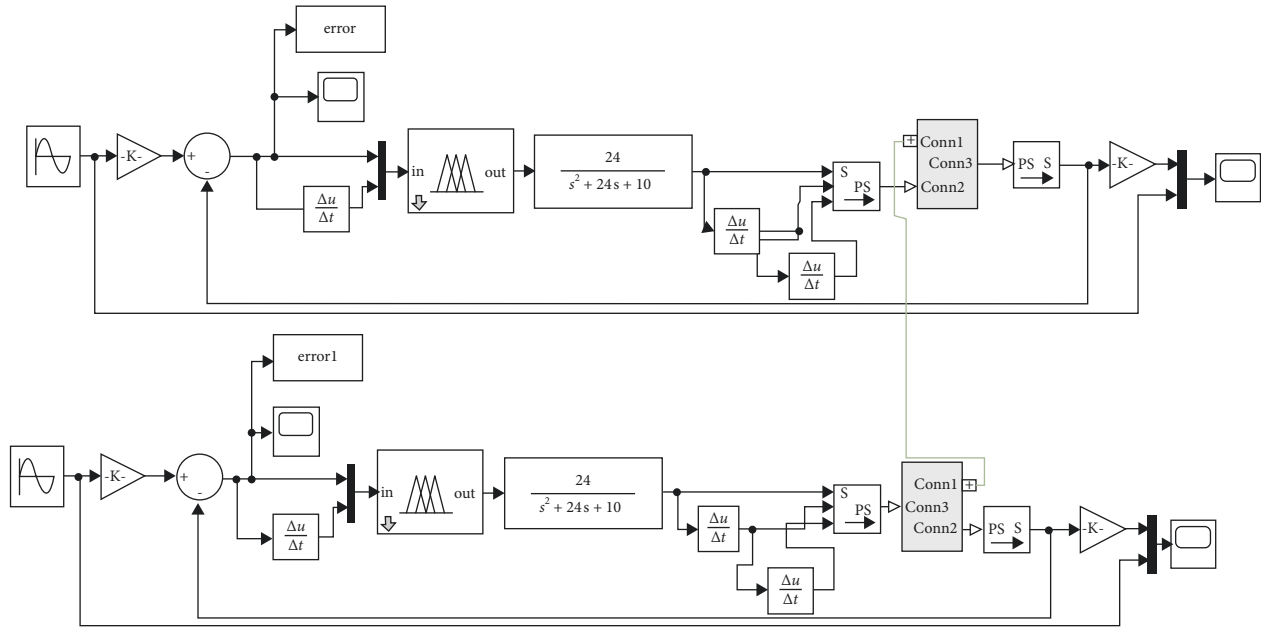


FIGURE 5: Block diagram of the finger control system.

2.4.5. *F and Cr Value Adjust.* The estimation of the F and Cr values depends on the following equations:

$$F_{i+1,G} = F_{i+1,G} - \text{rand}_{i,j}[0, 1] * \left(\frac{f(U_{i,G}) - f(Y_{i,G})}{f(U_{i,G})} \right),$$

$$Cr_{i+1,G} = Cr_{i+1,G} - \text{rand}_{i,j}[0, 1] * \left(\frac{f(U_{i,G}) - f(Y_{i,G})}{f(U_{i,G})} \right),$$

$$F_{G+1} = \text{rand}_{i,j}[0, 1] * \left(\frac{\text{max} - \text{min}}{\text{max}} \right),$$

$$C_{G+1} = \text{rand}_{i,j}[0, 1] * \left(\frac{\text{max} - \text{min}}{\text{max}} \right), \quad (6)$$

where $F_{i+1,G}$ and $Cr_{i+1,G}$ represent the estimation of the F and Cr of each vector. $f(U_{i,G})$ is the new vector and $f(Y_{i,G})$ is the current vector. F_{G+1} and C_{G+1} are the new F and CR values for the next generation. In addition, the max and min are values obtained from an array that contains all $F_{i+1,G}$ and $Cr_{i+1,G}$. The methodology implemented is as follows:

- (1) Start AADE algorithm
 - (a) Set the initial parameters.
 - (b) Initialize all NP individuals with random positions.
 - (c) Generate three and four individuals from the current population randomly based on the mutation used.
 - (d) Apply the mutation operator to form the donor vector using equation (6).
 - (e) Apply the crossover operator in order to increase diversity.
 - (f) Calculate the fitness of each individual.

(g) Calculate the new F and Cr values.

- (2) Once the best individual is found, every parameter must be assigned to its corresponding set.
- (3) Evaluate the fuzzy system.

2.5. Simulations and Results

2.5.1. *Experimental Configuration.* The numerical experiments were carried out on a Legion Y540-15IRH laptop with Core i7 9th gen processor, 16 GB RAM, and a clock speed of 2.6 GHz with turbo boost of up to 4.5 GHz.

Considering the range of flexion/extension movements generated by the human finger, a middle part of a sinusoidal trajectory was proposed as a reference for the position control. Due to the robotic finger design configuration, the amplitude of the function is 1.4835 rad (85°) for the proximal phalanx and 1.3962 rad (80°) for the medial phalanx. The equation of the mean squared error (MSE) is used in order to measure the performance of the fuzzy controller. The goal function is as follows:

$$\min \left\{ \frac{1}{N} \sum_{k=1}^N [x(k) - y(k)]^2 + M_1 h_1 \right\}, \quad (7)$$

where $h_1(x) = 0 \rightarrow$ the values are in the range. $h_1(x) = 1 \rightarrow$ otherwise.

In equation (1), $x(k)$ represents the value at time k , $y(k)$ is the value produced by the system at time k , and N represents the total number of samples. M_1 is a constant of a very high value that penalize the goal function when the constraint fails.

The optimization problem is defined by

- (i) Design variables $X = [d_e^1, d_e^2, d_e^3, d_c^1, d_c^2, d_c^3, d_v^1, d_v^2, d_v^3]$.

TABLE 4: Parameters for set distribution with different mutation strategies.

Mutation strategy	d_c^1	d_c^2	d_c^3	d_v^1	d_v^2	d_v^3	d_v^1	d_v^2	d_v^3
DE/rand/1	0.5677	0.0873	0.0014	0.1883	0.3423	0.1870	0.9259	5.7279	7.6088
DE/best/1	0.7120	0.0957	0.0053	0.2691	0.4952	0.2781	3.6487	4.0871	6.5742
DE/rand/2	0.3860	0.0406	0.0180	0.2568	0.2537	0.3045	0.3248	6.003	6.6644

TABLE 5: Comparison of different mutations strategies in terms of error value.

Mutation strategy	Fitness Pha1	Fitness Pha2
DE/rand/1	$3.1352E-04$	$2.7109E-04$
DE/best/1	$7.2511E-04$	$6.4323E-04$
DE/rand/2	$4.1357E-04$	$4.0554E-04$

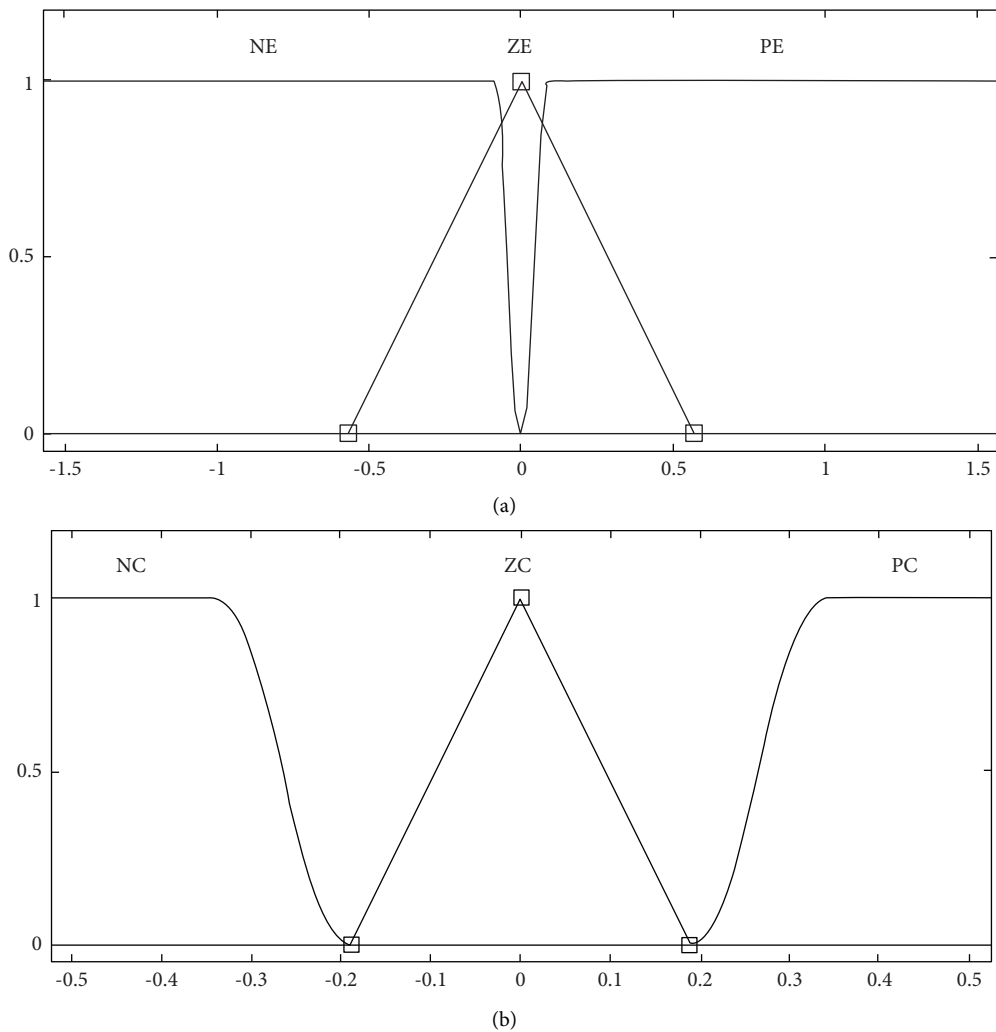


FIGURE 6: Membership function obtained for inputs: (a) error and (b) change.

(ii) Limits of the variables: $d_e^1, d_e^2, d_e^3 \in [0, (\pi/2)]$; $d_c^1, d_c^2, d_c^3 \in [0, (\pi/6)]$; and $d_v^1, d_v^2, d_v^3 \in [-8.16, 8.16]$.

(iii) Parameters of the algorithm:

Population size = 50.

Generation limit = 150.

$F = 0.5$.

Crossover rate = 0.2.

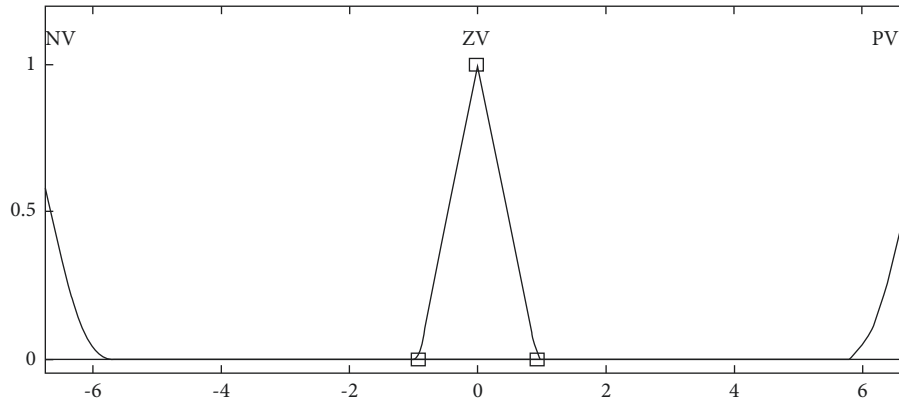


FIGURE 7: Membership function obtained for the output.

The proposed optimization algorithm was implemented using Matlab software, while the parallel mode was used because it increases the convergence speed, thereby demonstrating another advantage of using this approach. The algorithm was iterated using the mutation strategies from equations (5)–(7), with 30 total iterations, and 10 per each mutation strategy. In order to evaluate the proposed fuzzy control, some simulations were carried out using the Simulink environment. For simulation purposes, a finger from the hand model presented in Figure 1 was exported to Simmechanics, and the control was implemented in two parts: one for the proximal phalanx and another for the middle phalanx. This is because the distal and middle phalanxes are connected through a link resulting in a subactuated mechanism. Only one finger is simulated because it is the same movement for the other fingers. The block diagram is shown in Figure 5.

3. Results and Discussion

Table 4 shows the best performance solutions for the finger control with the three used mutation strategies.

The fitness of each solution is shown in Table 5. Pha1 and Pha2 represent the proximal and middle phalanges, respectively. All solutions are acceptable because the error is very close to zero, although the best solution is presented by DE/rand/1, followed by DE/rand/2 and DE/best/1.

Using DE/rand/1 solution, the input and output values of the fuzzy system are defined. Figures 6 and 7 show the membership functions and Figure 8 shows the 3D surface viewer of the fuzzy logic controller to get a perspective of rules design.

The results of the virtual prototype and comparison between the desired trajectory and the trajectory by the control of each phalanx are shown in Figures 9 to 11. Figure 9 shows the virtual configuration of the robotic underactuated finger, while the position of the distal phalanx depends on the movement of the middle phalanx, which is transmitted by the P bar.

Based on Figure 10, DTPP represents the desired trajectory of the proximal phalanx and OTTP is the obtained trajectory. The maximum rotation value of the proximal phalanx is 1.4835 rad due to the configuration of the

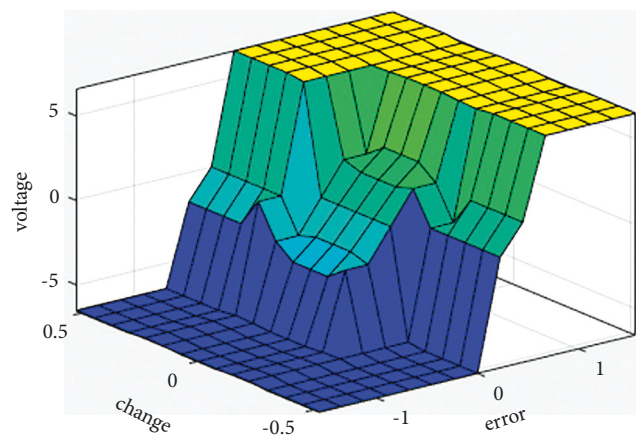


FIGURE 8: Rule surface.

mechanism. As can be seen in the finger's final position, the base is represented by the B block and the movement by the A block. The time simulation is 3.2 s, and the OTTP converges to DTPP with an error of $3.1352E - 04$ rad. This error is more visible in two intervals, from 1.3 to 2 and from 2.5 to 3.2. Between the trajectories, there are oscillations that cannot be appreciated because they are very small ($1E - 03$ rad) and appear in the interval from 0 to 1.4 s.

Referring to the results of Figure 11, DTMP and OTMP are the desired and obtained trajectories of the medial phalanx. The maximum rotation value is 1.3089 rad due to the finger structure. Compared to the human finger range there is a difference of 16.66%, meaning that the finger is not able to grasp small cylindrical objects (diameter of less than 60 mm). The error between trajectories is $2.7109E - 04$ rad.

According to analysis of its behavior, the controller presents a fast response due to the extremely small error tolerance (0.1 approx.), based on the membership function intersection (Figure 6(a)). Under the same conditions and modifying only the d_e^3 values, the system response speed decreases. On the other hand, after only modifying the parameter d_c^3 to values less than 0.2, the system does not present changes. It means that the motor does not change the direction of rotation and its velocity is the same under any condition. In this way, the values for d_e^1 , d_e^2 , and d_e^3 affect the response speed of the controller, the signal to change

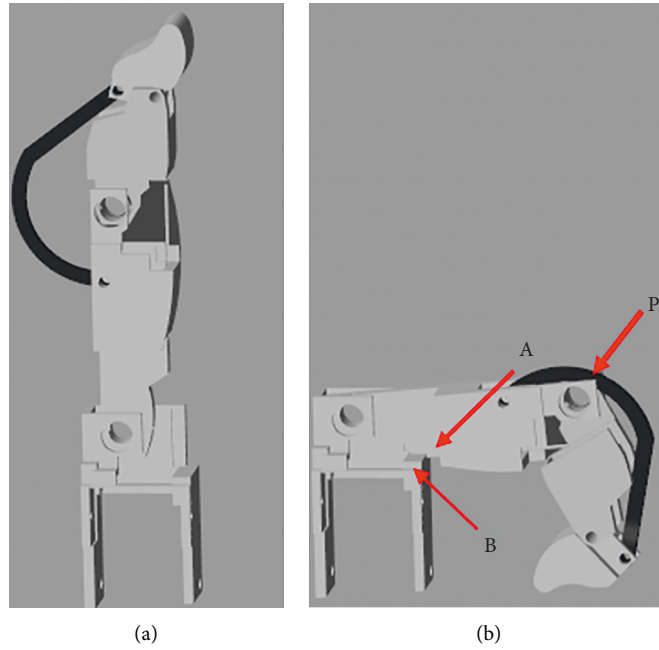


FIGURE 9: Finger position: (a) initial and (b) final.

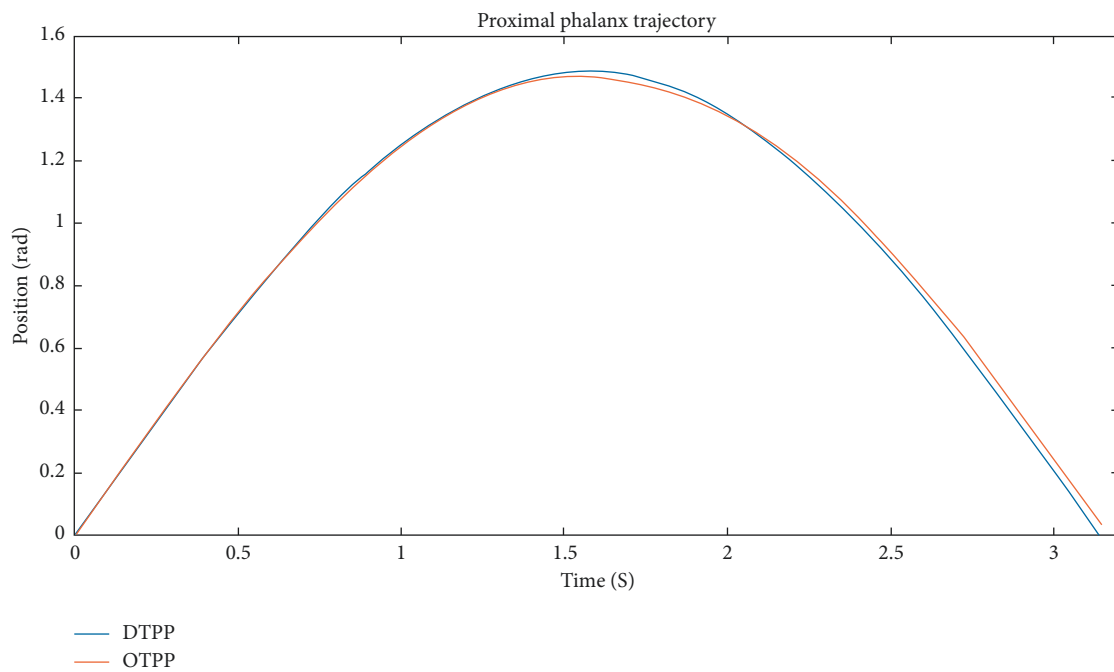


FIGURE 10: Comparison of desired and obtained trajectory for proximal phalanx.

rotation of the motor is defined by the parameters d_c^1 , d_c^2 , and d_c^3 . The rest of the parameters define the motor rotation speed.

Table 6 shows a comparison between the present work and some results previously reported in the literature, and it can be observed that almost all of the finger models are underactuated. The most common technique for controlling the position of the robotic finger is the PID controller with some variants. A fuzzy controller is also used but the

parameters are manually selected. Based on information in the table, in some cases, the finger dynamic model is presented in order to control the three joints. In [10, 12, 14], the authors report a step response with a steady-state error (SSE) of 0, although in [10] the time response is more than 10 sec. On the other hand, the numerical results presented in [12, 14] show settling times of less than 5 sec, but the control parameters are manually obtained. Tasar et al. [11] used a PID controller for a regulation problem of a full-actuated

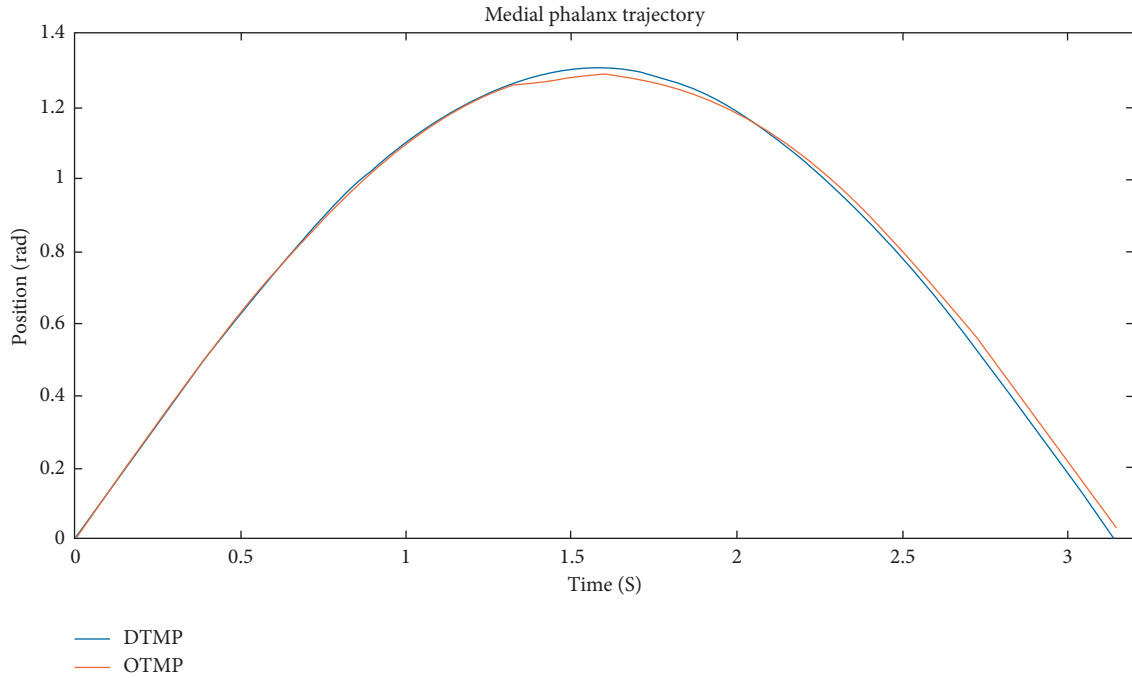


FIGURE 11: Comparison of desired and obtained trajectory for medial phalanx.

TABLE 6: Comparison between different control strategies.

Author	Control	Finger dynamic model	Trajectories	Error
Calderon et al. [10]	PI	No	Step 17 mm	SSE 0
Tasar et al. [11]	PID	Yes	Step (for three phalanxes)	SSE 0.255 deg (max)
Ghazali et al. [14]	Fuzzy-PID	No	Step 90 deg	SSE 0 deg
Ghazali et al. [14]	Fuzzy	No	Step 90 deg	SSE 0.12 deg
Raković et al. [12]	Fuzzy	No	Step 100 rad	SSE 0 rad
Jalani et al. [43]	PID	Yes	Sinusoidal [0–(–1)] rad	0.0159 rad
Jalani et al. [43]	Adaptive	Yes	Sinusoidal [0–4] rad	0.0791 rad
Jalani et al. [43]	SMC	Yes	Sinusoidal [0–(–1)] rad	0.0167 rad
Our proposal	Optimized fuzzy	No	Sinusoidal [0–1.483] rad	3.1352E–04 rad

robotic finger. A maximum overshoot of 14.902° was achieved for a reference of 90° for each actuated phalanx. Sinusoidal trajectories are proposed in [43] and different control techniques are presented. As in previous cases, the control parameters are tuned manually. The considered trajectory is a sinusoidal function with an amplitude range [0–(–1)] rad in PID and SMC (sliding model control) cases, which is very similar to what is reported in this work but with a larger error. The main difference with our work is that the controller parameters are automatically adjusted, and the obtained error is the smallest in all the presented trajectories.

Regarding the optimization of the fuzzy control, other works have presented methods that, in some cases, optimize more than 10 variables [29]. Moreover, the most common algorithm is GA, although one of the main problems with this type of algorithm is that it is largely dependent on the population size. Moreover, the selection of the initial parameters represents a challenge because selecting the wrong values can lead to the algorithm not converging. In order to avoid this problem, the methods applied in this paper show

that it is possible to reduce the number of parameters, considering that the fuzzy set is symmetrical. Instead of using a GA algorithm, it was decided to implement an AADE algorithm because the control parameters F and CR are automatic and the time convergence is smaller compared to GA. Another advantage is that the AADE has the potential to generate a fuzzy control with no previous knowledge of the system.

4. Conclusion

When removing the empiricism of a fuzzy controller, a nonlinear problem with several dimensions appears, which can be solved by focusing on the membership function to generate a desired control. In this paper, the auto adaptive differential evolution algorithm was implemented because of the limitations of other methods such as genetic algorithms, artificial bee colonies, or ant colonies. The chosen method performs a sophisticated local search through the recombination method, and the way in which the mutated method

vector is calculated means that the algorithm depends less on an initial position. Furthermore, another advantage is that F and Cr values are calculated automatically. Additionally, the use of the symmetrical discourses is different to other methods for finding the membership function mentioned in the introduction. Specific information about the system is neither not needed nor necessary to work with all the variables shown in the proposed problem. At the start of the process, it was composed of 21 variables, and before applying the method, the variables were reduced to 9. With the obtained vector, the MFs were generated to the fuzzy control. From the simulation, the obtained results proved that the control is able to perform flexion-extension movements following the proposed trajectory with an error of almost zero, despite not having a mathematical model of the robotic hand. It would be very difficult to achieve these results by selecting the controller parameters empirically.

The following step in this research is to prove experimentally the effectiveness of the proposed controller by carrying out tests on the physical prototype reported in [38]. In addition, future studies will focus on the optimization of membership functions to generate movement in the palm and doing fingers able to perform different kinds of grasps to evaluate the efficiency of this type of control scheme. Another interesting topic to be addressed in future works is the consideration of type-3 fuzzy logic systems (T3FLS) to improve the control system performance. T3FLS have been proposed to handle an increased number of uncertainties [44]. However, their main disadvantages are that the structure of the fuzzy sets has been assumed to be constant and the membership computation is complicated. Moreover, studies on the parameter optimization of T3FLS have been scarcely reported in literature [45]. Therefore, combining AADE algorithms with T3FLS could be a promising alternative to provide robustness and improve the fuzzy logic controller performance.

Data Availability

The data that support the findings of this study are available upon request to the corresponding author.

Conflicts of Interest

The authors declare that they have no conflicts of interest.

Acknowledgments

The authors are grateful to the National Council of Science and Technology (CONACYT) and to the Project 621 from the Cathedra's Program for supporting the research presented in this paper.

References

- [1] Y. Wang, X. Wu, D. Mei, L. Zhu, and J. Chen, "Flexible tactile sensor array for distributed tactile sensing and slip detection in robotic hand grasping," *Sensors and Actuators A: Physical*, vol. 297, p. 111512, 2019.
- [2] S. Bilgin, Y. Üser, and M. Mercan, "Robotic hand controlling based on flexible sensor," *International Journal of Engineering and Applied Sciences*, vol. 8, no. 4, p. 49, 2016.
- [3] H. Liu and D. Geng, "Kinematics modeling and grasping experiment of pneumatic four-finger flexible robotic hand," *Proceedings of the Institution of Mechanical Engineers - Part C: Journal of Mechanical Engineering Science*, vol. 235, no. 24, pp. 7894–7906, 2021.
- [4] P. M. Khin, J. H. Low, M. H. Ang, and C. H. Yeow, "Development and grasp stability estimation of sensorized soft robotic hand," *Frontiers in Robotics and AI*, vol. 8, p. 619390, 2021.
- [5] P. Svensson, C. Antfolk, N. Malesevic, and F. Sebelius, "Characterization of pneumatic touch sensors for a prosthetic hand," *IEEE Sensors Journal*, vol. 20, no. 16, pp. 9518–9527, 2020.
- [6] Z. Deng, Y. Jonetzko, L. Zhang, and J. Zhang, "Grasping force control of multi-fingered robotic hands through tactile sensing for object stabilization," *Sensors*, vol. 20, no. 4, p. 1050, 2020.
- [7] A. M. Almassri, W. Z. Wan Hasan, S. A. Ahmad et al., "Pressure sensor: state of the art, design, and application for robotic hand," *Journal of Sensors*, vol. 2015, pp. 1–12, 2015.
- [8] A. Saudabayed and H. A. Varol, "Sensors for robotic hands: a survey of the state of the art," *IEEE Access*, vol. 3, pp. 1765–1782, 2015.
- [9] M. K. Kasim, R. L. Shauri, and K. Nasir, "PID position control of three-fingered hand for different grasping styles," in *Proceedings of the 6th Control and System Graduate Research Colloquium (ICSGRC)*, pp. 7–10, Shah Alam, Malaysia, August 2015.
- [10] C. A. Calderon, C. Ramirez, V. Barros, and G. Punin, "Design and deployment of grasp control system applied to robotic hand prosthesis," *IEEE Latin America Transactions*, vol. 15, no. 2, pp. 181–188, 2017.
- [11] B. Tasar, A. B. Tatar, A. K. Tanyildizi, and O. Yakut, "Design, dynamic modelling and control of wearable finger orthosis," *Journal of Mechanics in Medicine and Biology*, vol. 21, no. 1, 2021.
- [12] M. Raković, G. Anil, Z. Mihajlović et al., "Fuzzy position-velocity control of underactuated finger of FTN robot hand," *Journal of Intelligent and Fuzzy Systems*, vol. 34, no. 4, pp. 2723–2736, 2018.
- [13] X. h. Liu, X. h. Chen, X. h. Zheng, S. p. Li, and Z. b. Wang, "Development of a GA-fuzzy-immune PID controller with incomplete derivation for robot dexterous hand," *The Scientific World Journal*, vol. 2014, pp. 1–10, 2014.
- [14] R. Ghazali, M. Z. Saad, S. Y. S. Hussien, M. H. Jali, F. N. Zohedi, and T. A. Izzuddin, "Intelligent controller design for multifunctional prosthetics hand," *International Journal of Mechanical Engineering and Robotics Research*, vol. 6, no. 6, pp. 495–501, 2017.
- [15] K. Sato and G. J. Maeda, "A practical control method for precision motion-Improvement of NCTF control method for continuous motion control," *Precision Engineering*, vol. 33, no. 2, pp. 175–186, 2009.
- [16] I. Yusuf, Y. Yusuf, and N. Iksan, "FGA temperature control for incubating egg," *Advances in Fuzzy Systems*, vol. 2012, no. 1, pp. 1–8, 2012.
- [17] W. S. Chan, C. Y. Lee, C. W. Chang, and Y. H. Chang, "Interval type-2 fuzzy neural network for ball and beam systems," in *Proceedings of the International Conference on Systems Science and Engineering*, pp. 315–320, Taipei, Taiwan, July 2010.

- [18] Q. Zhu, Y. Han, C. Cai, and Y. Xiao, "Robust optimal navigation using nonlinear model predictive control method combined with recurrent fuzzy neural network," *Mathematical Problems in Engineering*, vol. 2018, pp. 1–19, 2018.
- [19] L. Amador-Angulo and O. Castillo, "Optimization of the type-1 and type-2 fuzzy controller design for the water tank using the bee colony optimization," in *Proceedings of the Conference on Norbert Wiener in the 21st Century*, pp. 1–8, Boston, USA, June 2014.
- [20] M. Nikolić, M. Šelmić, D. Macura, and J. Čalić, "Bee colony optimization metaheuristic for fuzzy membership functions tuning," *Expert Systems with Applications*, vol. 158, p. 113601, 2020.
- [21] M. S. Jacob and P. Selvi Rajendran, "Fuzzy artificial bee colony-based CNN-LSTM and semantic feature for fake product review classification," *Concurrency and Computation: Practice and Experience*, vol. 34, no. 1, 2022.
- [22] A. Rezoug, Z. Achour, and M. Hamerlain, "Ant colony optimization of type-2 fuzzy helicopter controller," in *Proceedings of the International Conference on Robotics and Biomimetics (ROBIO)*, pp. 1548–1553, Bali, Indonesia, December 2014.
- [23] A. Ragmani, A. Elomri, N. Abghour, K. Moussaid, and M. Rida, "An improved hybrid fuzzy-ant colony algorithm applied to load balancing in cloud computing environment," *Procedia Computer Science*, vol. 151, pp. 519–526, 2019.
- [24] V. Sangeetha, R. Krishankumar, K. S. Ravichandran et al., "A fuzzy gain-based dynamic ant colony optimization for path planning in dynamic environments," *Symmetry*, vol. 13, no. 2, p. 280, 2021.
- [25] L. D. Seixas and F. C. Correa, "Comparison between genetic algorithm and differential evolution tuning a fuzzy controller," *Mathematics in Engineering Science and Aerospace (MESA)*, vol. 11, no. 3, pp. 1–11, 2020.
- [26] S. Tsafarakis, K. Zervoudakis, A. Andronikidis, and E. Altsitsiadis, "Fuzzy self-tuning differential evolution for optimal product line design," *European Journal of Operational Research*, vol. 287, no. 3, pp. 1161–1169, 2020.
- [27] O. Castillo, F. Valdez, J. Soria et al., "Optimal design of fuzzy systems using differential evolution and harmony search algorithms with dynamic parameter adaptation," *Applied Sciences*, vol. 10, no. 18, p. 6146, 2020.
- [28] H. Zhang, N. Xu, G. Zong, and A. F. Alkhateeb, "Adaptive fuzzy hierarchical sliding mode control of uncertain underactuated switched nonlinear systems with actuator faults," *International Journal of Systems Science*, vol. 52, no. 8, pp. 1499–1514, 2021.
- [29] Y. Li, N. Xu, B. Niu, Y. Chang, J. Zhao, and X. Zhao, "Small-gain technique-based adaptive fuzzy command filtered control for uncertain nonlinear systems with unmodeled dynamics and disturbances," *International Journal of Adaptive Control and Signal Processing*, vol. 35, no. 9, pp. 1664–1684, 2021.
- [30] Y. Chang, P. Zhou, B. Niu et al., "Switched-observer-based adaptive output-feedback control design with unknown gain for pure-feedback switched nonlinear systems via average dwell time," *International Journal of Systems Science*, vol. 52, no. 9, pp. 1–15, 2021.
- [31] O. Castillo and P. Melin, "A review on the design and optimization of interval type-2 fuzzy controllers," *Applied Soft Computing*, vol. 12, no. 4, pp. 1267–1278, 2012.
- [32] N. Öztürk and E. Çelik, "Speed control of permanent magnet synchronous motors using fuzzy controller based on genetic algorithms," *International Journal of Electrical Power & Energy Systems*, vol. 43, no. 1, pp. 889–898, 2012.
- [33] H. Zhang, B. Zhang, and F. Wang, "Automatic fuzzy rules generation using fuzzy genetic algorithm," in *Proceedings of the Sixth International Conference on Fuzzy Systems and Knowledge Discovery*, pp. 107–112, Tianjin, China, August 2009.
- [34] H. Liang, J. Zou, K. Zuo, and M. J. Khan, "An improved genetic algorithm optimization fuzzy controller applied to the wellhead back pressure control system," *Mechanical Systems and Signal Processing*, vol. 142, p. 106708, 2020.
- [35] N. Lukman, M. Irfan, A. Nugraha, and J. Jumadi, "Comparison between genetic algorithm with differential evolution in study scheduling," in *Proceedings of the 5th Annual Applied Science and Engineering Conference (AASEC 2020)*, Bandung, Indonesia, April 2020.
- [36] M. Georgioudakis and V. Plevris, "A comparative study of differential evolution variants in constrained structural optimization," *Frontiers in Built Environment*, vol. 6, 2020.
- [37] A. Téllez-Velázquez, H. Molina-Lozano, L. A. Villa-Vargas et al., "A feasible genetic optimization strategy for parametric interval type-2 fuzzy logic systems," *International Journal of Fuzzy Systems*, vol. 20, no. 1, pp. 318–338, 2018.
- [38] F. J. Espinosa-Garcia, R. Tapia-Herrera, E. Lugo-Gonzalez, and M. Arias-Montiel, "Development of a robotic hand based on a metamorphic mechanism for extending the thumb's functionality," *Journal of the Brazilian Society of Mechanical Sciences and Engineering*, vol. 43, pp. 1–16, 2021.
- [39] B. Pillai and K. T. Nair, "Intelligent adaptive control for DC servo motor position control in LabVIEW," in *Proceedings of the International Conference on Intelligent Computing, Instrumentation and Control Technologies (ICICCT)*, pp. 981–985, Kerala, India, July 2017.
- [40] V. Sharma, S. Agarwal, and P. K. Verma, "Auto adaptive differential evolution algorithm," in *Proceedings of the Third International Conference on Computing Methodologies and Communications (ICCMC)*, pp. 958–962, Erode, India, March 2019.
- [41] D. Zaharie, "A comparative analysis of crossover variants in differential evolution," in *Proceedings of the International Multiconference on Computer Science and Information Technology (IMCSIT)*, pp. 171–181, Wisla, Poland, October 2007.
- [42] A. Slowik and H. Kwasnicka, "Evolutionary algorithms and their applications to engineering problems," *Neural Computing & Applications*, vol. 32, no. 16, pp. 12363–12379, 2020.
- [43] J. Jalani, G. Herrmann, and C. Melhuish, "Robust trajectory following for underactuated robot fingers," in *Proceedings of the UKACC International Conference on Control*, pp. 1–6, Coventry, UK, September 2010.
- [44] A. Mohammadzadeh, M. H. Sabzalian, and W. Zhang, "An interval type-3 fuzzy system and a new online fractional-order learning algorithm: theory and practice," *IEEE Transactions on Fuzzy Systems*, vol. 28, no. 9, pp. 1940–1950, 2020.
- [45] S. N. Qasem, A. Ahmadian, A. Mohammadzadeh, S. Rathinasamy, and B. Pahlevanzadeh, "A type-3 logic fuzzy system: optimized by a correntropy based Kalman filter with adaptive fuzzy kernel size," *Information Sciences*, vol. 572, pp. 424–443, 2021.

Research Article

SPMSM Sensorless Control System Based on ASMO

Yu Cao  and Chuang Liu

College of Automation Engineering, Nanjing University of Aeronautics and Astronautics, Nanjing 211106, China

Correspondence should be addressed to Yu Cao; yu_cao_bx1403516@126.com

Received 6 December 2021; Revised 25 January 2022; Accepted 21 February 2022; Published 30 March 2022

Academic Editor: Rosalba Galván-Guerra

Copyright © 2022 Yu Cao and Chuang Liu. This is an open access article distributed under the Creative Commons Attribution License, which permits unrestricted use, distribution, and reproduction in any medium, provided the original work is properly cited.

Aiming at the chattering problem of traditional sliding mode observer (SMO) in surface-mounted permanent magnet synchronous motor (SPMSM) control system when estimating rotor position and speed and adaptive sliding mode observer (ASMO) is designed in this paper. The observer can reduce chattering and avoid the introduction of the low-pass filter, which simplifies the system structure, considering the difficulty in determining the sliding mode gain of the existing sliding mode observer, and an adaptive law is designed to adjust the sliding mode gain with the change of the back electromotive force, to meet the operation requirements of the system and improve the control accuracy of the sensorless control system. Finally, the simulation is built through Matlab/Simulink platform. It is proved that the proposed control strategy can satisfy the system's accuracy and simultaneously reduce the chattering and solve the problem that the gain is difficult to determine.

1. Introduction

Surface-mounted permanent magnet synchronous motor has obvious advantages of high mechanical efficiency and high power factor [1], so it is widely used in wind power generation systems. Because wind turbines often operate in harsh environments, mechanical sensors' installation and use will increase the system's cost and reduce its reliability [2]. Therefore, speed sensorless control has become a research hotspot. At present, the commonly used algorithms include sliding mode observer, model reference adaptive control [3–7], extended Kalman filter [8–11], and artificial intelligence method [12–14]. The sliding mode observer has been widely used in speed sensorless SPMSM rotor position and speed estimation due to its insensitivity to disturbance and parameters, fast response, and other advantages [15]. However, the sliding mode control structure's characteristics bring strong robustness and cause system chattering, which hinders its application in practical engineering. Therefore, the low-pass filter introduced in the traditional SMO algorithm filters the back EMF. Because the cutoff frequency of the traditional low-pass filter is fixed, the ripple component in the back EMF cannot be eliminated, which seriously affects the estimation accuracy of rotor position [16].

To obtain a smooth estimation of the back EMF and SMO based on a variable cutoff frequency low-pass filter and a modified back EMF, the observer is proposed in the literature [17]. The SMO can effectively suppress the high frequency and ripple components of the back EMF. However, the filter's introduction causes the system's phase delay to a certain extent, and the two-stage filtering structure also causes the system's design complexity. It is not easy to implement. In literature [18], a sliding mode observer with a sinusoidal saturation function is designed to reduce chattering. However, because the saturated boundary layer is closely related to the approaching velocity and buffeting, how to choose a reasonable boundary layer is a big problem. In literature [19, 20], a sliding mode observer with improved reaching law is proposed to reduce the chattering caused by sliding mode control. Although the purpose is achieved in some cases, the method will be invalid when the control deviation changes to zero, and the sliding mode gain is also zero.

To avoid introducing a low-pass filter, a new type of sliding mode observer was designed in the literature [21]. The hybrid nonsingular sliding mode terminal sliding surface was applied to the traditional linear sliding mode surface, which reduced the phase lag and chattering

problems. However, the optimization of hybrid non-singular sliding mode design is complicated, and the hardware requirements are relatively high, so it is not easy to realize. Literature [22–25] proposed a sliding mode observer based on the super-twisting algorithm. Although the scheme can effectively suppress sliding mode chattering, it is not easy to choose a good sliding mode gain. The sliding mode gain's stability condition is related to the control function error. Literature [26] proposed a neural network estimation strategy that is used to obtain sliding mode gain. Although this scheme can weaken chattering, the designed variable parameters make the system more complex. Literature [27] proposed a sliding mode observer based on fuzzy radial basis function (RBF) neural network to adjust sliding mode gain to better adapt to external disturbances parameter changes. It needs experience in practice and is difficult to master. The super twisting sliding mode observer based on the adaptive algorithm avoids the introduction of complex neural network on the basis of solving the difficulty in determining the sliding mode gain, but only limited time to enter the sliding mode variable contains households within the neighborhood of plastering, damaging the convergence precision of the algorithm [28].

To avoid the above problems, a sliding mode observer based on the adaptive algorithm is proposed in this paper. The observer has the characteristics of a first-order low-pass filter, which can effectively filter the high-frequency sliding mode noise contained in the estimated back EMF without adding a low-pass filter. Simultaneously, an adaptive gain law varying with the back EMF is designed to adjust the observer's parameters online, which solves excessive gain and effectively suppresses the system's chattering. Finally, the information on rotor position and speed is estimated by using the arctangent function.

2. Traditional SMO

In the $\alpha\beta$ two-phase stationary coordinate system, the mathematical model of SPMSM can be expressed as [17]

$$\left. \begin{aligned} \dot{i}_\alpha &= -\frac{R_s}{L}i_\alpha + \frac{u_\alpha}{L} - \frac{z_\alpha}{L} \\ \dot{i}_\beta &= -\frac{R_s}{L}i_\beta + \frac{u_\beta}{L} - \frac{z_\beta}{L} \end{aligned} \right\}, \quad (1)$$

where u_α, u_β are the stator currents and voltages of α - β axis, respectively; R_s is the stator resistance; L is the stator inductance; z_α, z_β are the back EMFs of the α - β axis; and the expression is

$$\left. \begin{aligned} z_\alpha &= -\psi f \omega e \sin \theta e \\ z_\beta &= \omega e \psi f \cos \theta e \end{aligned} \right\}, \quad (2)$$

where ψf is the rotor flux linkage, θe is the rotor position angle, and ωe is the electric angular velocity of the rotor.

According to (1), the SPMSM sliding mode observer can be constructed.

$$\left. \begin{aligned} \dot{\hat{i}}_\alpha &= -\frac{R_s}{L}\hat{i}_\alpha + \frac{u_\alpha}{L} - \frac{h_\alpha}{L} \\ \dot{\hat{i}}_\beta &= -\frac{R_s}{L}\hat{i}_\beta + \frac{u_\beta}{L} - \frac{h_\beta}{L} \end{aligned} \right\}, \quad (3)$$

where $\hat{i}_\alpha, \hat{i}_\beta$ are the α - β axis estimation values of the stator current.

The stator current error system can be obtained by subtracting (1) from (3).

$$\left. \begin{aligned} \dot{\bar{i}}_\alpha &= -\frac{R_s}{L}\bar{i}_\alpha - \frac{z_\alpha - h_\alpha}{L} \\ \dot{\bar{i}}_\beta &= -\frac{R_s}{L}\bar{i}_\beta - \frac{z_\beta - h_\beta}{L} \end{aligned} \right\}, \quad (4)$$

where $\bar{i}_\alpha = \hat{i}_\alpha - i_\alpha$ and $\bar{i}_\beta = \hat{i}_\beta - i_\beta$ are the errors between the observed current value and the actual current value. h_α, h_β are the SMO control laws, and the expression is

$$\left. \begin{aligned} h_\alpha &= k \text{sign}(\bar{i}_\alpha) \\ h_\beta &= k \text{sign}(\bar{i}_\beta) \end{aligned} \right\}, \quad (5)$$

where k is the sliding mode gain, and $k > \max(|z_\alpha|, |z_\beta|)$.

When the system state reaches the sliding mode surface and enters the sliding mode, the system state remains on the sliding mode surface and satisfies $\bar{i}_\alpha = 0, \bar{i}_\beta = 0$, and according to (5), it can be obtained.

$$\left. \begin{aligned} z_\alpha &= h_\alpha = k \text{sign}(\bar{i}_\alpha) \\ z_\beta &= h_\beta = k \text{sign}(\bar{i}_\beta) \end{aligned} \right\}. \quad (6)$$

Equation (6) contains a nonlinear switching function, which will cause high-frequency chattering of the system, and is not conducive to extracting continuous estimation of the back EMFs. Therefore, the first-order LPFs should be introduced for filtering processing, namely:

$$\left. \begin{aligned} \hat{z}_\alpha &= \frac{wc}{S + wc} z_\alpha \\ \hat{z}_\beta &= \frac{wc}{S + wc} z_\beta \end{aligned} \right\}, \quad (7)$$

where $\hat{z}_\alpha, \hat{z}_\beta$ is the estimated value of the back EMFs; S is a complex frequency; wc is the cutoff frequency of LPFs. Due to the introduction of a first-order low-pass filter, and to obtain a better filtering effect, a lower cutoff frequency should be selected, but this will lead to a large phase lag in the estimation of the back electromotive force, which requires phase compensation for the rotor position. The estimated value of rotor position and speed after compensation is

$$\left. \begin{aligned} \hat{\theta} e &= -\arctan\left(\frac{\hat{z}_\alpha}{\hat{z}_\beta}\right) + \arctan\left(\frac{\hat{\omega} e}{wc}\right) \\ \hat{\omega} e &= \frac{(\hat{z}_\alpha^2 + \hat{z}_\beta^2)^{1/2}}{\psi f} \end{aligned} \right\}. \quad (8)$$

3. Design of the ASMO

To accurately estimate the SPMSM sensorless control system of the rotor position and speed, and to avoid the introduction of the first-order low-pass filter, this paper proposes a sliding mode observer based on the adaptive algorithm, which weakens the chattering phenomenon of the system and reduces LPFs estimation error.

3.1. ASMO. For the SPMSM model (1) and (2), the SMO is constructed [29, 30].

$$\left. \begin{aligned} \dot{\hat{i}}\alpha &= -\frac{R_s}{L}i\alpha + \frac{u\alpha}{L} - \frac{\hat{z}\alpha}{L} - M|\bar{i}\alpha|^{1/2}\text{sign}(\bar{i}\alpha) \\ \dot{\hat{i}}\beta &= -\frac{R_s}{L}i\beta + \frac{u\beta}{L} - \frac{\hat{z}\beta}{L} - M|\bar{i}\beta|^{1/2}\text{sign}(\bar{i}\beta) \\ \hat{z}\alpha &= \int N\text{sign}(\bar{i}\alpha)dt \\ \hat{z}\beta &= \int N\text{sign}(\bar{i}\beta)dt \end{aligned} \right\}, \quad (9)$$

where $\hat{i}\alpha, \hat{i}\beta$ are the α - β axis estimated currents; $\hat{z}\alpha, \hat{z}\beta$ are the α - β axis estimated back EMFs; M, N are the sliding mode gains.

The stator current error system can be obtained by subtracting (1) from (9).

$$\left. \begin{aligned} \dot{\bar{i}}\alpha &= \frac{R_s}{L}\bar{i}\alpha - \frac{z\alpha - \hat{z}\alpha}{L} - M \cdot |\bar{i}\alpha|^{1/2} \cdot \text{sign}(\bar{i}\alpha) \\ \dot{\bar{i}}\beta &= \frac{R_s}{L}\bar{i}\beta - \frac{z\beta - \hat{z}\beta}{L} - M \cdot |\bar{i}\alpha|^{1/2} \cdot \text{sign}(\bar{i}\alpha) \end{aligned} \right\}, \quad (10)$$

where $\bar{z}\alpha = \hat{z}\alpha - z\alpha$ and $z\beta = \hat{z}\beta - z\beta$ are the errors between the observed voltage value and the actual voltage value.

When the system state reaches the sliding mode surface and enters the sliding mode, the system state remains on the sliding mode surface and satisfies $\bar{i}\alpha = 0, \bar{i}\beta = 0$, and according to (9), it can be obtained.

$$\begin{bmatrix} \hat{z}\alpha \\ \hat{z}\beta \end{bmatrix} = \begin{bmatrix} z\alpha \\ z\beta \end{bmatrix} = \begin{bmatrix} \int N\text{sign}(\bar{i}\alpha)dt \\ \int N\text{sign}(\bar{i}\beta)dt \end{bmatrix}. \quad (11)$$

From (11), it can be seen that the estimated back EMFs is a continuous function for the partial derivative of time because of the integral term. Therefore, it is unnecessary to introduce first-order LPF for filtering, and the phase delay of the estimated value of the back EMFs is not caused, which further simplifies the system structure.

To prove the stability of STA-SMO, the Lyapunov function is

$$G1 = \frac{1}{2}(\bar{i}\alpha^2 + \bar{i}\beta^2). \quad (12)$$

The derivative of (12) can be obtained.

$$\dot{G}1 = -\frac{R_s}{L}(\bar{i}^2\alpha + \bar{i}^2\beta) - \frac{1}{L}(\bar{z}\alpha\bar{i}\alpha + \bar{z}\beta\bar{i}\beta) - M(|\bar{i}\alpha|^{3/2} + |\bar{i}\beta|^{3/2}). \quad (13)$$

When $\dot{G}1 < 0$, the observed current of SMO converges in finite time. So M should be designed to be [30].

$$M > \sup \left\{ -\frac{R_s}{L} \cdot \frac{(\bar{i}^2\alpha + \bar{i}^2\beta)}{|\bar{i}\alpha|^{3/2} + |\bar{i}\beta|^{3/2}} - \frac{1}{L} \cdot \frac{\bar{z}\alpha\bar{i}\alpha + \bar{z}\beta\bar{i}\beta}{|\bar{i}\alpha|^{3/2} + |\bar{i}\beta|^{3/2}} \right\}, \quad (14)$$

where sup represents the upper bound.

When the current of the system converges in finite time, namely, $\bar{i}\alpha = \bar{i}\alpha = \bar{i}\beta = \bar{i}\beta = 0$, from (10) that

$$\left\{ \begin{aligned} \text{sign}(\bar{i}\alpha) &= -\frac{\bar{z}\alpha}{M \cdot L \cdot |\bar{i}\alpha|^{1/2}}, \\ \text{sign}(\bar{i}\beta) &= -\frac{\bar{z}\beta}{M \cdot L \cdot |\bar{i}\beta|^{1/2}}. \end{aligned} \right. \quad (15)$$

By combining (11) and (15), we get

$$\left\{ \begin{aligned} \dot{\hat{z}}\alpha &= -\frac{N \cdot \bar{z}\alpha}{M \cdot L \cdot |\bar{i}\alpha|^{1/2}}, \\ \dot{\hat{z}}\beta &= -\frac{N \cdot \bar{z}\beta}{M \cdot L \cdot |\bar{i}\beta|^{1/2}}. \end{aligned} \right. \quad (16)$$

By deriving (2), we get

$$\left. \begin{aligned} \dot{z}\alpha &= -\psi f \omega e \cos \theta e = -z\beta \omega e \\ \dot{z}\beta &= -\omega e \psi f \sin \theta e = z\alpha \omega e \end{aligned} \right\}. \quad (17)$$

(16) and (17) can be subtracted:

$$\left\{ \begin{aligned} \dot{\bar{z}}\alpha &= -\frac{N \cdot \bar{z}\alpha}{M \cdot L \cdot |\bar{i}\alpha|^{1/2}} + \omega e \cdot z\beta, \\ \dot{\bar{z}}\beta &= -\frac{N \cdot \bar{z}\beta}{M \cdot L \cdot |\bar{i}\beta|^{1/2}} - \omega e \cdot z\alpha. \end{aligned} \right. \quad (18)$$

Similarly, the Lyapunov function can define as

$$G2 = \frac{1}{2}(\bar{z}\alpha^2 + \bar{z}\beta^2). \quad (19)$$

By deriving (19), we get

$$\begin{aligned} \dot{G}2 &= -N \left[\frac{\bar{z}^2\alpha}{M \cdot L \cdot |\bar{i}\alpha|^{1/2}} + \frac{\bar{z}^2\beta}{M \cdot L \cdot |\bar{i}\beta|^{1/2}} \right] \\ &\quad + \omega e \cdot z\beta \cdot \bar{z}\alpha - \omega e \cdot z\alpha \cdot \bar{z}\beta. \end{aligned} \quad (20)$$

To ensure the convergence of SMO, namely, $G2 < 0$, N should be designed as

$$N > \sup \left\{ \frac{M \cdot L \cdot \omega e \cdot (z\beta \cdot \bar{z}\alpha - z\alpha \cdot \bar{z}\beta)}{(\bar{z}^2\alpha/|\bar{i}\alpha|^{1/2}) + (\bar{z}^2\beta/|\bar{i}\beta|^{1/2})} \right\}. \quad (21)$$

3.2. Design and Analysis of Adaptive Law. Compared with the traditional sliding mode control, the algorithm's control structure is simple and easy to implement. However, it can be seen from (9) and (15) that the observer's stability condition requires that the sliding mode gain is more significant than the supremum of a function about the control error. However, the control error cannot be determined in the existing system, so the system's stability condition cannot directly determine the sliding mode's selection range. So, in reality, we often try to choose more extensive parameters, which leads to the increase of system chattering, and even the system cannot usually run. When the sliding mode variable is near the sliding mode surface, the chattering of the system is increased due to the overestimation of the control gain, thus affecting the stability of the system. At

the same time, in order to prevent the sliding mode variable away from the sliding mode surface, because the control gain estimate is too small, the system rapidity is affected.

Therefore, in this paper, M and N are designed as sliding mode gains that change with the change of the back EMF, namely,

$$\begin{cases} M = \lambda_1 + \zeta_1 \sqrt{\bar{z}\alpha + \bar{z}\beta}, \\ N = \lambda_2 + \zeta_2 \sqrt{\bar{z}\alpha + \bar{z}\beta}, \end{cases} \quad (22)$$

where λ_1 and λ_2 are both small numbers greater than 0; ζ_1 and ζ_2 are adaptive coefficients more significant than 0, and it is shown in Figure 1.

Stability analysis is given as follows.

From (13), $-Rs/L(\bar{i}^2\alpha + \bar{i}^2\beta)$ and $-M(|\bar{i}\alpha|^{3/2} + |\bar{i}\beta|^{3/2})$ are terms that are always less than 0.

Therefore, a sufficient condition for the existence of (15) is constructed as follows:

$$\begin{aligned} & -\frac{Rs}{L}(\bar{i}^2\alpha + \bar{i}^2\beta) - \frac{1}{L}(\bar{z}\alpha\bar{i}\alpha + \bar{z}\beta\bar{i}\beta) - M(|\bar{i}\alpha|^{3/2} + |\bar{i}\beta|^{3/2}) < 0, \quad \bar{i}\alpha > 0, \bar{i}\beta > 0, \\ & -\frac{Rs}{L}(\bar{i}^2\alpha + \bar{i}^2\beta) - \frac{1}{L}(-\bar{z}\alpha\bar{i}\alpha - \bar{z}\beta\bar{i}\beta) - M(|\bar{i}\alpha|^{3/2} + |\bar{i}\beta|^{3/2}) < 0, \quad \bar{i}\alpha < 0, \bar{i}\beta < 0. \end{aligned} \quad (23)$$

Since $-Rs/L(\bar{i}^2\alpha + \bar{i}^2\beta) < 0$, $-M(|\bar{i}\alpha|^{3/2} + |\bar{i}\beta|^{3/2}) < 0$, it can be deduced that the condition satisfying $\dot{G}1 < 0$ is as follows:

$$N > \max(|z\alpha|, |z\beta|) = |\omega e|\psi f = \sqrt{\bar{z}\alpha + \bar{z}\beta}. \quad (24)$$

Therefore, N can be designed as

$$N = \lambda_2 + \zeta_2 \sqrt{\bar{z}\alpha + \bar{z}\beta}. \quad (25)$$

From (21), we can know $N > \sup\{M\}$. According to (21), M can be designed as

$$M = \lambda_1 + \zeta_1 \sqrt{\bar{z}\alpha + \bar{z}\beta}, \quad (26)$$

where λ_1 is less than λ_2 ; ζ_1 is less than ζ_2 .

4. Simulation

The vector control strategy $id = 0$ is adopted to establish the system simulation model based on MATLAB/Simulink to realize the sensorless control of SPMSM. Its principal block diagram is shown in Figure 2. Rated motor parameters used in the simulation are shown in Table 1.

The parameters of SMO are $k = 200$. The STA-SMO parameter configuration is $M = 5000$, $N = 35000$. The ASMO parameter configuration is $\lambda_1 = 235$, $\zeta_1 = 65$, $\lambda_2 = 3800$, $\zeta_2 = 450$.

The initial speed of the system is 600 r/min, and no load is started. At 0.05 s, 5 N m load torque is applied; at 0.1 s, the speed changes to 1000 r/min; in the first variable speed stable operation stage (0.15 s), the load torque changes to 10 N m;

at 0.2 s, the speed changes to 300 r/min; in the second variable speed stable operation stage (0.25 s), the load torque changes to 15 N·m.

From Figures 3 and 4 the response speed of STA-SMO and ASMO is faster than that of SMO, no matter in the motor start-up stage, speed shift stage, and load torque mutation stage. Especially at 0.2 s, when the speed decreases from 1000 r/min to 300 r/min, the SMO speed waveform has an obvious lag phenomenon due to introducing a low-pass filter. At 0.25 s, the torque load suddenly increases to 15 N·m, and the phenomenon of the rapid drop of SMO is apparent.

It can be seen that SMO is not as good as the previous two control strategies when dealing with external disturbances.

From Figures 3–5 and Table 2, compared with traditional SMO, the speed errors of ASMO at different speed stages are 2.65%, 3.51%, and 3.5% of SMO, respectively. Compared with STA-SMO, ASMO's speed errors at different speeds are 72.581%, 92.857%, and 59.231% of STA-SMO, respectively.

From the above results and the simulation figures analysis, it can be seen that the speed error of the three control strategies is proportional to the speed. SMO has the largest chattering and speed error, and the response speed is slow. Compared with SMO, STA-SMO, because of the function of integral function, can well suppress sliding mode chattering, reduce the rotation speed error, avoid the phenomenon of rotation speed waveform lag caused by the introduction of the low-pass filter, and enhance the response speed of the system. However, because the sliding mode gain is a fixed value, it cannot meet high precision speed regulation requirements. The sliding mode gain of the ASMO can

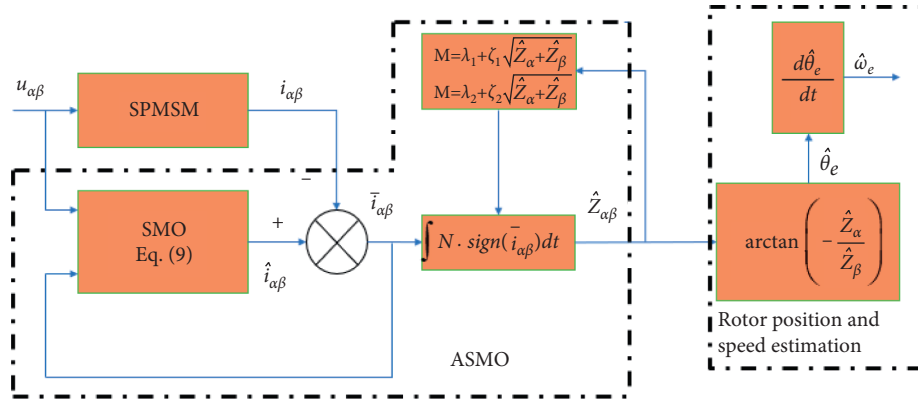


FIGURE 1: Block diagram of ASMO.

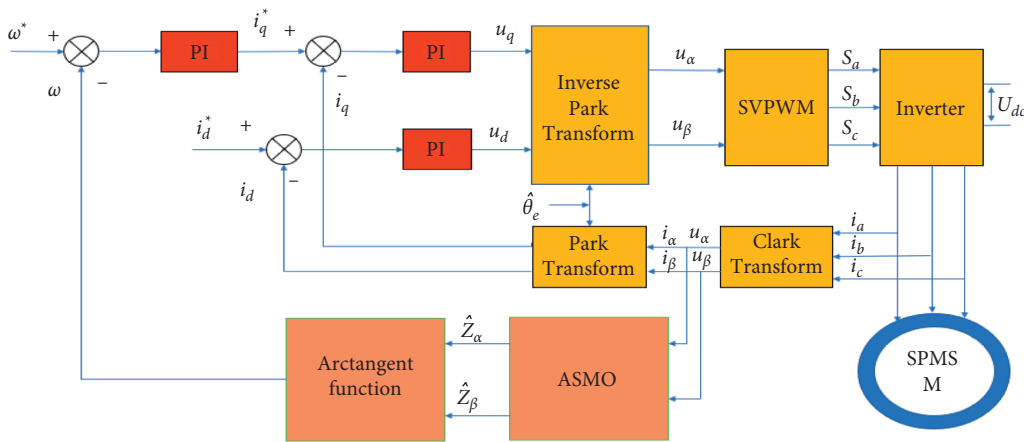


FIGURE 2: SPMSM speed sensor-less control block diagram of ASMO.

TABLE 1: Parameters of the SPMSM.

Quantity	Name of unit	Symbol
R_s	2.875	Ω
ψ_f	0.175	Wb
L	$8.5e^{-3}$	H
DC bus voltage	311	V
Rotational inertia	0.003	$kg\ m^2$
Rated power	2.3	kW
Rated speed	1000	r/min
Rated torque	15	N·m
Pole pairs numbers	4	

be adjusted online with speed, and the speed error and the speed waveform chattering can be minimized. The problem of excessive gain can be solved well, and the robustness of the system is enhanced.

From Table 3, the rotor position errors of ASMO at different speed segments are 29.13%, 4.69%, and 4% of SMO, respectively. Compared with STA-SMO, ASMO's rotor position errors at different speeds are 75%, 96.83%, and 55.56% of STA-SMO, respectively.

From Figures 6–9 and the analysis of the above results, the estimated rotor position waveform of SMO has obvious chattering. When the speed drops to 300 r/min, the

chattering is further aggravated, and the rotor position error is the largest, which seriously affects the system control accuracy. Compared with SMO, the rotor position error of STA-SMO is small, and the chattering phenomenon is weakened, but because its sliding mode gain is a fixed value when the speed is 300 r/min, the rotor position error increases, which is not conducive to the system high precision control needs. Compared with the above two control strategies, the ASMO rotor position error is the smallest, and under different disturbances, the estimated rotor position is the same as the actual rotor position. It satisfies the high precision control requirements of the system.

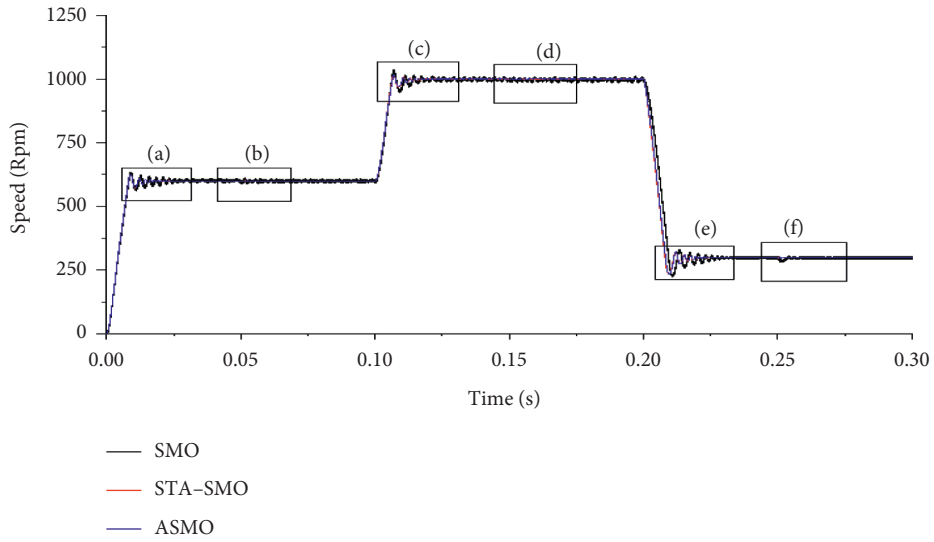


FIGURE 3: Speed response diagram.

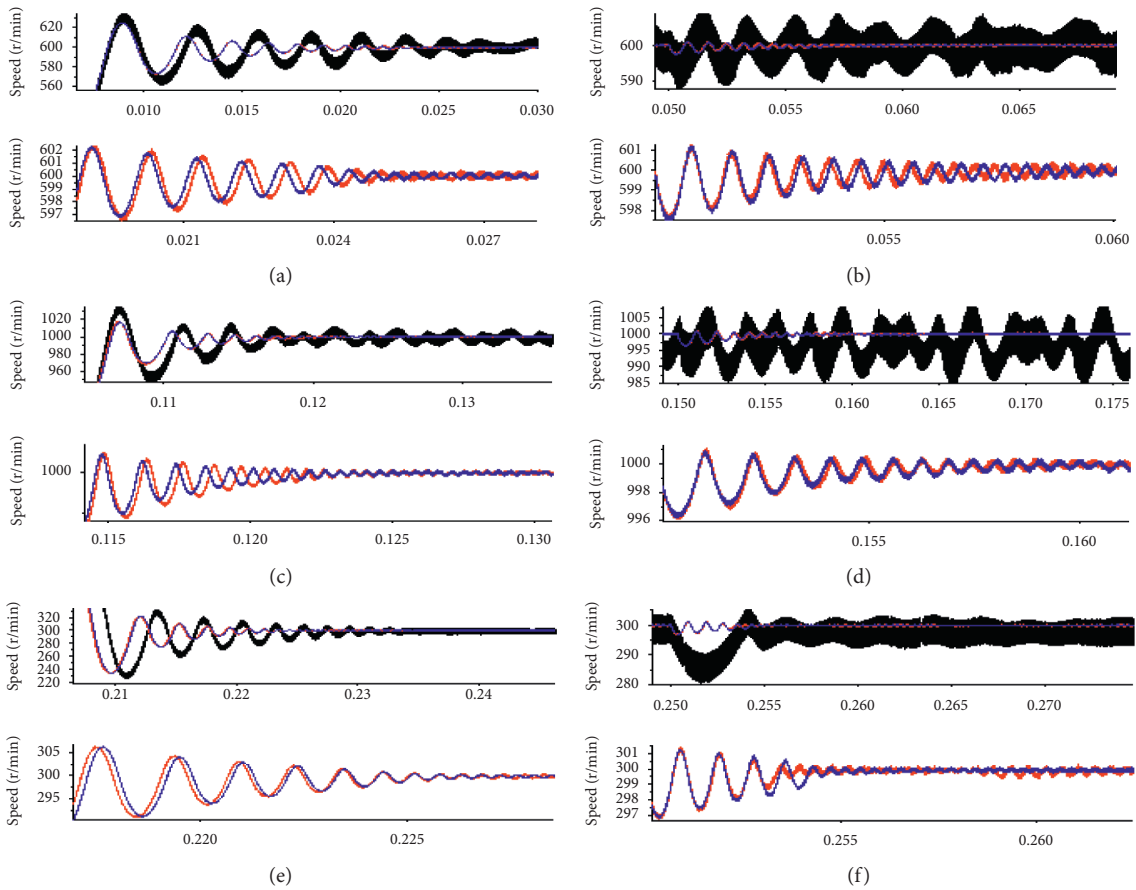


FIGURE 4: Enlargement of local speed.

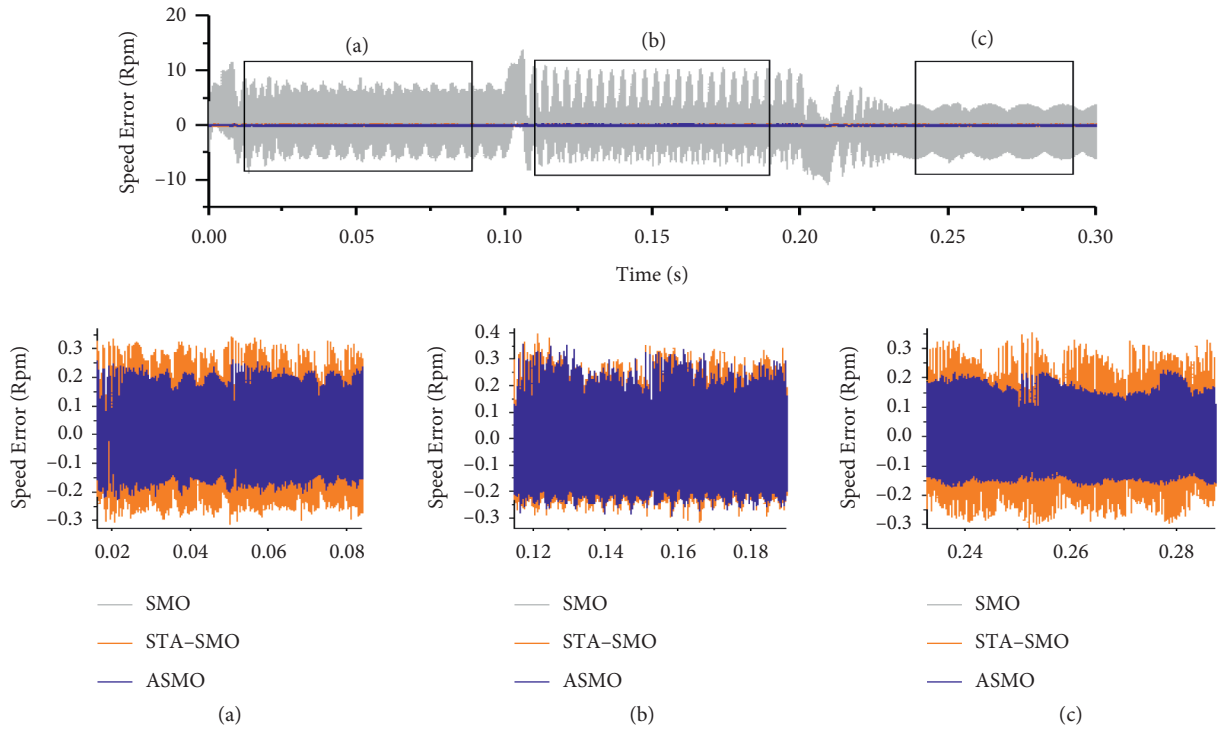


FIGURE 5: Speed error response diagram.

TABLE 2: Speed error.

Results	SMO	STA-SMO	ASMO	Symbol
Error (a)	17	0.62	0.45	r/min
Error (b)	18.5	0.7	0.65	r/min
Error (c)	11	0.65	0.385	r/min

TABLE 3: Rotor position error.

Results	SMO	STA-SMO	ASMO	Symbol
Error (a)	0.00206	0.0008	0.0006	Deg
Error (b)	0.013	0.00063	0.00061	Deg
Error (c)	0.025	0.0018	0.001	Deg

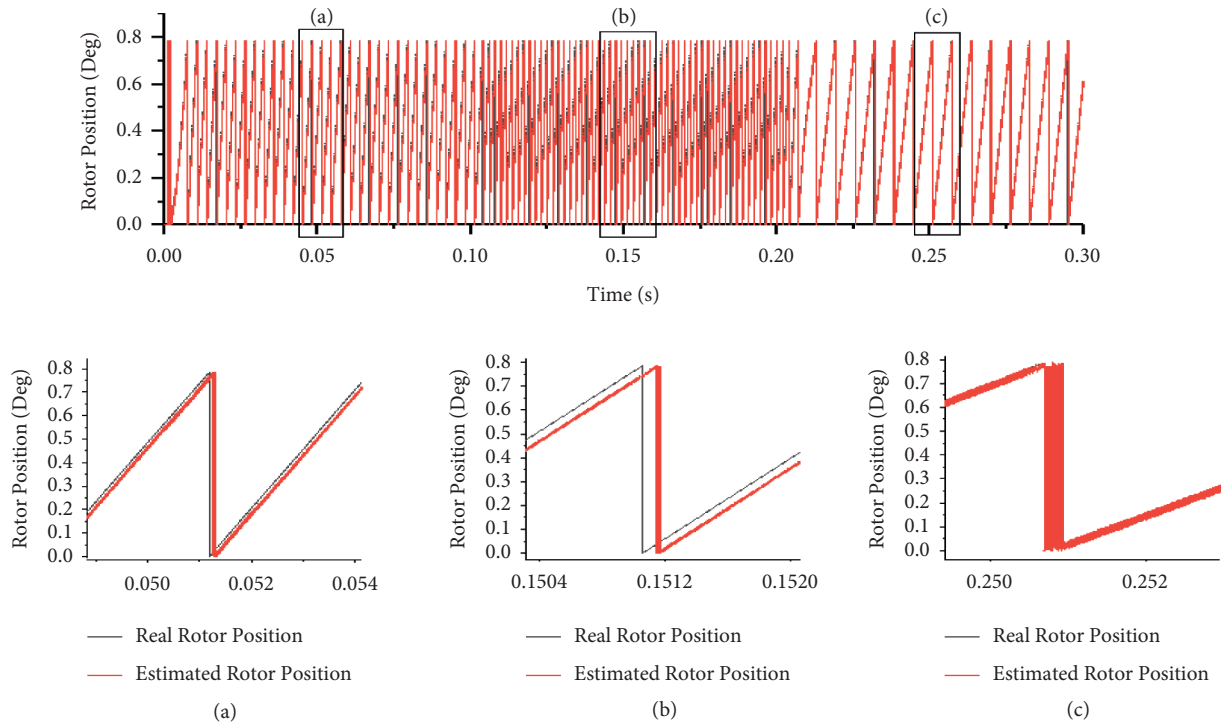


FIGURE 6: SMO rotor position response diagram.

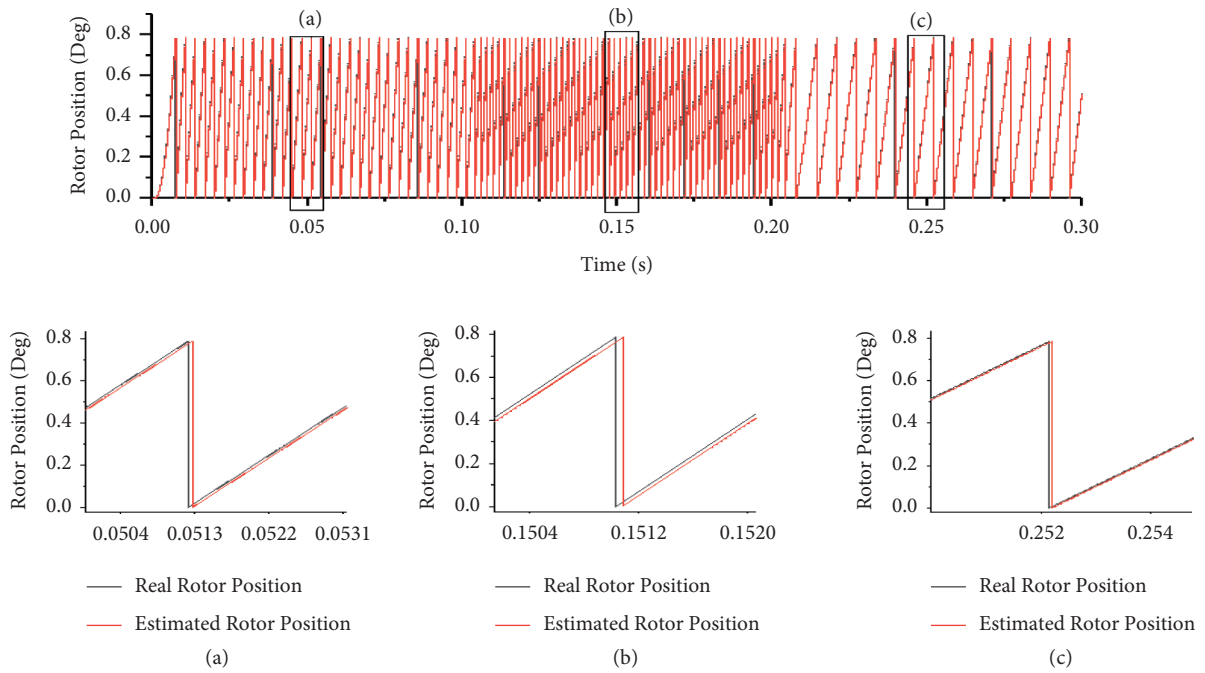


FIGURE 7: STA-SMO rotor position response diagram.

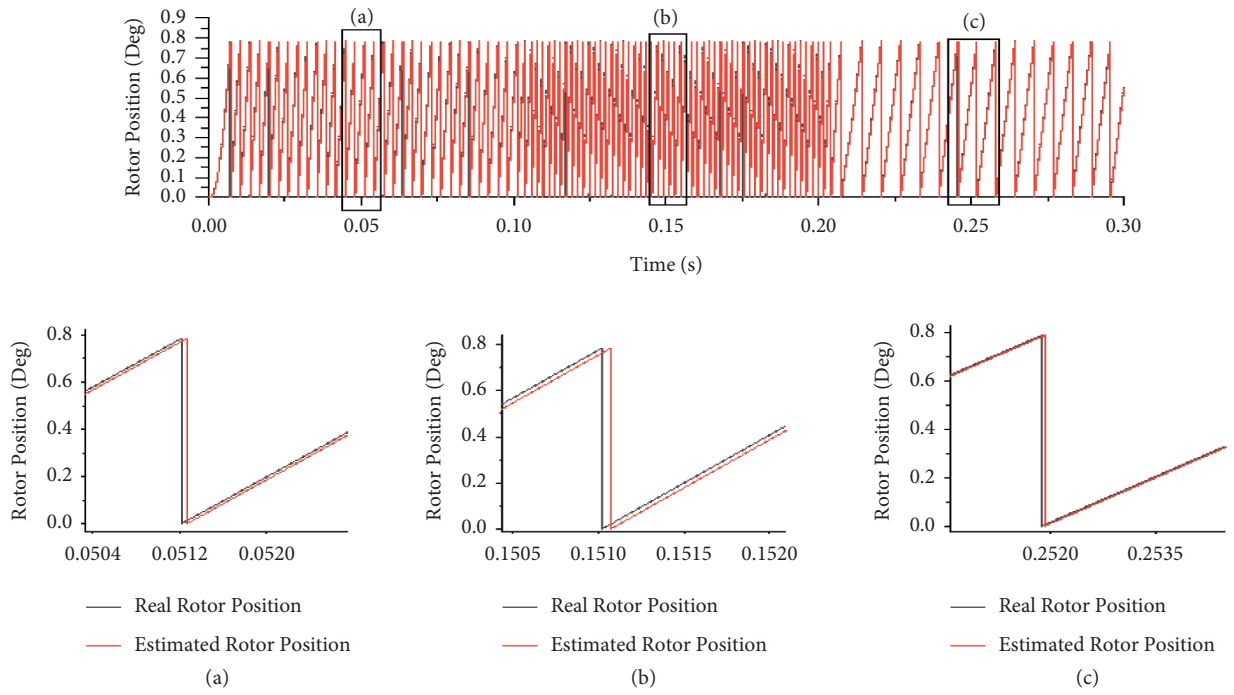


FIGURE 8: ASMO rotor position response diagram.

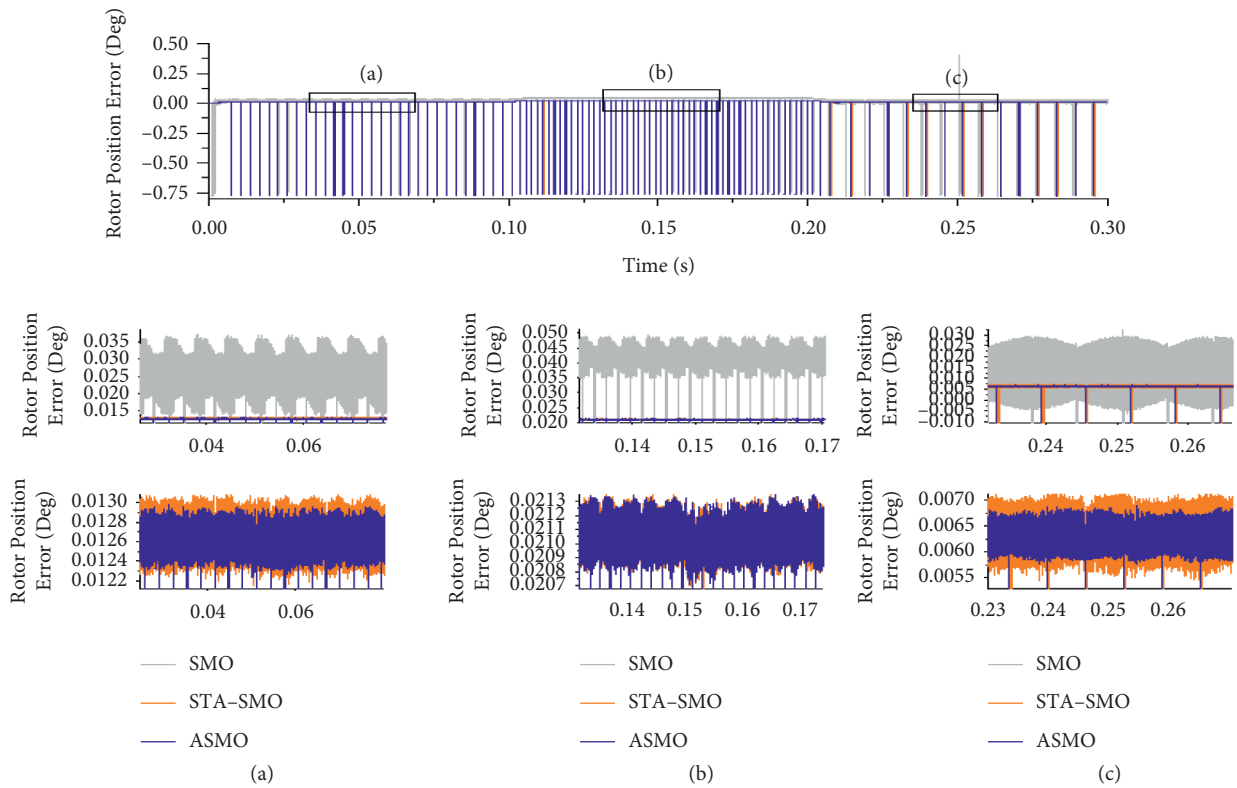


FIGURE 9: Rotor position error response diagram.

5. Conclusion

This paper presents a speed sensorless control technology of surface-mount permanent magnet synchronous motor based on ASMO. The proposed observer can effectively filter the high-frequency sliding mode noise when estimating the back EMF and avoid the lag caused by introducing the low-pass filter, thus reducing the system's complexity.

Secondly, to solve the difficulty of the observer's sliding mode gain, an adaptive law is designed that changes with the back EMF. By adjusting the sliding mode gain online, the control precision of the system is further enhanced.

Finally, by comparing with the simulation experiments of traditional SMO and STA-SMO control strategies, it can be seen that the proposed control strategy can effectively suppress sliding mode chattering, improve the accuracy of rotor position estimation, and better meet the requirements of the system speed regulation.

Data Availability

The data used to support the findings of this study are available from the corresponding author upon request.

Conflicts of Interest

The authors declare that they have no conflicts of interest.

References

- [1] L. Zhang, S. Wang, and J. Bai, "Fast -super -twisting Sliding Mode Speed Loop Control of Permanent Magnet Synchronous Motor Based on SVM -DTC," *IEICE Electronics Express*, vol. 18, no. 1, Article ID 20200375, 2021.
- [2] X. Zhang, L. Guo, S. Yang, and R. Cao, "Speed sensorless control of permanent magnet synchronous generator," *Proceedings of the CSEE*, vol. 34, no. 21, p. 3440, 2014.
- [3] K. Prabhakaran, K. Anbalagan, and F. Blaabjerg, "Laboratory Implementation of Electromagnetic Torque Based MRAS Speed Estimator for Sensorless SMPMSM drive," *Electronics Letters*, vol. 55, no. 21, pp. 1145–1147, 2019.
- [4] E. Dehghan-Azad, S. Gadoue, D. Atkinson, H. Slater, P. Barrass, and F. Blaabjerg, "Sensorless control of IM based on stator-voltage MRAS for limp-home EV applications," *IEEE Transactions on Power Electronics*, vol. 33, no. 3, pp. 1911–1921, 2018.
- [5] Y. A. Khan and V. Verma, "Stator resistance estimation for MRAS -based speed sensorless vector -controlled switched reluctance motor drive," *Electrical Engineering*, vol. 103, no. 4, pp. 1949–1963, 2021.
- [6] M. Nicola, C. I. Nicola, and D. Sacerdotianu, "Sensorless Control of PMSM using DTC Strategy Based on PI - ILC Law and MRAS Observer," in *Proceedings of the 2020 International Conference on Development and Application Systems (DAS)*, Suceava, Romania, May 2020.
- [7] P. Misra and B. Kumar, "Rotor Resistance Estimation for Improved Performance of MRAS -Based Sensorless Speed Estimation of Induction Motor Drives," *Intelligent Algorithms for Analysis and Control of Dynamical Systems*, Springer, Singapore, 2021.
- [8] Z. Yin, G. Li, Y. Zhang, and J. Liu, "Symmetric -strong -tracking -extended -kalman -filter -based sensorless control of induction motor drives for modeling error reduction," *IEEE Transactions on Industrial Informatics*, vol. 15, no. 2, pp. 650–662, 2018.
- [9] A. Farhan, A. Saleh, M. Abdelrahman, R. Kennel, and A. Shaltout, "High - Precision Sensorless Predictive Control of Salient - Pole Permanent Magnet Synchronous Motor Based -on Extended Kalman Filter," in *Proceedings of the 2019 21st International Middle East Power Systems Conference (MEPCON)*, IEEE, Cairo, Egypt, December 2019.
- [10] R. Inan and E. Zerdali, "Design of adaptive extended kalman filter-based speed-sensorless direct torque controlled drive system with constant switching frequency," *Pamukkale University Journal of Engineering Sciences*, vol. 26, no. 5, pp. 860–867, 2020.
- [11] M. L. Jayaramu, H. N. Suresh, M. S. B. Ranjana, D. Almakhlis, S. Padmanaban, and U. Subramaniam, "Real -Time Implementation of Adaptive Extended Kalman Filter Observer with Improved Speed Estimation for Sensorless Control," *IEEE Access*, vol. 9, pp. 50452–50465, 2020.
- [12] Y. Yan, S. Yu, Z. Yang, and J. Du, "Continuous Finite -Time Observer -Controller Based Speed Regulation of Permanent Magnet Synchronous Motors," in *Proceedings of the Advanced Intelligent Computing, Lecture Notes in Computer Science ICIC 2011*, Zhengzhou, China, August 2011.
- [13] Y. H. Kim, F. L. Lewis, and C. T. Abdallah, "A dynamic recurrent neural-network-based adaptive observer for a class of nonlinear systems," *Automatica*, vol. 33, no. 8, pp. 1539–1543, 1997.
- [14] R. Xi, Z. Yang, and X. Xiao, "Adaptive neural network observer based PID -backstepping terminal sliding mode control for robot manipulators," in *Proceedings of the 2020 IEEE/ASME International Conference on Advanced Intelligent Mechatronics (AIM)*, IEEE, Boston, MA, USA, July 2020.
- [15] J. Sun, G.-Z. Cao, S.-D. Huang, Y. Peng, J. He, and Q.-Q. Qian, "Sliding-mode-observer-based position estimation for sensorless control of the planar switched reluctance motor," *IEEE Access*, vol. 7, pp. 61034–61045, 2019.
- [16] C. M. Verrelli, S. Bifaretti, E. Carfagna et al., "Speed Sensor Fault Tolerant PMSM Machines: from Position - sensorless to Sensorless Control," *IEEE Transactions on Industry Applications*, vol. 55, no. 4, pp. 3946–3954, 2019.
- [17] F. Zhao, W. Luo, F. Gao, and J. Yu, "Position sensorless hybrid control of permanent magnet synchronous motor based on fuzzy sliding mode controller and two -stage filter observer," *Control Theory & Applications*, vol. 37, no. 8, pp. 196–203, 2020.
- [18] Z. Hua -Qiang, S. Feng -Ming, and Y. Tong, "Research and Optimization of Speed Control System of PMSM Sliding Mode Observer," *Power Electronics*, 2019.
- [19] Y. Zhang, Z. Yin, Y. Zhang, J. Liu, and X. Tong, "A novel sliding mode observer with optimized constant rate reaching law for sensorless control of induction motor," *IEEE Transactions on Industrial Electronics*, vol. 67, no. 7, pp. 5867–5878, 2020.
- [20] N. Cai, Y. Jing, and S. Zhang, "Synchronization of the unified chaotic systems with disturbance and uncertainty," in *Proceedings of the 2009 Chinese Control and Decision Conference*, pp. 804–808, Guilin, China, June 2009.
- [21] Y. Yong Feng, J. Jianfei Zheng, X. Xinghuo Yu, and fnm Nguyen Vu Truong, "Hybrid terminal sliding-mode observer design method for a permanent-magnet synchronous motor control system," *IEEE Transactions on Industrial Electronics*, vol. 56, no. 9, pp. 3424–3431, 2009.
- [22] D. Liang, J. Li, and R. Qu, "Super -twisting Algorithm Based Sliding Mode Observer for Wide -speed Range PMSM

- Sensorless Control Considering VSI nonlinearity,” in *Proceedings of the 2017 IEEE International Electric Machines and Drives Conference (IEMDC)*, IEEE, Miami, Florida, USA., May 2017.
- [23] S. D. Gennaro, J. Rivera, and B. Castillo -Toledo, “Super - twisting sensorless control of permanent magnet synchronous motors,” in *Proceedings of the 49th IEEE Conference on Decision & Control*, IEEE, Atlanta, GA, USA, December 2010.
- [24] A. Borkar and P. M. Patil, “Super twisting observer based full order sliding mode control,” *International Journal of Dynamics and Control*, vol. 9, no. 4, pp. 1653–1659, 2021.
- [25] R. Ma, Y. Han, and W. Pan, “Variable-gain super-twisting sliding mode damping control of series-compensated DFIG-based wind power system for SSCI mitigation,” *Energies*, vol. 14, no. 2, p. 382, 2021.
- [26] R. J. . Rong-Jong Wai, “Total sliding-mode controller for PM synchronous servo motor drive using recurrent fuzzy neural network,” *IEEE Transactions on Industrial Electronics*, vol. 48, no. 5, pp. 926–944, 2001.
- [27] C. Liji, Y. Baosheng, and M. A. Qiang, “Design of PMSM Sliding Mode Observer Based on Fuzzy RBF Neural Network,” *Electric Machines & Control Application*, vol. 46, no. 9, pp. 66–71, 2019.
- [28] S. Wu, J. Zhang, and B. Chai, “Adaptive Super-twisting Sliding Mode Observer Based Robust Backstepping Sensorless Speed Control for IPMSM,” *ISA Transactions*, vol. 92, pp. 155–165, 2019.
- [29] L. Guo, Z. Xing, S. Yang, X. Zhen, and L. Wang, “Super-twisting sliding mode observer based speed sensorless torque control for PMSG used in wind turbines,” in *Proceedings of the International Conference on Power Electronics & Ecce Asia*, IEEE, Seoul, Korea (South), June 2015.
- [30] L. Guo, *Research on Driving Technology of High Power Permanent Magnet Direct Drive Wind Power Generation System*, Hefei University of Technology, Hefei, China, 2016.

Research Article

A Novel Family of Exact Nonlinear Cascade Control Design Solutions for a Class of UAV Systems

Kristian Maya-Gress ¹, **Jorge Álvarez** ², **Raúl Villafuerte-Segura** ¹,
Hugo Romero-Trejo ¹ and **Miguel Bernal** ²

¹Research Center on Information Technology and Systems, Hidalgo State University, Pachuca-Hidalgo C. P. 42184, Mexico

²Department of Electrical and Electronics Engineering of the Sonora Institute of Technology, 5 de Febrero 818 Sur, Cd. Obregon C. P. 85000, Mexico

Correspondence should be addressed to Miguel Bernal; miguel.bernal@itson.edu.mx

Received 13 July 2021; Revised 7 September 2021; Accepted 13 November 2021; Published 29 November 2021

Academic Editor: Antonios Tsourdos

Copyright © 2021 Kristian Maya-Gress et al. This is an open access article distributed under the Creative Commons Attribution License, which permits unrestricted use, distribution, and reproduction in any medium, provided the original work is properly cited.

In this work, a novel family of exact nonlinear control laws is developed for trajectory tracking of unmanned aerial vehicles. The proposed methodology exploits the cascade structure of the dynamic equations of most of these systems. In a first step, the vehicle position in Cartesian coordinates is controlled by means of fictitious inputs corresponding to the angular coordinates, which are fixed to a combination of computed torque and proportional-derivative elements. In a second step, the angular coordinates are controlled as to drive them to the desired fictitious inputs necessary for the first part, resulting in a double-integrator 3-input cascade control scheme. The proposal is put at test in two examples: 4-rotor and 8-rotor aircrafts. Numerical simulations of both plants illustrate the effectiveness of the proposed method, while real-time results of the first one confirm its applicability.

1. Introduction

Unmanned aerial vehicles (UAVs) have become a topic of interest in many works due to the fact that they are capable of operating in degraded environments which might be dangerous for humans. These vehicles are designed to fly with high agility and rapid maneuvering, even under wind gusts. For all these qualities, the UAVs have a wide variety of applications such as military [1], 3D mapping and aerial photography [2, 3], and inspection of places that are not easily accessible or are too dangerous for humans [4], among others [5, 6].

There is a great variety of UAVs that can be classified by a broad number of performance characteristics such as their structure, weight, endurance, range, speed, and so on [7]. In this work, we will focus on plants with a cascade structure that allows for a family of novel cascade nonlinear control laws to be applied, e.g., the quadrotor and the 8-rotor aircrafts. These plants consist in a structure of symmetrical links and 4 or 8 rotors at its ends, respectively. In the case of

the quadrotor, given that the front and the rear motors rotate counter-clockwise while the other two rotate clockwise, gyroscopic effects and aerodynamic torques tend to cancel during flight. A similar situation is produced in the 8-rotor aircraft. Both plants include the rotation motion of three axes and the linear motion of the center of gravity along three axes. Thus, there are six motions: back/front, left/right, up/down, yaw, pitch, and roll. The quadrotor has 4 control inputs and 6 degrees of freedom; its dynamics has the characteristics of nonlinearity and strong coupling [8]. On the other hand, the 8-rotor has 6 control inputs and 6 degrees of freedom [9].

In the literature, there are many works about control laws applied to UAVs. Most of them do not require precise or complete knowledge of the dynamic equations of the plant. Indeed, one of the most basic control structures, the family of proportional-integral-derivative (PID) controllers, which requires tuning of its gains, can be applied successfully to these plants as they are capable of bringing the error signals to zero in trajectory tracking [10–12]. Other reports

incorporate fuzzy logic in combination with PID controllers, thus easing the tuning of the gains and increasing the adaptability of the control law to changing plant or environment parameters; they usually have better performance than classic PID [13–16]. Dead-zone and actuator faults have also been studied in this context [17]. Recent works present solutions based on neural networks for the autonomous landing of a quadrotor both on fixed and moving targets for maritime search-and-rescue applications [18]. In [19], a neural network adaptive scheme is combined with sliding mode control, which preserves the advantages of both methods, namely, adaptability and robustness against coupled perturbations.

On the other hand, there are also control laws that require knowledge of the plant, such as linear quadratic regulator (LQR) techniques that can be found in [20], where a linearization of the plant is necessary to design the controller; nonlinear dynamic models based on quaternions for attitude and LQR control are presented in [21]; in [22], a controller design using the backstepping approach has been applied to the state-space model of a quadrotor, while in [23], the model is used in the Lagrange–Euler form; in [24], a backstepping control and nonlinear disturbance observer have been developed; the observer is constructed separately from the controller to estimate the external disturbances and compensate for the negative effects of the disturbances such as wind gusts.

Yet, another category of controllers uses partial information of the model, e.g., sliding modes in [25–27], which besides being robust and simple, produces high-frequency switching of the control signals (chattering phenomenon); integral predictive and nonlinear robust \mathcal{H}_∞ strategy [28], where the integral of the position error is considered, allowing the achievement of a null steady-state error when sustained disturbances are acting on the system; and a hybrid finite-time control approach [29] for trajectory tracking with unknown dynamics and disturbances. Furthermore, many recent works have shown different approaches for trajectory tracking of the quadrotor such as finite-time output feedback schemes [30], adaptive control [31, 32], supertwisting [33], active disturbance rejection [34], and neural networks with backstepping [35].

1.1. Contribution. The contribution of this article is to provide a family of exact nonlinear cascade control schemes for UAV plants such as the quadrotor and the 8-rotor aircraft, which, due to their characteristics, have a cascade interconnection of groups of states. In contrast with other schemes in the literature, the control laws are exact, not approximate, and allow a variety of options to be easily incorporated via linear matrix inequalities (LMIs) [36], which are efficiently solved via convex optimization software [37].

1.2. Organization. The remainder of this study is organized as follows: Section 2 defines the family of systems to be studied, the basics on the computed torque technique, the mathematical models of the UAVs under study, and the

difficulties for implementing a computed torque-like control scheme: a problem statement is made; in Section 3, the main results concerning the family of exact nonlinear cascade controllers are presented; in Section 4, numerical simulations are provided proving the flexibility and efficiency of the control proposal; real-time results are shown in Section 5; and finally, conclusions are gathered in Section 6 along with a discussion on future work.

2. Preliminaries

This section describes the mathematical structure expected for the plants under consideration, the specific dynamic models of the two UAVs that will be used for illustration of the proposal, basics on the computed torque technique, and the problem statement of this work.

2.1. Cascade Plants. The plants under consideration must have one or more nested cascade structures of the following form:

$$\begin{aligned}\eta(t) &= f(\xi, u_1), \\ \xi(t) &= u_2,\end{aligned}\tag{1}$$

where $\eta \in \mathbb{R}^{n-p}$ and $\xi \in \mathbb{R}^p$ are associated with the plant states; the control inputs are $u_1 \in \mathbb{R}^{m-p}$ and $u_2 \in \mathbb{R}^p$; $f: \mathbb{R}^p \times \mathbb{R}^{m-p} \rightarrow \mathbb{R}^{n-p}$ is a sufficiently smooth nonlinear function in a domain D that contains the origin $(\eta, \xi) = (0, 0)$ with $f(0, 0) = 0$. As it will be seen later, UAVs belong to the former class as η is usually associated with Cartesian coordinates, ξ stands for the angular coordinates, u_1 and u_2 are usually the result of a simplification of the original inputs (i.e., from the voltage/speed inputs to the minimum number of torque ones), and $f(\cdot, \cdot)$ is clearly a nonlinear input distribution vector from the point of view of ξ and u_1 ; this point of view will be exploited later.

Most UAVs require trajectory tracking in the Cartesian coordinate space; therefore, following the analogy established between the model (1) and a UAV model, it is clear that trajectory tracking reduces to find inputs such that $\eta(t)$ is asymptotically driven to a desired trajectory $\eta_d(t)$. Note that, despite the cascade structure, backstepping is not directly applicable as the double-integrator and strong coupling of states in the first equation, precludes the designer from following the usual path. Indeed, most UAVs do not have polynomial coupling of states, but trigonometric ones. This means that backstepping cannot be performed as normally done because the required fictitious inputs cannot be straightforwardly determined [38].

Moreover, backstepping asymptotic stability of the origin is guaranteed via the direct Lyapunov method. But trajectory tracking requires writing the dynamic equations of the tracking error system in a form suitable for Lyapunov analysis, i.e., given the tracking error $e(t) = \eta_d(t) - \eta(t)$, being able to write

$$\begin{aligned}e(t) &= \eta_d(t) - \eta(t) = \eta_d(t) - f(\xi, u_1) \\ &= F(\eta, \dot{\eta}, \eta_d, \dot{\eta}_d, \xi, u_1)e(t),\end{aligned}\tag{2}$$

where, obviously, the form of $F(\cdot)$ might be very hard or impossible to obtain. The methodology to be presented in this study will circumvent this problem; once this is done, if a system can be put in a series of cascade connections such as the one presented above, the technique can be recursively applied.

2.2. UAV Dynamic Models. Since the UAVs employed for illustration of our proposal have similar underlying physical principles, we will focus on the development of the quadrotor model. This is standard material which, nevertheless, may help the reader understanding the origin and meaning of certain terms in the model.

The configuration of the quadrotor is composed by a rigid cross frame and four rotors as shown in Figure 1. The quadrotor is an underactuated and nonlinear coupled system with six degrees of freedom; its mathematical model will be obtained using the well-known Lagrangian method. To this end, let us define $q = (\eta, \xi) \in \mathbb{R}^6$ as the generalized coordinates vector for the quadrotor, where $\eta = (x, y, z) \in \mathbb{R}^3$ is the position of the center of mass of the quadrotor relative to the frame \mathcal{R}_o (Figure 1), and $\xi = (\psi, \theta, \phi) \in \mathbb{R}^3$ are the Euler angles (yaw, pitch, and roll) that describe the orientation of the aircraft. The kinetic energy of both translational and rotational motions are expressed, respectively, as

$$\begin{aligned} T_{\text{tra}} &= \frac{m}{2} \dot{\eta}^T \dot{\eta}, \\ T_{\text{rot}} &= \frac{1}{2} \dot{\xi}^T J \dot{\xi}, \end{aligned} \quad (3)$$

where m denotes the mass of the aircraft, and $J = W_n^T \mathcal{F} W_n$ is the inertia matrix for the rotational kinetic energy, with

$$\begin{aligned} W_n &= \begin{bmatrix} -\sin \theta & 0 & 1 \\ \sin \phi \cos \theta & \cos \phi & 0 \\ \cos \phi \cos \theta & -\sin \phi & 0 \end{bmatrix}, \\ \mathcal{F} &= \begin{bmatrix} I_{xx} & 0 & 0 \\ 0 & I_{yy} & 0 \\ 0 & 0 & I_{zz} \end{bmatrix}. \end{aligned} \quad (4)$$

The only force that contributes to the potential energy is the force due to gravitational acceleration, which is expressed as $U = mgz$, where z is the altitude of the quadrotor, and g is the gravitational constant. Thus, the Lagrangian is given by

$$\mathcal{L}(q, \dot{q}) = T_{\text{tra}} + T_{\text{rot}} - U = \frac{m}{2} \dot{\eta}^T \dot{\eta} + \frac{1}{2} \dot{\xi}^T J \dot{\xi} - mgz. \quad (5)$$

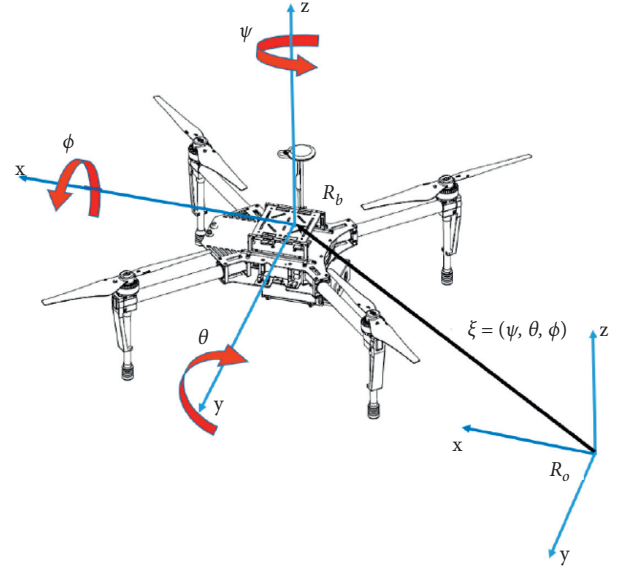


FIGURE 1: Scheme of the quadrotor system.

Considering the Euler-Lagrange equations and taking into account the vector of generalized external forces, the dynamic model of the quadrotor is defined as

$$\frac{d}{dt} \frac{\partial \mathcal{L}}{\partial \dot{q}} - \frac{\partial \mathcal{L}}{\partial q} = F, \quad (6)$$

where $F = [F_\eta^T \ \tau^T]^T$ is the vector of generalized forces. F_η groups the forces produced by the control inputs that produce a translational movement, and τ is the vector of generalized moments produced by the control inputs to perform rotational movements. The small body forces are ignored due to their being much smaller compared to the forces produced by the main control inputs. Then, the forces applied to the quadrotor with respect to the reference \mathcal{R}_b are given by

$$\begin{aligned} F_b &= \begin{bmatrix} 0 \\ 0 \\ u \end{bmatrix}, \\ \tau &= \begin{bmatrix} \tau_\psi \\ \tau_\theta \\ \tau_\phi \end{bmatrix}, \end{aligned} \quad (7)$$

where $u = f_1 + f_2 + f_3 + f_4$, $f_i = k_i w_i^2$ for $i = 1, 2, 3, 4$, and k_i , a positive constant parameter depending on the density of air, and w_i is the angular speed of the i^{th} motor. This set of forces expressed in \mathcal{R}_o is transformed into

$$F_\eta = \mathbf{R} F_b, \quad \text{with } \mathbf{R} = \begin{bmatrix} \cos \theta \cos \psi & \sin \phi \sin \theta \cos \psi - \sin \psi \cos \phi & \sin \psi \sin \phi + \sin \theta \cos \phi \cos \psi \\ \sin \psi \cos \theta & \sin \phi \sin \theta \sin \psi + \cos \phi \cos \psi & \sin \theta \sin \psi \cos \phi - \sin \phi \cos \psi \\ -\sin \theta & \sin \phi \cos \theta & \cos \phi \cos \theta \end{bmatrix}, \quad (8)$$

where \mathbf{R} is the transformation matrix representing the orientation of the quadrotor from \mathcal{R}_b to \mathcal{R}_o . Furthermore, the vectors of generalized moments acting on variables ξ are as follows:

$$\begin{aligned}\tau_\psi &= \sum_1^4 k_{Mi} w_i^2, \\ \tau_\theta &= (f_2 - f_4)l_c, \\ \tau_\phi &= (f_3 - f_1)l_c,\end{aligned}\quad (9)$$

where k_{Mi} is the moment constant of the i^{th} motor, and l_c is the distance between the axes of the motors and the center of gravity. Since the Lagrangian (5) does not contain any cross-term combining η and ξ , the Euler–Lagrange equation (6) can be split into two subsystems, one for the translational dynamics η and the other for the rotational dynamics ξ as follows:

$$\begin{aligned}m\eta + [0 \ 0 \ mg]^T &= F_\eta, \\ J\dot{\xi} + C(\xi, \dot{\xi})\dot{\xi} &= \tau,\end{aligned}\quad (10)$$

where $C(\xi, \dot{\xi})$ is the Coriolis matrix. In order to simplify the analysis, the following change of the input variables is proposed:

$$\tau = C(\xi, \dot{\xi})\dot{\xi} + J\tilde{\tau}. \quad (11)$$

Here, $\tilde{\tau} = [\tilde{\tau}_\psi \ \tilde{\tau}_\theta \ \tilde{\tau}_\phi]^T$ are the new inputs ([8] for details). Then, $\xi = \tilde{\tau}$ and equation (10) are rewritten as

$$\begin{aligned}x &= \frac{(\sin \phi \sin \psi + \sin \theta \cos \phi \cos \psi)u}{m}, \\ y &= \frac{(\sin \theta \sin \psi \cos \phi - \sin \phi \cos \psi)u}{m}, \\ \ddot{z} &= \frac{(\cos \theta \cos \phi)u}{m} - g, \\ \psi &= \tilde{\tau}_\psi, \\ \ddot{\theta} &= \tilde{\tau}_\theta, \\ \phi &= \tilde{\tau}_\phi,\end{aligned}\quad (12)$$

where the horizontal plane coordinates are represented by (x, y) , the vertical position is represented by z , ψ is the yaw angle around the z axis, θ is the pitch angle around the y axis, and ϕ is the roll angle around the x axis. The system (12) has four control inputs u , $\tilde{\tau}_\psi$, $\tilde{\tau}_\theta$, and $\tilde{\tau}_\phi$.

2.3. Computed Torque. Computed torque control is a technique used for trajectory tracking in rigid robotic manipulators consisting of open kinematic chains [39]. This sort of models is amenable to the Lagrange–Euler form:

$$M(q)\dot{q}(t) + V(q, \dot{q}) + F(q, \dot{q}) + G(q) = \tau(t), \quad (13)$$

where $q \in \mathbb{R}^n$ is a vector gathering the n joint variables of the kinematic chain, $M(q) \in \mathbb{R}^{n \times n}$ is the inertia matrix, $V(q, \dot{q}) \in \mathbb{R}^n$ is the Coriolis vector, $F(q, \dot{q}) \in \mathbb{R}^n$ accounts for the friction forces (whether viscous, dry, or others), $G(q) \in \mathbb{R}^n$ is the gravity vector, and $\tau(t) \in \mathbb{R}^n$ is the generalized force vector. Traditional computed torque control considers the plant as fully actuated, i.e., all entries in $\tau(t)$ are available for control purposes or it has one available actuator per joint. A desired trajectory $q_d(t)$ can be asymptotically tracked by $q(t)$ if the following control law is used:

$$\tau(t) = M(q)(\dot{q}_d(t) - u(t)) + V(q, \dot{q}) + F(q, \dot{q}) + G(q), \quad (14)$$

where $u(t)$ is responsible for stabilizing the tracking error system:

$$\begin{bmatrix} \dot{e}(t) \\ e(t) \end{bmatrix} = \begin{bmatrix} 0 & I \\ 0 & 0 \end{bmatrix} \begin{bmatrix} e(t) \\ \dot{e}(t) \end{bmatrix} + \begin{bmatrix} 0 \\ I \end{bmatrix} u(t), \quad (15)$$

with $e(t) = q_d(t) - q(t)$. Control law (14) is known as the inner-loop control feedback; it is based on exact feedback linearization [40]. Control law $u(t)$ is known as the outer-loop control feedback; it stabilizes the error system (15), a task usually achieved by linear state feedback or PD control:

$$u(t) = -K_p e(t) + K_v \dot{e}(t), \quad (16)$$

where for simplicity, gains K_p and K_v are the diagonal constant matrices with positive entries.

Clearly, computed torque is critically dependent on the precise knowledge of the model and does not take advantage of the nonlinear structure of the plant, let alone the cascade form of UAV models.

2.4. Problem Statement. For a UAV model of the form (1) to perform trajectory tracking of a Cartesian path $\eta_d(t) = [x_d(t) \ y_d(t) \ z_d(t)]$ by means of its inputs u_1 and u_2 , i.e., $\lim_{t \rightarrow \infty} e(t) = 0$ with $e(t) = \eta_d(t) - \eta(t)$, $\eta(t) = [x(t) \ y(t) \ z(t)]$, $\xi = [\psi \ \theta \ \phi]$, backstepping is not a straightforward option. Indeed, the double-integrator and the trigonometric functions in ξ impede its application.

Moreover, computed torque cannot be applied either because, following its notation, the joint vector $q = [x \ y \ z \ \psi \ \theta \ \phi]^T$ and the generalized force vector $\tau = [u \ \tilde{\tau}_\psi \ \tilde{\tau}_\theta \ \tilde{\tau}_\phi]^T$ do not share dimensions, i.e., there is not enough number of actuators as required by the computed torque technique.

In the next section, a novel family of exact nonlinear control laws is developed for trajectory tracking of UAVs; it will exploit the cascade structure without recurring to backstepping and will be able to deal with the underactuated characteristics that the computed torque technique is unable to cope. In contrast with other proposals, no approximations are employed; all the nonlinearities are taken into account for control purposes.

Notation: in matrix expressions, 0 and I stand for a zero and identity matrix, respectively, whose dimensions can be inferred from the context; $>$ and $<$ stand for positive and

negative-definiteness; the symbol $(*)$ denotes the transpose of the expression on the left, i.e., $A + (*) = A + A^T$.

3. Main Results

In this section, a family of nonlinear cascade controllers for trajectory tracking of UAVs with cascade model structure is proposed. To begin with, we reproduce the general mathematical model of the UAVs under consideration:

$$\begin{aligned} \eta(t) &= f(\xi, u_1), \\ \xi(t) &= u_2, \end{aligned} \quad (17)$$

where $\eta \in \mathbb{R}^3$ and $\xi \in \mathbb{R}^3$ are associated with Cartesian and angular coordinates, respectively; the simplified control inputs are $u_1 \in \mathbb{R}^m$ and $u_2 \in \mathbb{R}^3$; $f(\cdot, \cdot): \mathbb{R}^3 \times \mathbb{R}^m \rightarrow \mathbb{R}^3$ is a sufficiently smooth nonlinear function in a domain D that contains the origin $(\eta, \xi) = (0, 0)$ with $f(0, 0) = 0$.

Consider a desired trajectory in Cartesian coordinates $\eta_d \in \mathbb{R}^3$ such that $\eta_d(t) = [x_d(t) \ y_d(t) \ z_d(t)]^T$, where $x_d(t)$, $y_d(t)$, and $z_d(t)$ are the desired trajectories in the direction of the x , y , and z axis, respectively; let the corresponding tracking error be $e_\eta(t) = \eta_d(t) - \eta(t)$; thus, taking into account (17), we have

$$e_\eta(t) = \eta_d(t) - \eta(t) = \eta_d(t) - f(\xi, u_1), \quad (18)$$

$$\xi(t) = u_2. \quad (19)$$

Thanks to the cascade structure above, the following assumption can be made:

Assumption 1. There exists ξ_d and u_1 such that

$$\eta_d - f(\xi, u_1) = -K_{p\eta}e_\eta - K_{v\eta}\dot{e}_\eta, \quad (20)$$

where $K_{p\eta} \in \mathbb{R}^{3 \times 3}$ and $K_{v\eta} \in \mathbb{R}^{3 \times 3}$ are the matrices with proportional and derivative gains, respectively, to be defined (usually diagonal with positive entries); otherwise, claim the approach fails.

Despite its complexity, note that the existence of ξ_d and u_1 holding Assumption 1 is not only guaranteed for most of the UAV models but also a family of solutions. Indeed, as variables in ξ are angle coordinates, they come into trigonometric expressions which naturally lead to multiple solutions, if any.

Once ξ_d and u_1 holding Assumption 1 are found, the next problem is to drive ξ towards ξ_d , i.e., to drive the tracking error $e_\xi(t) = \xi_d(t) - \xi(t)$ to 0 as $t \rightarrow \infty$. To this end, computed torque techniques come at the hand, i.e., from (19), we have

$$u_2 = \xi_d + K_{p\xi}e_\xi + K_{v\xi}\dot{e}_\xi, \quad (21)$$

where $K_{p\xi} \in \mathbb{R}^{3 \times 3}$ and $K_{v\xi} \in \mathbb{R}^{3 \times 3}$ are the matrices with proportional and derivative gains, respectively, to be defined (usually diagonal with positive entries).

The whole tracking error system, once Assumption 1 and computed torque control law (21) are employed, is given by

$$\frac{d}{dt} \begin{bmatrix} e_\eta \\ \dot{e}_\eta \\ e_\xi \\ \dot{e}_\xi \end{bmatrix} = \begin{bmatrix} 0 & I & 0 & 0 \\ -K_{p\eta} & -K_{v\eta} & 0 & 0 \\ 0 & 0 & 0 & I \\ 0 & 0 & -K_{p\xi} & -K_{v\xi} \end{bmatrix} \begin{bmatrix} e_\eta \\ \dot{e}_\eta \\ e_\xi \\ \dot{e}_\xi \end{bmatrix}. \quad (22)$$

The main result of this work can now be stated by defining the overall tracking error signal as $e = [e_\eta^T \ \dot{e}_\eta^T \ e_\xi^T \ \dot{e}_\xi^T]^T$.

Theorem 1. *The origin $e = 0$ of the tracking error system (22) is asymptotically stable if there exists matrices $X_1 \in \mathbb{R}^{6 \times 6}$, $X_2 \in \mathbb{R}^{6 \times 6}$, $X_1 = X_1^T$, $X_2 = X_2^T$, $M_{p\eta} \in \mathbb{R}^{3 \times 3}$, $M_{v\eta} \in \mathbb{R}^{3 \times 3}$, $M_{p\xi} \in \mathbb{R}^{3 \times 3}$, and $M_{v\xi} \in \mathbb{R}^{3 \times 3}$, such that the following LMIs hold:*

$$\begin{aligned} X_1 &> 0, \\ X_2 &> 0, \\ \begin{bmatrix} 0 & I \\ 0 & 0 \end{bmatrix} X_1 + \begin{bmatrix} 0 \\ I \end{bmatrix} [M_{p\eta} \ M_{v\eta}] &< 0, \\ \begin{bmatrix} 0 & I \\ 0 & 0 \end{bmatrix} X_2 + \begin{bmatrix} 0 \\ I \end{bmatrix} [M_{p\xi} \ M_{v\xi}] &< 0. \end{aligned} \quad (23)$$

In that case, the gains are given by

$$\begin{aligned} [-K_{p\eta} \ -K_{v\eta}] &= [M_{p\eta} \ M_{v\eta}] X_1^{-1}, \\ [-K_{p\xi} \ -K_{v\xi}] &= [M_{p\xi} \ M_{v\xi}] X_2^{-1}. \end{aligned} \quad (24)$$

Proof. The closed-loop tracking error system (22) can be rewritten as two independent ones, namely,

$$\begin{aligned} \frac{d}{dt} \begin{bmatrix} e_\eta \\ \dot{e}_\eta \end{bmatrix} &= \left(\begin{bmatrix} 0 & I \\ 0 & 0 \end{bmatrix} + \begin{bmatrix} 0 \\ I \end{bmatrix} [-K_{p\eta} \ -K_{v\eta}] \right) \begin{bmatrix} e_\eta \\ \dot{e}_\eta \end{bmatrix}, \\ \frac{d}{dt} \begin{bmatrix} e_\xi \\ \dot{e}_\xi \end{bmatrix} &= \left(\begin{bmatrix} 0 & I \\ 0 & 0 \end{bmatrix} + \begin{bmatrix} 0 \\ I \end{bmatrix} [-K_{p\xi} \ -K_{v\xi}] \right) \begin{bmatrix} e_\xi \\ \dot{e}_\xi \end{bmatrix}. \end{aligned} \quad (25)$$

Let us focus on the first one as the proof follows the same lines for both of them. Consider the quadratic Lyapunov function candidate $V = [e_\eta^T \ \dot{e}_\eta^T] P_1 [e_\eta^T \ \dot{e}_\eta^T]^T$, where $P_1 = X_1^{-1} > 0$; its time derivative is

$$\begin{aligned} \dot{V} &= \begin{bmatrix} e_\eta \\ \dot{e}_\eta \end{bmatrix}^T P_1 \begin{bmatrix} \dot{e}_\eta \\ e_\eta \end{bmatrix} + \begin{bmatrix} \dot{e}_\eta \\ e_\eta \end{bmatrix}^T P_1 \begin{bmatrix} e_\eta \\ \dot{e}_\eta \end{bmatrix} \\ &= \begin{bmatrix} e_\eta \\ \dot{e}_\eta \end{bmatrix}^T \left(P_1 \left(\begin{bmatrix} 0 & I \\ 0 & 0 \end{bmatrix} + \begin{bmatrix} 0 \\ I \end{bmatrix} [-K_{p\eta} \ -K_{v\eta}] \right) + (*) \right) \begin{bmatrix} e_\eta \\ \dot{e}_\eta \end{bmatrix}. \end{aligned} \quad (26)$$

Condition $\dot{V} < 0$ for $(e_\eta, \dot{e}_\eta) \neq (0, 0)$ is satisfied if

$$P_1 \left(\begin{bmatrix} 0 & I \\ 0 & 0 \end{bmatrix} + \begin{bmatrix} 0 \\ I \end{bmatrix} \begin{bmatrix} -K_{p\eta} & -K_{v\eta} \end{bmatrix} \right) + (*) < 0, \quad (27)$$

which pre and postmultiplying by $X_1 = P_1^{-1}$ is equivalent to the third LMI in (23), provided that $\begin{bmatrix} -K_{p\eta} & -K_{v\eta} \end{bmatrix} X_1 = \begin{bmatrix} M_{p\eta} & M_{v\eta} \end{bmatrix}$, thus proving that $V(t)$ is a valid Lyapunov function establishing asymptotic stability of $\begin{bmatrix} e_\eta^T & \dot{e}_\eta^T \end{bmatrix}^T = 0$.

The same analysis establishes asymptotic stability of $\begin{bmatrix} e_\xi^T & \dot{e}_\xi^T \end{bmatrix}^T = 0$, thus concluding the proof. \square

Remark 1. As pointed out before, for any UAV model belonging to the family of systems under consideration, there is always a variety of solutions leading to a linear tracking error system; in this sense, the technique mimics computed torque control [39]. Since some states are employed as fictitious control signals in order to drive another set of states to a desired reference, the technique mimics backstepping [38]. Nevertheless, the proposal does not belong to any of the former approaches.

Remark 2. Notice that, in contrast with computed torque techniques, the gains $K_{p\eta}$, $K_{v\eta}$, $K_{p\xi}$, and $K_{v\xi}$ are not asked to be diagonal, which provides greater flexibility to the controller design. Moreover, these gains are determined via LMIs, which are solved in polynomial time by commercially available software. The LMI formulation has additional advantages as performance specifications such as decay rate, input/output constraints, or \mathcal{H}_∞ disturbance attenuation can be straightforwardly added [36].

4. Simulation Results

In this section, two examples illustrating our proposal are presented: the first one concerns a quadrotor performing trajectory tracking; the second one is an 8-rotor UAV. In both cases, a member of a family of exact nonlinear cascade control laws for trajectory tracking is used.

Example 1. Consider the quadrotor system (12), reproduced for convenience with a split of the state vector corresponding to (17), where the Cartesian coordinates are governed by

$$\eta \equiv \begin{bmatrix} x \\ y \\ z \end{bmatrix} = \begin{bmatrix} \frac{(\sin \phi \sin \psi + \sin \theta \cos \phi \cos \psi)u}{m} \\ \frac{(\sin \theta \sin \psi \cos \phi - \sin \phi \cos \psi)u}{m} \\ \frac{(\cos \theta \cos \phi)u}{m} - g \end{bmatrix}, \quad (28)$$

and angular coordinates are driven by

$$\xi \equiv \begin{bmatrix} \psi \\ \dot{\theta} \\ \phi \end{bmatrix} = \begin{bmatrix} \tilde{\tau}_\psi \\ \tilde{\tau}_\theta \\ \tilde{\tau}_\phi \end{bmatrix}, \quad (29)$$

where $u_1 = u$ and $u_2 = [\tilde{\tau}_\psi \ \tilde{\tau}_\theta \ \tilde{\tau}_\phi]^T$ in the notation of (17).

Focusing on the dynamic equation (28) governing the position in Cartesian coordinates, it is clear that, with the exception of u , angular variables ψ , θ , and ϕ can be seen as virtual inputs; their ideal values being those necessary to drive the Cartesian coordinates as desired for trajectory purposes; let us name these ideal signals as ψ_d , θ_d , and ϕ_d , which results in (28) being rewritten as the steady-state dynamic equations:

$$\begin{aligned} x &= \frac{(\sin \phi_d \sin \psi_d + \sin \theta_d \cos \phi_d \cos \psi_d)u}{m}, \\ y &= \frac{(\sin \theta_d \sin \psi_d \cos \phi_d - \sin \phi_d \cos \psi_d)u}{m}, \\ z &= \frac{(\cos \theta_d \cos \phi_d)u}{m} - g, \end{aligned} \quad (30)$$

where it is supposed that the angles are already in their sought behaviour.

Since the control objective is that the system tracks a reference in Cartesian coordinates, the error signals are defined as $e_x = x_d - x$, $e_y = y_d - y$, and $e_z = z_d - z$, where x_d , y_d , and z_d are the desired trajectories in x , y , and z coordinates, respectively. Thus, taking into account the dynamic equations above, the error system (18) is given by

$$\begin{aligned} e_x &= x_d - x = x_d - \frac{\sin \phi_d \sin \psi_d + \sin \theta_d \cos \phi_d \cos \psi_d}{m} u, \\ e_y &= y_d - y = y_d - \frac{\sin \theta_d \sin \psi_d \cos \phi_d - \sin \phi_d \cos \psi_d}{m} u, \\ e_z &= z_d - z = z_d - \frac{\cos \phi_d \cos \theta_d}{m} u + g. \end{aligned} \quad (31)$$

Following the methodology, equation (20) in Assumption 1 is expressed as

$$\begin{aligned} & \begin{bmatrix} x_d - \frac{\sin \phi_d \sin \psi_d + \sin \theta_d \cos \phi_d \cos \psi_d}{m} u \\ y_d - \frac{\sin \theta_d \sin \psi_d \cos \phi_d - \sin \phi_d \cos \psi_d}{m} u \\ z_d - \frac{\cos \phi_d \cos \theta_d}{m} u + g \end{bmatrix} \\ &= -K_{p\eta} \begin{bmatrix} e_x \\ e_y \\ e_z \end{bmatrix} - K_{v\eta} \begin{bmatrix} \dot{e}_x \\ \dot{e}_y \\ \dot{e}_z \end{bmatrix}, \end{aligned} \quad (32)$$

where $K_{p\eta} \in \mathbb{R}^{3 \times 3}$ and $K_{v\eta} \in \mathbb{R}^{3 \times 3}$ are the constant gains to be found. If the above equations hold, the tracking $x \rightarrow x_d$, $y \rightarrow y_d$, and $z \rightarrow z_d$ will be performed; they are 3 equations with 4 variables, namely, u , ψ_d , θ_d , and ϕ_d . Due to their nonlinear trigonometric nature, there is an infinite number of solutions, each of them yielding a family of controllers that guarantee the tracking error goes to zero. In order to obtain a particular solution, we simplify the analysis considering that the gains $K_{p\eta}$ and $K_{v\eta}$ have a diagonal form, i.e.,

$$K_{p\eta} = \begin{bmatrix} K_{px} & 0 & 0 \\ 0 & K_{py} & 0 \\ 0 & 0 & K_{pz} \end{bmatrix}, \quad (33)$$

$$K_{v\eta} = \begin{bmatrix} K_{vx} & 0 & 0 \\ 0 & K_{vy} & 0 \\ 0 & 0 & K_{vz} \end{bmatrix}.$$

Thus, from the last equation in (32), it is clear that the choice

$$u = \frac{m}{\cos \phi_d \cos \theta_d} (z_d + g + K_{pz} e_z + K_{vz} \dot{e}_z), \quad (34)$$

will drive the error signal e_z to zero, i.e., $z \rightarrow z_d$. Substituting (34) in the first two equations in (32), we have

$$\frac{\tan \phi_d \sin \psi_d}{\cos \theta_d} + \tan \theta_d \cos \psi_d = \frac{x_d + K_{px} e_x + K_{vx} \dot{e}_x}{z_d + g + K_{pz} e_z + K_{vz} \dot{e}_z},$$

$$\sin \psi_d \tan \theta_d - \frac{\cos \psi_d \tan \phi_d}{\cos \theta_d} = \frac{y_d + K_{py} e_y + K_{vy} \dot{e}_y}{z_d + g + K_{pz} e_z + K_{vz} \dot{e}_z}. \quad (35)$$

There are many ways to find a set of solutions to the equations above. One choice is to solve for θ_d and ϕ_d , which will depend on ψ_d , the other variables in the expression being known. Nevertheless, regardless of the value of ψ_d , the equalities will be fulfilled; therefore, it is enough to drive ψ to $\psi_d = 0$. Now that the control signal u and the virtual inputs ψ_d , θ_d , and ϕ_d are known, time derivatives $\dot{\psi}$, $\dot{\theta}_d$, $\dot{\phi}_d$, $\dot{\psi}$, $\dot{\theta}_d$, and $\dot{\phi}_d$ can be calculated in order to use them in the computed torque control (21). The latter consists in designing $\tilde{\tau}$ such that the orientation angles go to their corresponding desired signals, that is, $\psi \rightarrow \psi_d$, $\theta \rightarrow \theta_d$, and $\phi \rightarrow \phi_d$ as $t \rightarrow \infty$. Thus, considering that gains $K_{p\xi}$ and $K_{v\xi}$ in (21) have the following structure,

$$K_{p\xi} = \begin{bmatrix} K_{p\psi} & 0 & 0 \\ 0 & K_{p\theta} & 0 \\ 0 & 0 & K_{p\phi} \end{bmatrix}, \quad (36)$$

$$K_{v\xi} = \begin{bmatrix} K_{v\psi} & 0 & 0 \\ 0 & K_{v\theta} & 0 \\ 0 & 0 & K_{v\phi} \end{bmatrix},$$

the control law (21) is given by

$$\begin{aligned} \tilde{\tau}_\psi &= \psi_d + K_{p\psi} e_\psi + K_{v\psi} \dot{e}_\psi, \\ \tilde{\tau}_\theta &= \theta_d + K_{p\theta} e_\theta + K_{v\theta} \dot{e}_\theta, \\ \tilde{\tau}_\phi &= \phi_d + K_{p\phi} e_\phi + K_{v\phi} \dot{e}_\phi, \end{aligned} \quad (37)$$

where $K_{p\psi}$, $K_{p\theta}$, $K_{p\phi}$, $K_{v\psi}$, $K_{v\theta}$, and $K_{v\phi}$ are the constant gains to be found.

The LMIs in Theorem 1 can now be programmed; they yield the following feasible solution:

$$X_1 = \begin{bmatrix} 0.2639 & 0 & 0 & -0.4342 & 0 & 0 \\ 0 & 0.2639 & 0 & 0 & -0.4342 & 0 \\ 0 & 0 & 0.4827 & 0 & 0 & -0.4972 \\ -0.4342 & 0 & 0 & 0.9186 & 0 & 0 \\ 0 & -0.4342 & 0 & 0 & 0.9186 & 0 \\ 0 & 0 & -0.4972 & 0 & 0 & 0.5507 \end{bmatrix},$$

$$X_2 = \begin{bmatrix} 0.2302 & 0 & 0 & -0.438 & 0 & 0 \\ 0 & 0.2302 & 0 & 0 & -0.438 & 0 \\ 0 & 0 & 0.2302 & 0 & 0 & -0.438 \\ -0.438 & 0 & 0 & 0.8885 & 0 & 0 \\ 0 & -0.438 & 0 & 0 & 0.8885 & 0 \\ 0 & 0 & -0.438 & 0 & 0 & 0.8885 \end{bmatrix},$$

$$K_{p\eta} = \begin{bmatrix} 20 & 0 & 0 \\ 0 & 20 & 0 \\ 0 & 0 & 30 \end{bmatrix},$$

$$K_{v\eta} = \begin{bmatrix} 10 & 0 & 0 \\ 0 & 10 & 0 \\ 0 & 0 & 28 \end{bmatrix},$$

$$K_{p\xi} = \begin{bmatrix} 80 & 0 & 0 \\ 0 & 80 & 0 \\ 0 & 0 & 80 \end{bmatrix},$$

$$K_{v\xi} = \begin{bmatrix} 40 & 0 & 0 \\ 0 & 40 & 0 \\ 0 & 0 & 40 \end{bmatrix}. \quad (38)$$

Figure 2 shows the simulation results of the position and control signals where the quadrotor follows the desired trajectory $x_d = 1 + \cos(t)$, $y_d = -\sin(t)$, and $z_d = 1 + 0.2 \sin(2t)$. The initial conditions for simulation are $x(0) = 0$, $y(0) = -1$, $z(0) = 2$, $\dot{x}(0) = \dot{y}(0) = \dot{z}(0) = 0$, and $\psi(0) = \theta(0) = \phi(0) = \dot{\psi}(0) = \dot{\theta}(0) = \dot{\phi}(0) = 0$. High-frequency signals are customary during the transient of UAV control due to the very fast dynamics of these plants; this is the case of the control signals on the right.

Example 2. Consider the 8-rotor aircraft system whose mathematical model is given by

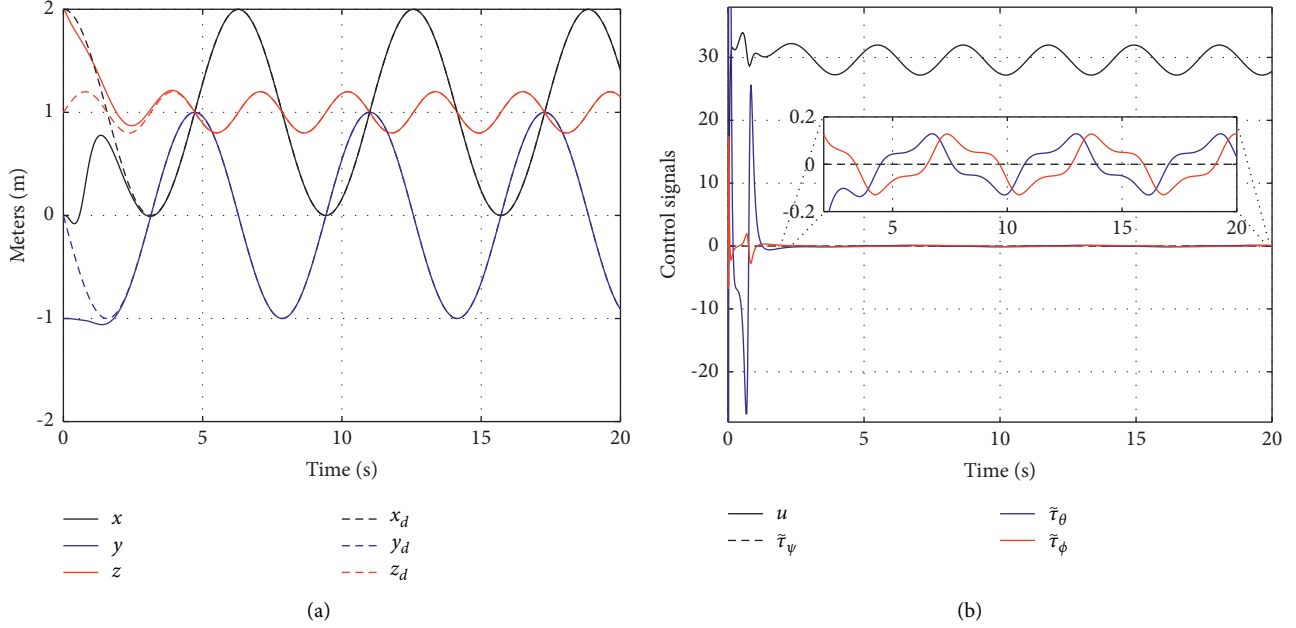


FIGURE 2: Quadrotor simulation results for trajectory tracking: position (a) and control (b).

$$\begin{aligned}
 mx &= u_x \cos \theta \cos \psi - u_y (\cos \phi \sin \psi - \cos \psi \sin \theta \sin \phi) + u_z (\sin \phi \sin \psi + \cos \phi \cos \psi \sin \theta), \\
 my &= u_x \cos \theta \sin \psi + u_y (\cos \phi \cos \psi + \sin \psi \sin \theta \sin \phi) - u_z (\sin \phi \cos \psi - \cos \phi \sin \psi \sin \theta), \\
 mz &= -u_x \sin \theta + u_y \cos \theta \sin \phi + u_z \cos \theta \cos \phi - mg, \\
 \psi &= \tilde{\tau}_\psi, \\
 \ddot{\theta} &= \tilde{\tau}_\theta, \\
 \phi &= \tilde{\tau}_\phi,
 \end{aligned} \tag{39}$$

where (x, y, z) represent the position of the aircraft in Cartesian coordinates, (ψ, θ, ϕ) are the orientation angles, m is the mass of the aircraft, and g is the gravitational constant. In contrast with the quadrotor, this model has six control inputs $u_x, u_y, u_z, \tilde{\tau}_\psi, \tilde{\tau}_\theta,$ and $\tilde{\tau}_\phi$ (see [9] for modelling details).

Following the methodology shown in Section 3, the error signals of interest are defined as $e_x = x_d - x, e_y = y_d - y,$ and $e_z = z_d - z.$ Dynamic equations of the error system (18)

can be straightforwardly written (omitted for brevity). In contrast with the previous example where variables $\phi, \theta,$ and ψ were considered as auxiliary/virtual control inputs, in the case of the 8-rotor aircraft, there are two more authentic control inputs; therefore, it is not necessary to take other signals as virtual control ones. In this case, considering the gains structure (33), Assumption 1 is given by the following equations, and it is fulfilled solving for $u_1 = [u_x \ u_y \ u_z]^T$ regardless of $\xi = [\psi \ \theta \ \phi]^T,$

$$\begin{aligned}
 e_x &= x_d - \frac{u_x}{m} \cos \theta \cos \psi + \frac{u_y}{m} (\cos \phi \sin \psi - \cos \psi \sin \theta \sin \phi) - \frac{u_z}{m} (\sin \phi \sin \psi + \cos \phi \cos \psi \sin \theta) \\
 &= -K_{px} e_x - K_{vx} \dot{e}_x, \\
 e_y &= y_d - \frac{u_x}{m} \cos \theta \sin \psi - \frac{u_y}{m} (\cos \phi \cos \psi + \sin \psi \sin \theta \sin \phi) + \frac{u_z}{m} (\sin \phi \cos \psi - \cos \phi \sin \psi \sin \theta) \\
 &= -K_{py} e_y - K_{vy} \dot{e}_y, \\
 e_z &= z_d + \frac{u_x}{m} \sin \theta - \frac{u_y}{m} \cos \theta \sin \phi - \frac{u_z}{m} \cos \theta \cos \phi + g = -K_{pz} e_z - K_{vz} \dot{e}_z.
 \end{aligned} \tag{40}$$

If equalities above are satisfied, the tracking errors are guaranteed to go to zero as time tends to infinity; thus, the

control signals u_x , u_y , and u_z can be solved. By way of illustration, the shortest of them is provided, namely, $u_y = u_{ym}/u_{yd}$, where

$$\begin{aligned} u_{ym} = & -(2(y_d \cos \phi \cos \psi - x_d \cos \phi \sin \psi + z_d \cos \theta \sin \phi + x_d \cos \psi \sin \phi \sin \theta \\ & + y_d \sin \phi \sin \psi \sin \theta + K_{vy} \dot{e}_y \cos \phi \cos \psi + K_{py} e_y \cos \phi \cos \psi - K_{vx} \dot{e}_x \cos \phi \sin \psi \\ & - K_{px} e_x \cos \phi \sin \psi + K_{vz} \dot{e}_z \cos \theta \sin \phi + K_{pz} e_z \cos \theta \sin \phi + gm \cos \theta \sin \phi \\ & + K_{vx} \dot{e}_x \cos \psi \sin \phi \sin \theta + K_{px} e_x \cos \psi \sin \phi \sin \theta + K_{vy} \dot{e}_y \sin \phi \sin \psi \sin \theta \\ & + K_{py} e_y \sin \phi \sin \psi \sin \theta)), \\ u_{yd} = & 4\cos^2 \phi \cos^2 \psi - 4\cos^2 \phi - 4\cos^2 \psi - 2\cos^2 \theta - \sin(2\theta) + 2\cos^2 \phi \cos^2 \theta + 4\cos^2 \psi \cos^2 \theta \\ & + 2\cos^2 \phi \cos \theta \sin \theta - 4\cos^2 \phi \cos^2 \psi \cos^2 \theta + 4 \cos \phi \cos \psi \sin \phi \sin \psi \sin \theta + 2. \end{aligned} \quad (41)$$

Once the control signals u_x , u_y , and u_z have been found, the remaining ones $\tilde{\tau}_\psi$, $\tilde{\tau}_\theta$, and $\tilde{\tau}_\phi$ are proposed with a simple PD form, such that $\psi \rightarrow 0$, $\theta \rightarrow 0$, and $\phi \rightarrow 0$ as $t \rightarrow \infty$. Thus,

$$\begin{aligned} \tilde{\tau}_\psi &= -K_{p\psi} \psi - K_{v\psi} \dot{\psi}, \\ \tilde{\tau}_\theta &= -K_{p\theta} \theta - K_{v\theta} \dot{\theta}, \\ \tilde{\tau}_\phi &= -K_{p\phi} \phi - K_{v\phi} \dot{\phi}. \end{aligned} \quad (42)$$

Figure 3 shows the simulation results for initial conditions $x(0) = 0$, $y(0) = -1$, $z(0) = 2$, $\dot{x}(0) = \dot{y}(0) = \dot{z}(0) = 0$, and $\psi(0) = \theta(0) = \phi(0) = \dot{\psi}(0) = \dot{\theta}(0) = \dot{\phi}(0) = 0$. It can be seen in 3(a) that the position of the aircraft follows the desired trajectory $x_d = 1 + \cos(t)$, $y_d = -\sin(t)$, and $z_d = 1 + 0.2 \sin(t)$. The gains used are $K_{px} = K_{py} = K_{pz} = 20$, $K_{vx} = K_{vy} = K_{vz} = 10$, $K_{p\psi} = K_{p\theta} = K_{p\phi} = 80$, and $K_{v\psi} = K_{v\theta} = K_{v\phi} = 40$. Control signals are shown 3(b). Since in this case, it was not necessary to take signals as virtual control inputs, the initial conditions for the angles are

zero, and the control signals $\tilde{\tau}_\psi$, $\tilde{\tau}_\theta$, and $\tilde{\tau}_\phi$ are zero during simulation.

The previous solution does not exploit the cascade structure of the system; in this sense, it is a 0-level cascade one. A 1-level one is, nevertheless, possible; such control law does not only serve artificial purposes but also can help standing against actuator fails. To illustrate this alternative, the design can take up from the error equations in (40); any variable in these expressions can be considered as a control signal, which results in a cascade structure and in turn represents a family of solutions. Indeed, considering the control input u_z as

$$u_z = \frac{mg + m\theta + u_x \sin \theta - u_y \sin \phi \sin \theta}{\cos \phi \cos \theta}, \quad (43)$$

the dynamics of the z position can be rewritten as $z = \theta$. Thus, θ can be seen as a fictitious control input, thus resulting in a cascade control. Renaming θ as θ_d and substituting (43), Assumption 1 yields

$$\begin{aligned} x_d - \frac{u_x}{m} \cos \theta_d \cos \psi + \frac{u_y}{m} (\cos \phi \sin \psi - \cos \psi \sin \theta_d \sin \phi) \\ - \frac{(gm + m\theta_d + u_x \sin \theta_d - u_y \sin \phi \sin \theta_d)(\sin \phi \sin \psi + \cos \phi \cos \psi \sin \theta_d)}{m \cos \phi \cos \theta_d} &= -K_{px} e_x - K_{vx} \dot{e}_x, \\ y_d - \frac{u_x}{m} \cos \theta_d \sin \psi - \frac{u_y}{m} (\cos \phi \cos \psi + \sin \psi \sin \theta_d \sin \phi) \\ + \frac{(gm + m\theta_d + u_x \sin \theta_d - u_y \sin \phi \sin \theta_d)(\sin \phi \cos \psi - \cos \phi \sin \psi \sin \theta_d)}{m \cos \phi \cos \theta_d} &= -K_{py} e_y - K_{vy} \dot{e}_y, \\ z_d - \theta_d &= -K_{pz} e_z - K_{vz} \dot{e}_z, \end{aligned} \quad (44)$$

which can be solved for u_x , u_y , and θ_d , such that Assumption 1 holds.

Once the control signals u_x , u_y , u_z , and the virtual input θ_d are determined, the time derivatives $\dot{\theta}_d$ and $\ddot{\theta}_d$ can be calculated to be used in the computed torque control (21),

which consists in designing $\tilde{\tau}$, such that the orientation angles go to their corresponding desired signals, i.e., $\theta \rightarrow \theta_d$ as $t \rightarrow \infty$. Thus, considering that the gains $K_{p\xi}$ and $K_{v\xi}$ have the structure (36), the control law (21) is given by

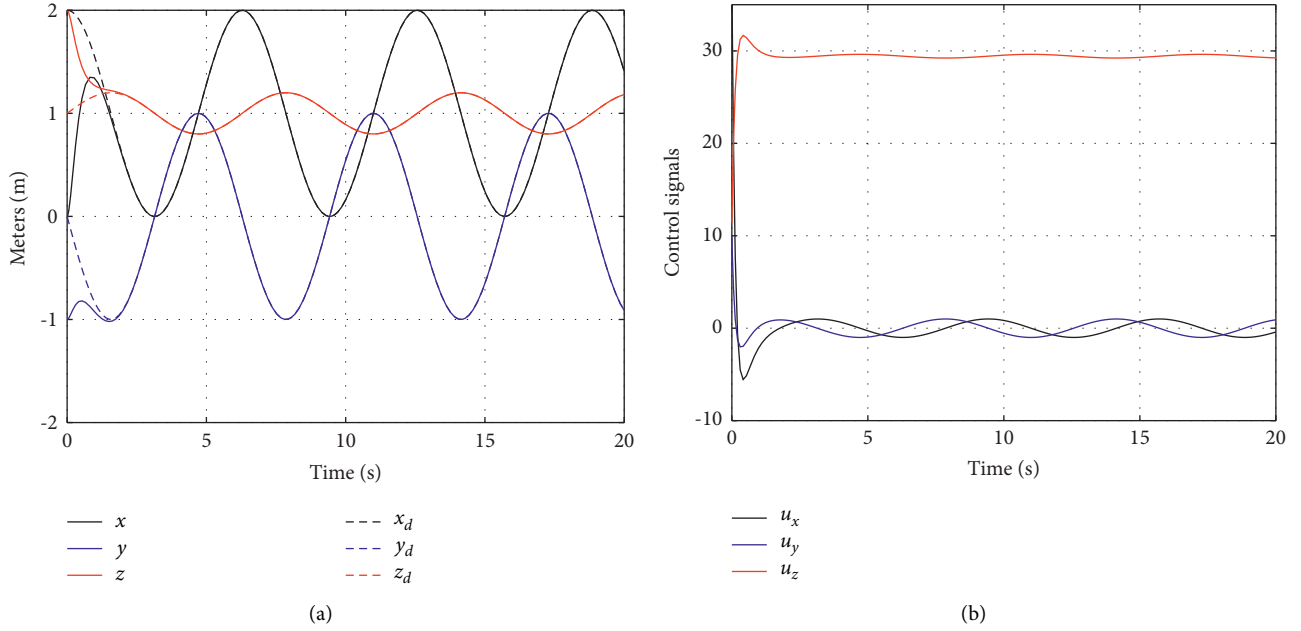


FIGURE 3: Octarotor simulation results for trajectory tracking: position (a) and control (b).

$$\begin{aligned}
 \bar{\tau}_\psi &= \psi_d + K_{p\psi}e_\psi + K_{v\psi}\dot{e}_\psi, \\
 \bar{\tau}_\theta &= \ddot{\theta}_d + K_{p\theta}e_\theta + K_{v\theta}\dot{e}_\theta, \\
 \bar{\tau}_\phi &= \phi_d + K_{p\phi}e_\phi + K_{v\phi}\dot{e}_\phi,
 \end{aligned} \tag{45}$$

where $K_{p\psi}$, $K_{p\theta}$, $K_{p\phi}$, $K_{v\psi}$, $K_{v\theta}$, and $K_{v\phi}$ are the constant gains to be found.

LMIs in Theorem 1 have been found feasible with the following solution:

$$\begin{aligned}
 X_1 &= \begin{bmatrix} 0.2126 & 0 & 0 & -0.3695 & 0 & 0 \\ 0 & 0.3192 & 0 & 0 & -0.5168 & 0 \\ 0 & 0 & 0.3192 & 0 & 0 & -0.5168 \\ -0.3695 & 0 & 0 & 1.2294 & 0 & 0 \\ 0 & -0.5168 & 0 & 0 & 1.0959 & 0 \\ 0 & 0 & -0.5168 & 0 & 0 & 1.0959 \end{bmatrix}, \\
 X_2 &= \begin{bmatrix} 0.2609 & 0 & 0 & -0.4959 & 0 & 0 \\ 0 & 0.2609 & 0 & 0 & -0.4959 & 0 \\ 0 & 0 & 0.2609 & 0 & 0 & -0.4959 \\ -0.4959 & 0 & 0 & 1.0065 & 0 & 0 \\ 0 & -0.4959 & 0 & 0 & 1.0065 & 0 \\ 0 & 0 & -0.4959 & 0 & 0 & 1.0065 \end{bmatrix}, \\
 K_{p\eta} &= \begin{bmatrix} 15 & 0 & 0 \\ 0 & 20 & 0 \\ 0 & 0 & 20 \end{bmatrix}, \\
 K_{v\eta} &= \begin{bmatrix} 5 & 0 & 0 \\ 0 & 10 & 0 \\ 0 & 0 & 10 \end{bmatrix}, \\
 K_{p\xi} &= \begin{bmatrix} 80 & 0 & 0 \\ 0 & 80 & 0 \\ 0 & 0 & 80 \end{bmatrix}, \\
 K_{v\xi} &= \begin{bmatrix} 40 & 0 & 0 \\ 0 & 40 & 0 \\ 0 & 0 & 40 \end{bmatrix}.
 \end{aligned} \tag{46}$$

Figure 4(a) shows the simulation results of the position where the aircraft follows the desired trajectory $x_d = 1 + \cos(t)$, $y_d = 0.5 - \sin(t)$, and $z_d = 1 + 0.2 \sin(t) + 0.2 \cos(t)$

(2t). Initial conditions are $x(0) = 0$, $y(0) = -1$, $z(0) = 2$, $\dot{x}(0) = \dot{y}(0) = \dot{z}(0) = 0$, and $\psi(0) = \theta(0) = \phi(0) = \dot{\psi}(0) = \dot{\theta}(0) = \dot{\phi}(0) = 0$. Figure 4(b) shows the control signal.

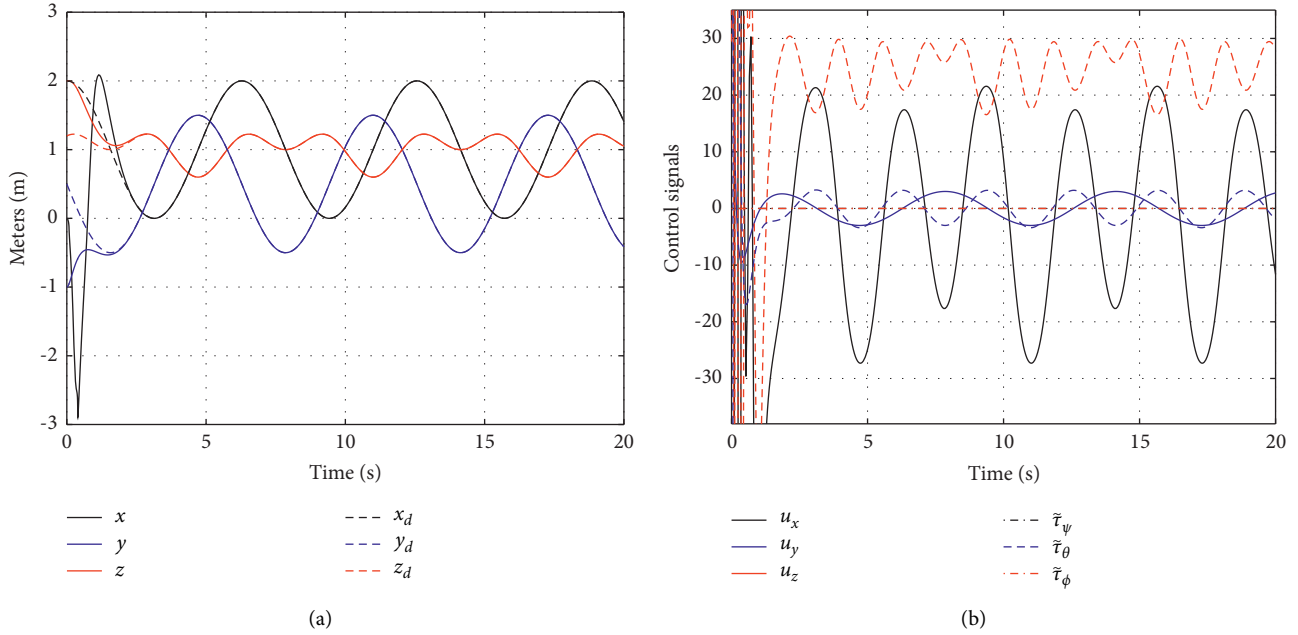


FIGURE 4: Octarotor simulation results for trajectory tracking: position (a) and control (b).

5. Real-Time Results

To corroborate the effectiveness of the proposed results in the previous section, its implementation on an experimental platform is presented; such implementation has been made in the National Laboratory of Autonomous Vehicles and Exoskeletons from the Autonomous University of Hidalgo State. The system used for the experiments is from the DJI Matrice 100 quadrotor (Figure 5). Some details about the performance of this platform are given in Table 1, while the specifications of the structure are given in Table 2 [41].

The mathematical model of the experimental platform above is (10). To implement the controller (11), (34), and (37), first a simulation was conducted using the DJI flight simulator provided by the manufacturer, later to program on the experimental platform Android Studio and DJI Mobile SDK (software development kit).

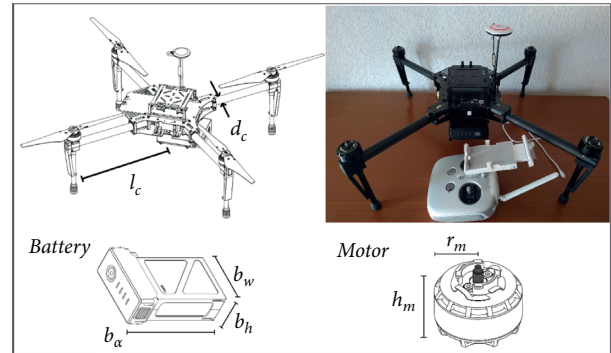


FIGURE 5: DJI Matrice 100 quadrotor.

Using the data given in the previous tables, the values of the Coriolis C and inertia J matrices are

$$C(\xi, \dot{\xi}) = \begin{bmatrix} c_{11} & c_{12} & c_{13} \\ c_{21} & c_{22} & c_{23} \\ c_{31} & c_{32} & c_{33} \end{bmatrix}, \quad (47)$$

$$J = \begin{bmatrix} I_{xx} & 0 & -I_{xx} \sin(\theta) \\ 0 & I_{yy} \cos^2(\phi) + I_{zz} \sin^2(\phi) & Mn_1 \\ -I_{xx} \sin(\theta) & Mn_2 & Mn_3 \end{bmatrix},$$

where $I_{xx} = 0.023442$, $I_{yy} = 0.025871$, and $I_{zz} = 0.0264413$, $c_{11} = 0$,

TABLE 1: Performance of experimental platform.

Hovering accuracy (<i>P</i> -mode with GPS)	Vertical: 0.5 m, horizontal: 2.5 m
Max. angular velocity	Pitch: 300°/s, yaw: 150°/s
Max. tilt angle	35°
Max. speed of ascent	5 m/s
Max. speed of descent	4 m/s
Max. wind resistance	10 m/s
Max. speed	22 m/s (ATTI mode, no payload, no wind) 17 m/s (GPS mode, no payload, no wind)
Hovering time (with TB47D battery)	No payload: 22 min; 500 g Payload: 17 min; 1 kg payload: 13 min

TABLE 2: Structure specifications of experimental platform.

Length of the frame arm (<i>l</i>)	0.65 m
Distance to center of gravity (<i>l_c</i>)	<i>l</i> /2
Mass of the frame arm (<i>m_{bc}</i>)	0.05 kg
Radius of the frame arm (<i>r_{bc} = d_c/2</i>)	0.01 m
Mass of the motor (<i>m_m</i>)	0.106 kg
Radius of the motor (<i>r_m</i>)	0.025 m
Height of the motor (<i>h_m</i>)	0.03 m
Mass of the battery (<i>m_b</i>)	0.6 kg
Width of the battery (<i>b_w</i>)	0.08 m
Height of the battery (<i>b_h</i>)	0.04 m
Length of the battery (<i>b_a</i>)	0.135 m
Net weight (<i>m</i>)	2.335 kg

$$\begin{aligned}
c_{12} &= -I_{xx}\dot{\psi}\cos(\theta) + I_{yy}\left(\dot{\theta}\sin(\phi)\cos(\phi) + \dot{\psi}\cos(\theta)\sin^2(\phi) - \dot{\psi}\cos(\theta)\cos^2(\phi)\right) \\
&\quad - I_{zz}\left(\dot{\psi}\cos(\theta)\sin^2(\phi) - \dot{\psi}\cos(\theta)\cos^2(\phi) + \dot{\theta}\sin\phi\cos\phi\right), \\
c_{13} &= I_{yy}\dot{\psi}\cos^2(\theta)\sin(\phi)\cos(\phi) - I_{zz}\dot{\psi}\cos^2(\theta)\sin(\phi)\cos(\phi), \\
c_{21} &= I_{xx}\dot{\psi}\cos(\theta) + I_{yy}\left(-\dot{\theta}\sin(\phi)\cos(\phi) + \dot{\psi}\cos(\theta)\cos^2(\phi) - \dot{\psi}\cos(\theta)\sin^2(\phi)\right) \\
&\quad + I_{zz}\left(\dot{\psi}\cos(\theta)\sin^2(\phi) - \dot{\psi}\cos(\theta)\cos^2(\phi) + \dot{\theta}\sin(\phi)\cos(\phi)\right), \\
c_{22} &= -I_{yy}\dot{\phi}\sin(\phi)\cos(\phi) + I_{zz}\dot{\phi}\sin(\phi)\cos(\phi), \\
c_{23} &= -I_{xx}\dot{\psi}\sin(\theta)\cos(\theta) + I_{yy}\dot{\psi}\sin(\theta)\cos(\theta)\sin^2(\phi) + I_{zz}\dot{\psi}\sin(\theta)\cos(\theta)\cos^2(\phi), \\
c_{31} &= -I_{xx}\dot{\theta}\cos(\theta) + I_{yy}\dot{\psi}\cos^2(\theta)\sin(\phi)\cos(\phi) - I_{zz}\dot{\psi}\cos^2(\theta)\sin(\phi)\cos(\phi), \\
c_{32} &= I_{xx}\dot{\phi}\sin(\theta)\cos(\theta) - I_{yy}\left(\dot{\theta}\sin(\theta)\sin(\phi)\cos(\phi) + \dot{\phi}\cos(\theta)\sin^2(\phi) - \dot{\phi}\cos(\theta)\cos^2(\phi)\right) \\
&\quad + \dot{\psi}\sin(\theta)\cos(\theta)\sin^2(\phi) + I_{zz}\left(\dot{\phi}\cos(\theta)\sin^2(\phi) - \dot{\phi}\cos(\theta)\cos^2(\phi)\right) \\
&\quad - \dot{\psi}\sin(\theta)\cos(\theta)\cos^2(\phi) + \dot{\theta}\sin(\theta)\sin(\phi)\cos(\phi), \\
c_{33} &= I_{xx}\dot{\theta}\sin(\theta)\cos(\theta) + I_{yy}\left(-\dot{\theta}\sin(\theta)\cos(\theta)\sin^2(\phi) + \dot{\phi}\cos^2(\theta)\sin(\phi)\cos(\phi)\right) \\
&\quad - I_{zz}\left(\dot{\theta}\sin(\theta)\cos(\theta)\cos^2(\phi) + \dot{\phi}\cos^2(\theta)\sin(\phi)\cos(\phi)\right), \\
Mn_1 &= \cos(\theta)\cos(\phi)\sin(\phi)(I_{yy} - I_{zz}), \\
Mn_2 &= \cos(\theta)\cos(\phi)\sin(\phi)(I_{yy} - I_{zz}), \\
Mn_3 &= I_{xx}\sin^2(\theta) + I_{yy}\cos^2(\theta)\sin^2(\phi) + I_{zz}\cos^2(\theta)\cos^2(\phi).
\end{aligned} \tag{48}$$

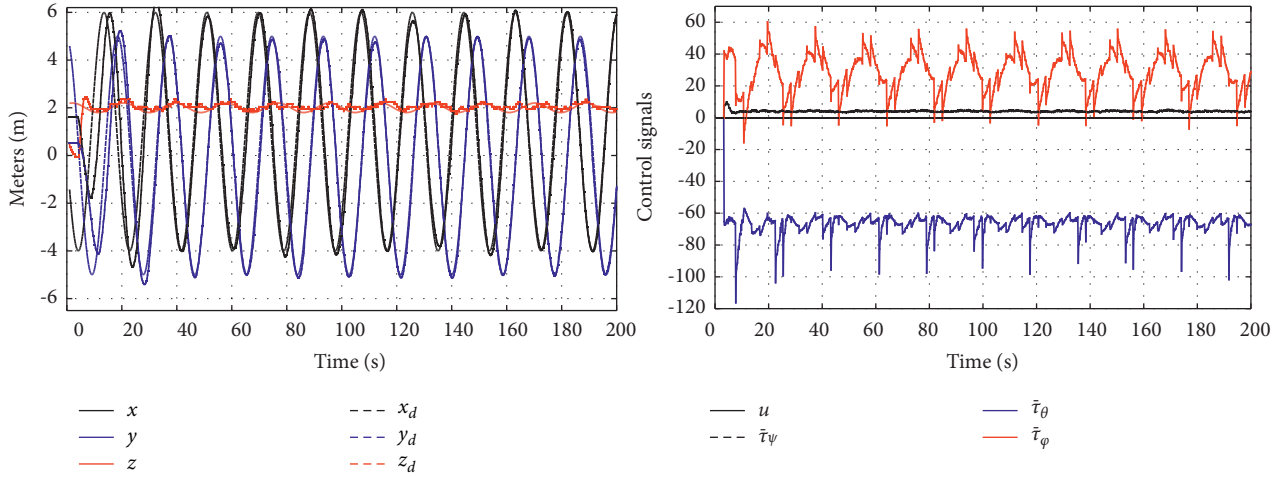


FIGURE 6: Quadrotor simulation results for trajectory tracking (2D).

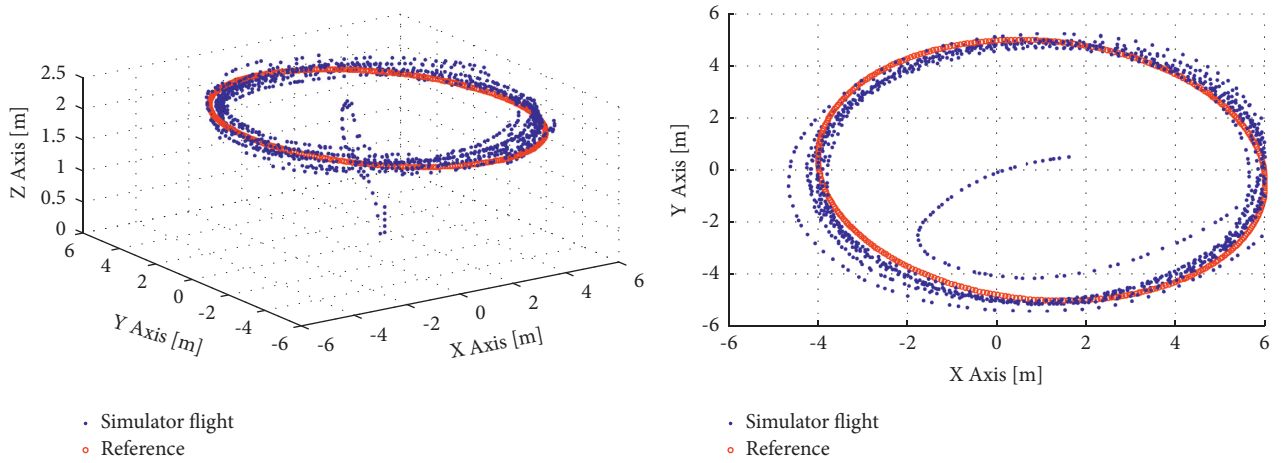


FIGURE 7: Quadrotor simulation results for trajectory tracking (3D).

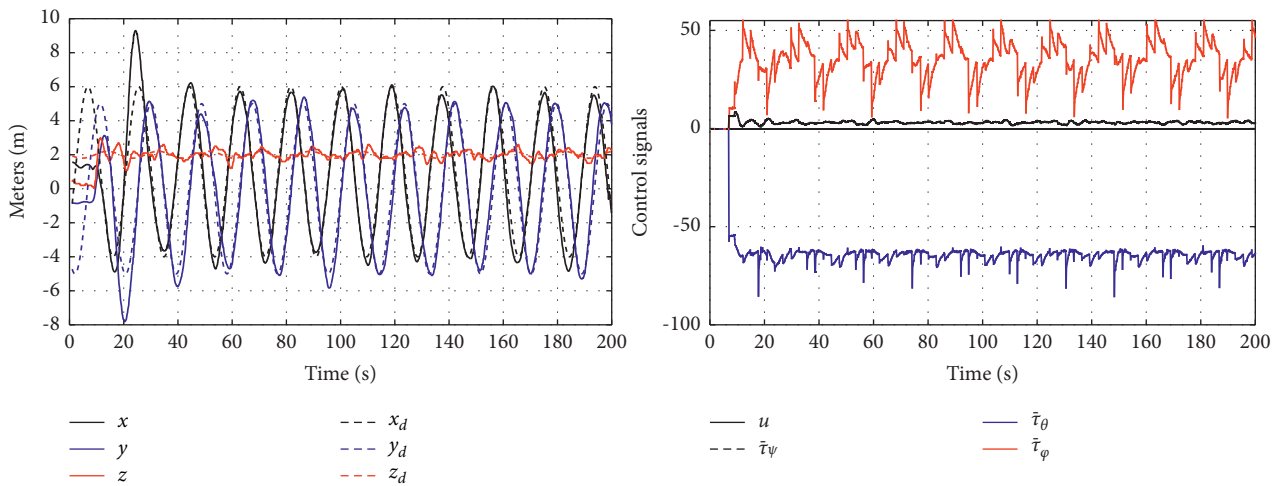


FIGURE 8: Quadrotor real-time results for trajectory tracking (2D).

Here, the desired trajectory of the quadrotor is $x_d = 1 + 5 \cos(t)$, $y_d = 5 \sin(t)$, and $z_d = 2 + 0.2 \sin(t)$. The initial conditions are $x(0) = y(0) = 0$, $z(0) = 1$,

$\dot{x}(0) = \dot{y}(0) = \dot{z}(0) = 0$, and $\psi(0) = \theta(0) = \phi(0) = \dot{\psi}(0) = \dot{\theta}(0) = \dot{\phi}(0) = 0$. For the input signal (24), $K_{px} = K_{py} = 50$, $K_{pz} = 60$, and $K_{vx} = K_{vy} = 10.5$ and $K_{vy} = 28$ are proposed.

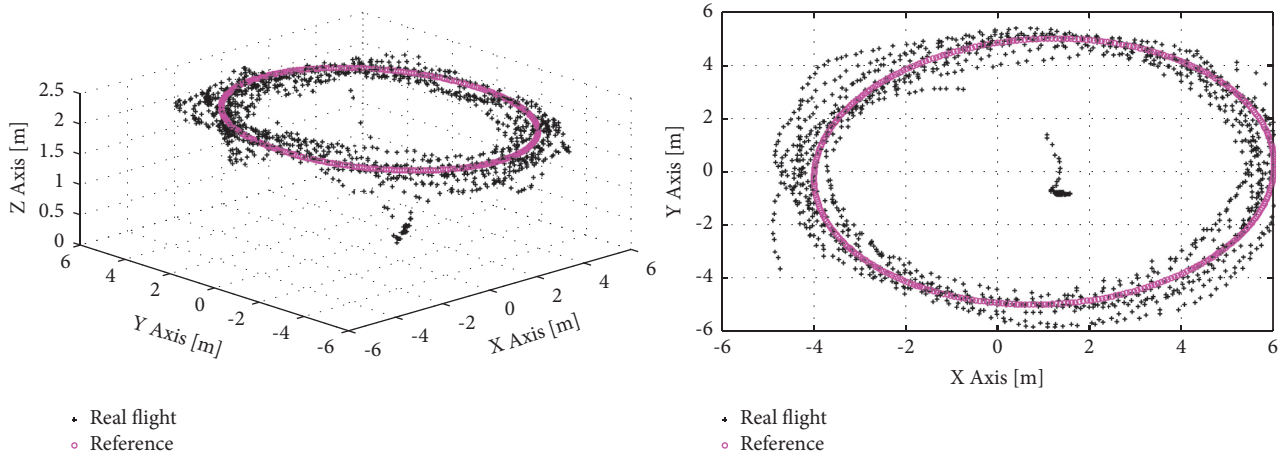


FIGURE 9: Quadrotor real-time results for trajectory tracking (3D).

While, for the equation (26), the gains used are $K_{p\theta} = K_{p\phi} = K_{p\psi} = 80$ and $K_{v\theta} = K_{v\phi} = K_{v\psi} = 40$.

Figures 6 and 7 show the performance of the DJI Matrice 100 quadrotor using the flight simulator provided by the manufacturer. The video with the simulation results can be seen at the following link: <https://youtu.be/Igoobvl61AE>.

Figures 8 and 9 show the performance of the DJI Matrice 100 quadrotor in real-time. The video where these results are shown can be consulted in the following link: <https://youtu.be/oGN5N7M3UZw>.

6. Conclusions

A family of exact nonlinear cascade control laws for trajectory tracking of unmanned aerial vehicles has been presented. It has been shown that the control scheme can be applied to UAVs because it takes advantage of their underactuated characteristics, which produce a cascade model suitable for Lyapunov-based design. The proposal has been proven to produce an infinite number of solutions which guarantee that the position in Cartesian coordinates of the aircraft follows a desired trajectory. The methodology has been illustrated via numerical simulations in 4- and 8-rotor systems. Real-time results have been provided on the quadrotor, which confirm the applicability of the presented approach. Future work is on course for including robustness and more general classes of underactuated systems.

Data Availability

No data were used to support this study.

Conflicts of Interest

The authors declare that they have no conflicts of interest.

Acknowledgments

This research has been supported by the CONACYT scholarship (731421), the Laboratory LANAVEX from the Universidad Politécnica de Pachuca, and the project ITSON-PROFAPI 2021-0027.

References

- [1] D. Orfanus, E. P. de Freitas, and F. Eliassen, "Self-organization as a supporting paradigm for military uav relay networks," *IEEE Communications Letters*, vol. 20, no. 4, pp. 804–807, 2016.
- [2] F. Nex and F. Remondino, "Uav for 3d mapping applications: a review," *Applied geomatics*, vol. 6, no. 1, pp. 1–15, 2014.
- [3] C. Qian, H. Yang, T. Ren, Z. Li, and F. Teng, "Real-time aerial photography and global positioning system for a quadrotor design," *Journal of Jilin University (Information Science Edition)*, vol. 4, 2015.
- [4] I. Sa and P. Corke, "Vertical infrastructure inspection using a quadcopter and shared autonomy control," in *Field and Service Robotics*, pp. 219–232, Springer, New York, NY, USA, 2012.
- [5] P. E. Pounds, D. R. Bersak, and A. M. Dollar, "Grasping from the air: hovering capture and load stability," in *Proceedings of the 2011 IEEE International Conference on Robotics and Automation*, pp. 2491–2498, IEEE, Shanghai, China, May 2011.
- [6] J. J. Potter, C. J. Adams, and W. Singhose, "A planar experimental remote-controlled helicopter with a suspended load," *IEEE/ASME transactions on mechatronics*, vol. 20, no. 5, pp. 2496–2503, 2015.
- [7] M. Arjomandi, S. Agostino, M. Mammone, M. Nelson, and T. Zhou, *Classification of Unmanned Aerial Vehicles. Report for Mechanical Engineering Class*, University of Adelaide, Adelaide, Australia, 2006.
- [8] H. Romero-Trejo, *Modélisation et asservissement visuel d'un mini hélicoptère*, Ph.D. thesis, University of Technology of Compiègne, Compiègne, France, 2008.
- [9] S. Salazar, H. Romero, R. Lozano, and P. Castillo, "Modeling and real-time stabilization of an aircraft having eight rotors," in *Unmanned Aircraft Systems*, pp. 455–470, Springer, New York, NY, USA, 2008.
- [10] B. Erginer and E. Altug, "Modeling and pd control of a quadrotor VTOL vehicle," in *Proceedings of the 2007 IEEE Intelligent Vehicles Symposium*, pp. 894–899, IEEE, Istanbul, Turkey, June 2007.
- [11] A. Tayebi and S. McGilvray, "Attitude stabilization of a vtol quadrotor aircraft," *IEEE Transactions on Control Systems Technology*, vol. 14, no. 3, pp. 562–571, 2006.

- [12] K. F. Maya-Gress, R. Villafuerte-Segura, H. Romero-Trejo, and M. Á. Bernal-Reza, "Puesta en operación y modelado de un cuatrorotor Matrice 100," *de DJI. Pádi Boletín Científico de Ciencias Básicas e Ingenierías del ICBI*, vol. 9, no. 17, pp. 67–75, 2021.
- [13] C. Coza and C. J. Macnab, "A new robust adaptive-fuzzy control method applied to quadrotor helicopter stabilization," in *Proceedings of the NAFIPS 2006-2006 Annual Meeting of the North American Fuzzy Information Processing Society*, pp. 454–458, IEEE, Montreal, Canada, June 2006.
- [14] B. Erginer and E. Altuğ, "Design and implementation of a hybrid fuzzy logic controller for a quadrotor VTOL vehicle," *International Journal of Control, Automation and Systems*, vol. 10, no. 1, pp. 61–70, 2012.
- [15] M. R. Mehranpour, A. M. Shahri, O. Emamgholi, and M. Farrokhi, "A new fuzzy adaptive control for a quadrotor flying robot," in *Proceedings of the 2013 13th Iranian Conference on Fuzzy Systems (IFSC)*, pp. 1–5, IEEE, Qazvin, Iran, August 2013.
- [16] H. Gao, C. Liu, D. Guo, and J. Liu, "Fuzzy adaptive pd control for quadrotor helicopter," in *Proceedings of the 2015 IEEE International Conference on Cyber Technology in Automation, Control, and Intelligent Systems (CYBER)*, pp. 281–286, IEEE, Shenyang, China, June 2015.
- [17] G. Dong, L. Cao, D. Yao, H. Li, and R. Lu, "Adaptive attitude control for multi-muav systems with output dead-zone and actuator fault," *IEEE/CAA Journal of Automatica Sinica*, vol. 8, pp. 1567–1575, 2020.
- [18] A. Almeshal and M. Alenezi, "A vision-based neural network controller for the autonomous landing of a quadrotor on moving targets," *Robotics*, vol. 7, no. 4, p. 71, 2018.
- [19] H. Razmi and S. Afshinfar, "Neural network-based adaptive sliding mode control design for position and attitude control of a quadrotor uav," *Aerospace Science and Technology*, vol. 91, pp. 12–27, 2019.
- [20] E. Okyere, A. Bousbaine, G. T. Poyi, A. K. Joseph, and J. M. Andrade, "LQR controller design for quad-rotor helicopters," *Journal of Engineering*, vol. 2019, no. 17, pp. 4003–4007, 2019.
- [21] E. Reyes-Valeria, R. Enriquez-Caldera, S. Camacho-Lara, and J. Guichard, "LQR control for a quadrotor using unit quaternions: modeling and simulation," in *Proceedings of the CONIELECOMP 2013, 23rd International Conference on Electronics, Communications and Computing*, pp. 172–178, IEEE, Cholula, Puebla, Mexico, March 2013.
- [22] T. Madani and A. Benallegue, "Backstepping control for a quadrotor helicopter," in *Proceedings of the 2006 IEEE/RSJ International Conference on Intelligent Robots and Systems*, pp. 3255–3260, IEEE, Beijing, China, October 2006.
- [23] A. Das, F. Lewis, and K. Subbarao, "Backstepping approach for controlling a quadrotor using Lagrange form dynamics," *Journal of Intelligent and Robotic Systems*, vol. 56, no. 1-2, pp. 127–151, 2009.
- [24] F. Chen, W. Lei, K. Zhang, G. Tao, and B. Jiang, "A novel nonlinear resilient control for a quadrotor uav via backstepping control and nonlinear disturbance observer," *Nonlinear Dynamics*, vol. 85, no. 2, pp. 1281–1295, 2016.
- [25] L. Luque-Vega, B. Castillo-Toledo, and A. G. Loukianov, "Robust block second order sliding mode control for a quadrotor," *Journal of the Franklin Institute*, vol. 349, no. 2, pp. 719–739, 2012.
- [26] K. Runcharoon and V. Srichatrapimuk, "Sliding mode control of quadrotor," in *Proceedings of the 2013 The International Conference on Technological Advances in Electrical, Electronics and Computer Engineering (TAECE)*, pp. 552–557, IEEE, Konya, Turkey, May 2013.
- [27] E.-H. Zheng, J.-J. Xiong, and J.-L. Luo, "Second order sliding mode control for a quadrotor UAV," *ISA Transactions*, vol. 53, no. 4, pp. 1350–1356, 2014.
- [28] G. V. Raffo, M. G. Ortega, and F. R. Rubio, "An integral predictive/nonlinear H_∞ control structure for a quadrotor helicopter," *Automatica*, vol. 46, no. 1, pp. 29–39, 2010.
- [29] N. Wang, Q. Deng, G. Xie, and X. Pan, "Hybrid finite-time trajectory tracking control of a quadrotor," *ISA Transactions*, vol. 90, pp. 278–286, 2019.
- [30] B. Tian, H. Lu, Z. Zuo, Q. Zong, and Y. Zhang, "Multivariable finite-time output feedback trajectory tracking control of quadrotor helicopters," *International Journal of Robust and Nonlinear Control*, vol. 28, no. 1, pp. 281–295, 2018.
- [31] L. Sun and Z. Zuo, "Nonlinear adaptive trajectory tracking control for a quad-rotor with parametric uncertainty," *Proceedings of the Institution of Mechanical Engineers-Part G: Journal of Aerospace Engineering*, vol. 229, no. 9, pp. 1709–1721, 2015.
- [32] R. Perez-Alcocer and J. Moreno-Valenzuela, "Adaptive control for quadrotor trajectory tracking with accurate parametrization," *IEEE Access*, vol. 7, pp. 53236–53247, 2019.
- [33] W. Wu, X. Jin, and Y. Tang, "Vision-based trajectory tracking control of quadrotors using super twisting sliding mode control," *Cyber-Physical Systems*, vol. 6, no. 4, pp. 207–230, 2020.
- [34] Y. Zhang, Z. Chen, and M. Sun, "Trajectory tracking control for a quadrotor unmanned aerial vehicle based on dynamic surface active disturbance rejection control," *Transactions of the Institute of Measurement and Control*, vol. 42, no. 12, pp. 2198–2205, 2020.
- [35] M. A. Mohd Basri, "Trajectory tracking control of autonomous quadrotor helicopter using robust neural adaptive backstepping approach," *Journal of Aerospace Engineering*, vol. 31, no. 2, Article ID 04017091, 2018.
- [36] S. Boyd, L. E. Ghaoui, E. Feron, and V. Belakrishnan, *Linear Matrix Inequalities in System and Control Theory*, Vol. 15, SIAM: Studies In Applied Mathematics, Philadelphia, PA, USA, 1994.
- [37] P. Gahinet, A. Nemirovski, A. J. Laub, and M. Chilali, *LMI Control Toolbox*, Math Works, Natick, MA, USA, 1995.
- [38] H. K. Khalil, *Nonlinear Control*, Pearson Higher Ed, New York, NY, USA, 2014.
- [39] F. Lewis, D. Dawson, and C. Abdallah, *Robot Manipulator Control: Theory and Practice*, CRC Press, Boca Raton, FL, USA, 2003.
- [40] A. Isidori, *Nonlinear Control Systems*, Springer, London, UK, 3rd edition, 1995.
- [41] DJI, *Description of the Dji Matrice 100 Quadcopter*, DJI, Nanshan, Shenzhen, China, 2019, <https://www.dji.com/mx/matrice100?site=brandsite&from=nav>.

Research Article

Controlling the PVTOL Aircraft System with an Inverted Pendular Load by means of Nested Saturation Functions and GPI Controller

Cesar Alejandro Villaseñor Rios , Octavio Gutiérrez-Frías , Carlos Aguilar-Ibanez ,
and Miguel S. Suarez-Castanon 

Instituto Politécnico Nacional, Mexico City, Mexico

Correspondence should be addressed to Octavio Gutiérrez-Frías; ogutierrezf@ipn.mx

Received 24 September 2021; Accepted 30 October 2021; Published 19 November 2021

Academic Editor: Baltazar Aguirre Hernandez

Copyright © 2021 Cesar Alejandro Villaseñor Rios et al. This is an open access article distributed under the Creative Commons Attribution License, which permits unrestricted use, distribution, and reproduction in any medium, provided the original work is properly cited.

This paper presents a control scheme that allows height position regulation and stabilization for an unmanned planar vertical takeoff and landing aircraft system with an inverted pendular load. The proposed controller consists of nested saturations and a generalized proportional integral (GPI). The GPI controls the aircraft height and the roll attitude; the latter is used as the fictitious input control. Next, the system is reduced through linear transformations, expressing it as an integrator chain with a nonlinear perturbation. Finally, the nested saturation function-based controller stabilizes the aircraft's horizontal position and the pendulum's angle. Obtaining the control approach was a challenging task due to the underactuated nature of the aircraft, particularly ensuring the pendulum's upright position. The stability analysis was based on the second method of Lyapunov using a simple candidate function. The numerical simulation confirmed the control strategy's effectiveness and performance. Additionally, the numerical simulation included a comparison against a PD controller, where its corresponding performance indexes were estimated, revealing that our controller had a better response in the presence of unknown disturbances.

1. Introduction

The control of underactuated mechanical systems is a widely studied field and continuously increases knowledge, mainly because controlling this kind of system is challenging since it has fewer controllers than degrees of freedom. The inverted pendulum system is a classic example of an underactuated system. It consists of a freely spinning load around an axis and attached to a base that freely moves forward and backward—multiple authors have proposed control laws to stabilize this kind of system in its inverted position. Block and Spong [1] proposed the partial feedback collocated and noncollocated control law for the stabilization around the origin of the acrobot and the pendubot. Fantoni and Lozano [2] proposed a nested saturation control for the wheeled inverted pendulum that enables stabilization around the origin. Ibañez and Frías [3] proposed a nested saturation control for the nonlinear

perturbed wheeled inverted pendulum, expressed it as a chain of integrators. The proposed control demonstrates asymptotical stability around the origin through the Lyapunov method when the pendulum angle is in the upper half-plane. The Furuta pendulum is another challenging system that has attracted the attention of several researchers, who have presented many interesting approaches to control this kind of pendulum. For instance, in [4], the authors proposed a Lyapunov-based control method for the stabilization around the origin, Furuta pendulum stabilization around the origin, while in [5], the authors introduced an active disturbance rejection-based control and its stability analysis. Another exciting example of underactuated systems is the unmanned aerial vehicle (UAV) such that this kind of system has been of high interest in the present century because of wide applications for different fields such as farming, photography, exploration, and military [6–8]. A typical example of a UAV is the planar vertical takeoff

and landing (PVTOL) aircraft, a simplified model of the actual vertical takeoff and landing aircraft [9], which encompasses almost all the dynamics found in real UAVs. The PVTOL has been used as a suitable benchmark to test new and existing controllers because it behaves like the well-known quadrotor in a two-dimensional plane. There exist many works that tackle the PVTOL stabilization problem. For instance, Aguilar-Ibanez et al. [10] proposed a control scheme using controlled Lagrangian for PVTOL stabilization. Fantoni et al. [11] introduced a control scheme using the PVTOL attitude as fictitious control and nested saturation technique for the stabilization at the origin. In [12], Lozano et al. showed that once controlling the PVTOL aircraft height, the system resembles an inverted pendulum, and using a change of coordinates, it can be seen as an integrator chain with nonlinear disturbance. Also, in this study, the authors present a nested saturation-based control and demonstrated asymptotic stabilization at the origin. In [13], based on the image-based visual servoing method and the backstepping technique, the authors presented a novel control strategy to force a vertical takeoff and landing (VTOL) aircraft. Works [14, 15] can be valuable sources for the readers interested in this problem.

Combining the inverted pendulum and UAV systems adds a degree of freedom, obtaining a system noneasy to stabilize. Hehn et al. [16] proposed this problem in 2011 and named it the flying inverted pendulum, consisting of an inverted pendulum attached to a quadcopter. The control goals of this study are stabilization at the origin and tracking a circular trajectory for the quadcopter, using linear quadratic regulator (LQR) control in both cases. The fact that the pendulum weights less than 5% of the UAV weight allows us to separate its corresponding dynamics. Some works found in the specialized literature deal with the control of the flying inverted pendulum using different control ideas [17–20], and some others consider the control of UAVs carrying loads (commonly known as the flying crane). This problem is closely related and relevant to the central control problem in this study. For instance, Nicotra et al. [21] showed that the linearized model of a quadcopter with a suspended load could be stabilized at the origin using nested saturation functions. Pizetta et al. in [22] proposed a total feedback control with an auxiliary controller to accomplish tracking trajectory; almost all the references therein were developed to test the PVTOL system indoors, mainly to avoid counteracting the undesirable effect of the wind, which is not an easy task. However, techniques for nonlinear systems can be applied to obtain robust controllers, as the controller developed in this study. Of these techniques, perhaps the most used are backstepping control [23, 24], fuzzy control [25–27], active disturbance rejection control approach [28], and others [29]. To the authors' knowledge, a general solution for stabilizing this type of system has not yet been reported in the literature.

In this context, we propose a control scheme for a PVTOL aircraft system with an inverted pendular load (PVTOL-ASIPL). This scheme mainly consists of a generalized proportional integral (GPI) controller and a nested saturation-based control. The GPI controller accomplishes height and roll attitude control, using the roll attitude angle as fictitious input control. Then, proposing a set of

convenient linear transformations and reducing the system can be expressed as a chain of integrators with a nonlinear perturbation. Finally, we design a nested saturation function-based controller to stabilize the horizontal position and the pendulum angle. Applying the second method of Lyapunov assures boundedness of the whole state and asymptotic convergence to the origin.

The main contributions of this study are as follows:

- (i) An algorithm control that uses a fictitious control, and we propose a combination of a GPI controller and a controller-based saturation for the takeoff and landing maneuvers
- (ii) A set of convenient transformations, in which a high-order system can be expressed as a various low-order system
- (iii) A control strategy for the PVTOL aircraft system with an inverted pendular load controls the height, roll attitude, horizontal position, and roll angle simultaneously, even in the presence of exogenous disturbance

The organization of the rest of this study is as follows. Section 2 introduces the model of PVTOL-ASIPL externally perturbed, obtained from the Euler–Lagrange formalism. Section 3 develops the control scheme design, while Section 4 presents the results of the numerical simulations. Finally, Section 5 is devoted to the concluding remarks and future work.

2. Dynamic Model

This section presents the dynamic model of the PVTOL aircraft system with an inverted pendular load (see Figure 1). The dynamic equations were obtained by the Euler–Lagrange formalism as follows:

$$\mathcal{L} = E_k - E_p, \quad (1)$$

where E_k and E_p are, respectively, the system kinetic and potential energies. Besides, the inverted pendular load base is in the PVTOL aircraft center of mass, $P_v = (x_v, y_v)$, α is defined as the angle between the PVTOL aircraft and the horizontal axis, and θ is the angle between the inverted pendular load and the vertical axis. Finally, the inverted pendular load center of mass ($P_p = (x_p, y_p)$) is defined as

$$\begin{aligned} x_p &= x_v - l_p \sin \theta, \\ y_p &= y_v + l_p \cos \theta. \end{aligned} \quad (2)$$

Therefore, Lagrangian of the system can be expressed as

$$\mathcal{L} = \frac{m_v \dot{p}_v \dot{p}_v^\top}{2} + \frac{m_p \dot{p}_p \dot{p}_p^\top}{2} + \frac{\alpha^2 i_v}{2} + \frac{\theta^2 i_p}{2} - m_v g y_v - m_p g y_p, \quad (3)$$

where m_v is the PVTOL aircraft mass, m_p is the pendular load mass, g is the gravity force, i_v is the PVTOL aircraft inertia, and i_p is the inverted pendular load inertia.

The Euler–Lagrange equations of motion for the PVTOL-ASIPL system are in the form of

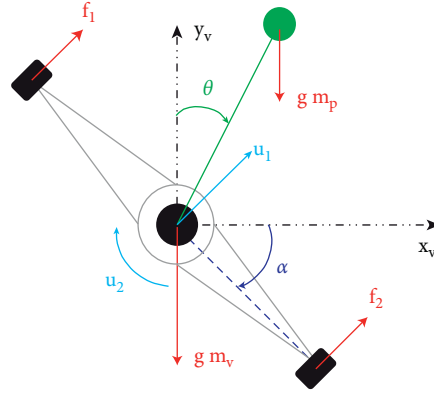


FIGURE 1: The PVTOL aircraft system with an inverted pendular load.

$$\frac{d}{dt} \frac{\partial \mathcal{L}}{\partial \dot{q}} - \frac{\partial \mathcal{L}}{\partial q} = \tau + D, \quad (4)$$

where $q = (x_v, y_v, \alpha, \theta)$ is the generalized coordinate vector, τ is the input control vector, and D is the external disturbance vector; without loss of generality, $i_v = 1$ and $i_p = 0$.

Developing Euler-Lagrange equation (4) leads to

$$l_p m_p \sin(\theta) \dot{\theta}^2 + (m_v + m_p) \ddot{x}_v - l_p m_p \cos(\theta) \ddot{\theta} = -u_1 \sin(\alpha) + D_x, \quad (5a)$$

$$-l_p m_p \cos(\theta) \dot{\theta}^2 + (m_v + m_p) (g + \ddot{y}_v - l_p m_p \sin(\theta) \ddot{\theta}) = u_1 \cos(\alpha) + D_y, \quad (5b)$$

$$i_v \dot{\alpha} = u_2 + D_\alpha, \quad (5c)$$

$$-l_p m_p \cos(\theta) (\ddot{x}_v - l_p m_p \sin(\theta) (g + \ddot{y}_v) + (i_p + l_p^2 m_p) \ddot{\theta}) = 0. \quad (5d)$$

Then, the equations in (5a) represent the PVTOL-ASIPL, and they can be expressed in a compact form as

$$M \ddot{q} + C(q, \dot{q}) \dot{q} + G = U + D, \quad (6)$$

with

$$M = \begin{bmatrix} m_v + m_p & 0 & 0 & -l_p m_p \cos(\theta) \\ 0 & (m_v + m_p) & 0 & -l_p m_p \sin(\theta) \\ 0 & 0 & i & 0 \\ -l_p m_p \cos(\theta) & -l_p m_p \sin(\theta) & 0 & (i_p + l_p^2 m_p) \end{bmatrix}, \quad (7)$$

$$C = \begin{bmatrix} 0 & 0 & 0 & l_p m_p \sin(\theta) \dot{\theta} \\ 0 & 0 & 0 & -l_p m_p \cos(\theta) \dot{\theta} \\ 0 & 0 & 0 & 0 \\ 0 & 0 & 0 & 0 \end{bmatrix},$$

$$G = \begin{bmatrix} 0 \\ m_v + m_p \\ 0 \\ -l_p m_p \sin(\theta) \end{bmatrix},$$

$$U = \begin{bmatrix} -u_1 \sin(\alpha) & u_1 \cos(\alpha) & u_2 & 0 \end{bmatrix}^T,$$

$$D = [D_x \ D_y \ D_\alpha \ D_\theta]^T,$$

where M is a positive semidefinite matrix, C is the Coriolis matrix, G is the gravity matrix, U is the input control matrix, and D is the external disturbance matrix. The terms D_x , D_y ,

and D_α are assumed to be unmodelled owing to the external disturbances and are defined as follows [30, 31]:

$$D_x = a_x \dot{x}_v, \quad (8a)$$

$$D_y = a_y \dot{y}_v, \quad (8b)$$

$$D_\alpha = a_\alpha \dot{\alpha}, \quad (8c)$$

$$D_\theta = 0. \quad (8d)$$

Finally, because M is not a singular matrix, it is possible to represent the dynamical model of the PVTOL aircraft system with an inverted pendular load as

$$\ddot{x}_v = \frac{e_{x1} + e_{x2}}{2m_v(m_v + m_p)}, \quad (9a)$$

$$\ddot{y}_v = \frac{e_{y1} + e_{y2}}{2m_v(m_v + m_p)}, \quad (9b)$$

$$\ddot{\alpha} = u_2 + a_\alpha \dot{\alpha}, \quad (9c)$$

$$\ddot{\theta} = \frac{-u_1 \sin(\alpha - \theta) + a_x \cos(\theta) \dot{x}_v + a_y \sin(\theta) \dot{y}_v}{l_p m}, \quad (9d)$$

where

$$\begin{aligned}
e_{x1} &= -u_1 \left((2m_v + m_p) \sin(\alpha) + m_p \sin(\alpha - 2\theta) \right), \\
e_{x2} &= a_x (2m_v + m_p + m_p \cos(2\theta)) \dot{x}_v + a_y m_p \sin(2\theta) \dot{y}_v - 2l_p m_v m_p \sin(\theta) \dot{\theta}^2, \\
e_{y1} &= -2gm_v (m_v + m_p) + (2m_v + m_p) u_1 \cos(\alpha) - m_p u_1 \cos(\alpha - 2\theta), \\
e_{y2} &= a_x m_p \sin(2\theta) \dot{x}_v + a_y (2m_v + m_p - m_p \cos(2\theta)) \dot{y}_v + 2l_p m_v m_p \cos(\theta) \dot{\theta}^2.
\end{aligned} \tag{10}$$

2.1. Problem Statement. The control goal consists in proposing an algorithm to accomplish stabilization at the origin of the PVTOL aircraft system with an inverted pendular load. The maneuvers are trajectory tracking tasks involving a step-by-step procedure, consisting of (1) the stabilization of the coordinate α ; (2) the stabilization of the coordinate y_v ; and (3) further stabilization of coordinates x_v and θ , even in the presence of disturbances due to the aerodynamic effects.

We have expressed the system in its minimal representation form, which will allow us to decouple it and simplify it. Instead of working with a complex system, we work with a few simple systems that embody the dynamics of the original one. We are now in a position to design and propose the control scheme in the following section.

3. Control Scheme

This section establishes the framework to solve the main control problem. To this end, please consider that the input control u_2 acts over α plus disturbance D_α . So, it is possible to design a control law for α using a fictitious controller for the PVTOL aircraft with an inverted pendular load [9, 11]. Then, through linear transformations, a GPI law is used for the PVTOL takeoff and landing maneuvers. Once the GPI law stabilized the PVTOL aircraft height, a change of coordinates allows expressing the system as a chain of integrators nonlinearly perturbed, allowing to propose the nested saturation function-based stabilizing controller. Figure 2 presents the schematic diagram of the closed-loop system.

3.1. Controlling the PVTOL Aircraft Attitude (α). It is clear that the third equation (9c) consists of a double-chain integrator with nonlinear disturbance D_α and control input u_2 . Then, a control law for tracking trajectory is searched for α .

3.1.1. Control Statement. The dynamical equation for the roll attitude angle (α) can be expressed as

$$\ddot{\alpha} = u_2 + \xi(t), \tag{11}$$

where $\xi(t)$ is a lumped generalized disturbance input.

Also, according to Lozano Hernández et al. and Fliess et al. [31, 32], to overcome the lack of available measurements of $\dot{\alpha}$, an integral reconstructor ($\hat{\alpha} = \int_0^t u(\tau) d\tau$)

can be proposed, and using the local approximation of the disturbance input, it is possible to propose the control input u_2 as

$$\begin{aligned}
u_2 &= \ddot{\alpha}_d - k_{\alpha_4} \dot{e}_\alpha - k_{\alpha_3} e_\alpha - k_{\alpha_2} \int_{\tau_1=0}^t e_\alpha d\tau_1 - k_{\alpha_1} \int_{\tau_1=0}^t \int_{\tau_2=0}^{\tau_1} e_\alpha d\tau_2 d\tau_1 \\
&\quad - k_{\alpha_0} \int_{\tau_1=0}^t \int_{\tau_2=0}^{\tau_1} \int_{\tau_3=0}^{\tau_2} e_\alpha d\tau_3 d\tau_2 d\tau_1,
\end{aligned} \tag{12}$$

where α_d is a smooth reference signal for the state α , which is twice differentiable. Also, $\dot{e}_\alpha = \dot{\alpha} - \dot{\alpha}_d$ and $e_\alpha = \alpha - \alpha_d$, and the relation between the actual value of $\dot{\alpha}$ and $\hat{\alpha}$ is expressed by

$$\dot{\alpha} = \hat{\alpha} + \int_0^t \xi(\tau) d\tau + \dot{\alpha}(0). \tag{13}$$

Substituting (12) into (11) and expressing the resulting dynamics in terms of the tracking error, the following dynamics are obtained:

$$e_\alpha^{(5)} + k_{\alpha_4} e_\alpha^{(4)} + k_{\alpha_3} e_\alpha^{(3)} + k_{\alpha_2} \ddot{e}_\alpha + k_{\alpha_1} \dot{e}_\alpha + k_{\alpha_0} e_\alpha = 0, \tag{14}$$

where k_{α_i} , with $i = 0, \dots, 4$, are selected such that characteristic polynomial $s^5 + k_{\alpha_4} s^4 + k_{\alpha_3} s^3 + k_{\alpha_2} s^2 + k_{\alpha_1} s + k_{\alpha_0} = 0$ is Hurwitz, reducing the undesirable effects of the nonlinear disturbances [33, 34]. So, the dynamic error is exponentially asymptotically stable at the origin. This fact allows using α_d as a fictitious control for subsystems (9a), (9b), and (9d). This proposal was previously used in other works dealing with the stabilization of PVTOL aircrafts [9, 12].

3.2. Simplified PVTOL Aircraft System with an Inverted Pendular Load. After $\alpha \rightarrow \alpha_d$ and applying the controller u_2 , the following system of equations represents the PVTOL aircraft system with an inverted pendular load:

$$\ddot{x}_v = \frac{e_{x1} + e_{x2}}{2m_v(m_v + m_p)}, \tag{15a}$$

$$\ddot{y}_v = \frac{e_{y1} + e_{y2}}{2m_v(m_v + m_p)}, \tag{15b}$$

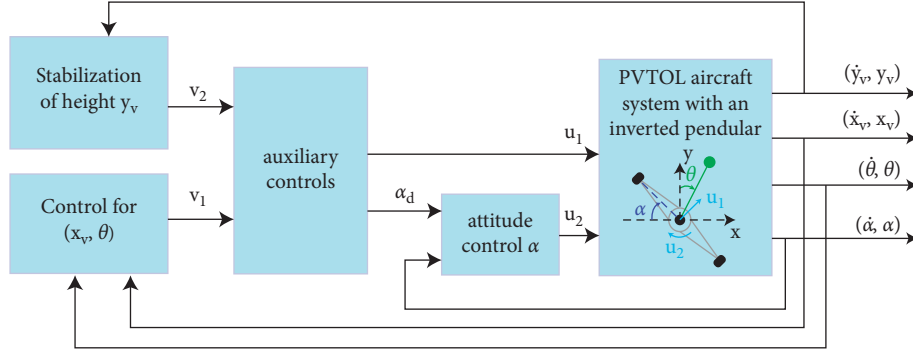


FIGURE 2: Control scheme of the PVTOL aircraft system with an inverted pendular load.

$$\ddot{\theta} = \frac{-u_1 \sin(\alpha_d - \theta) + a_x \cos(\theta) \dot{x}_v + a_y \sin(\theta) \dot{y}_v}{l p m}, \quad (15c) \quad \text{with}$$

$$\begin{aligned} e_{x1} &= -u_1 \left((2m_v + m_p) \sin(\alpha_d) + m_p \sin(\alpha_d - 2\theta) \right), \\ e_{x2} &= a_x (2m_v + m_p + m_p \cos(2\theta)) \dot{x}_v + a_y m_p \sin(2\theta) \dot{y}_v - 2l_p m_v m_p \sin(\theta) \dot{\theta}^2, \\ e_{y1} &= -2gm_v (m_v + m_p) + (2m_v + m_p) u_1 \cos(\alpha_d) - m_p u_1 \cos(\alpha_d - 2\theta), \\ e_{y2} &= a_x m_p \sin(2\theta) \dot{x}_v + a_y (2m_v + m_p - m_p \cos(2\theta)) \dot{y}_v + 2l_p m_v m_p \cos(\theta) \dot{\theta}^2, \end{aligned} \quad (16)$$

where α_d and u_1 are the input controls.

Thus, we propose the following control laws [12]:

$$u_1 = \sqrt{r_1^2 + r_2^2}, \quad (17a)$$

$$\alpha_d = \arctan\left(\frac{r_2}{r_1}\right), \quad (17b)$$

where $r_1 > 0$ and $r_2 > 0$ are auxiliary control inputs.

To obtain the dynamic model, the following change of coordinates is applied to model (15a)–(15c):

$$x_v = \frac{\hat{x}_v}{2m_v(m_v + m_p)}, \quad (18a)$$

$$y_v = \frac{\hat{y}_v}{2m_v(m_v + m_p)}, \quad (18b)$$

$$\theta = \frac{\hat{\theta}}{l_p m_v}. \quad (18c)$$

Therefore, models (15a)–(15c) transform into the following system:

$$\begin{aligned} \ddot{\hat{x}}_v &= -(2m_v + m_p)(r_2 - a_x \dot{x}_v) + m_p \cos(2\theta)(-r_2 + a_x \hat{x}_v) \\ &\quad + m_p \sin(2\theta)(r_1 + a_y \dot{y}_v) - 2l_p m_v m_p \sin(\theta) \dot{\theta}^2, \end{aligned} \quad (19)$$

$$\begin{aligned} \ddot{\hat{y}}_v &= -2gm_v(m_v + m_p) + (2m_v + m_p)r_1 - m_p(r_1 \cos(2\theta) + r_2 \sin(2\theta)), \\ &\quad + a_x m_p \sin(2\theta) \dot{x}_v + a_y (2m_v + m_p - m_p \cos(2\theta)) \dot{y}_v + 2l_p m_v m_p \cos(\theta) \dot{\theta}^2 \\ \ddot{\hat{\theta}} &= \cos(\theta)(-r_2 + a_x \hat{x}_v) + \sin(\theta)(r_1 + a_y \dot{y}_v). \end{aligned} \quad (20)$$

Hence, system (19) takes the compact form with

$$\begin{bmatrix} \ddot{\hat{x}}_v \\ \ddot{\hat{y}}_v \end{bmatrix} = M_2 \begin{bmatrix} r_1 \\ r_2 \end{bmatrix} + C_2, \quad (21)$$

$$M_2 = \begin{bmatrix} m_p \sin(2\theta) & -(2m_v + m_p + m_p \cos(2\theta)) \\ (2m_v + m_p) - m_p \cos(2\theta) & -m_p \sin(2\theta) \end{bmatrix}, \quad (22)$$

$$C_2 = \begin{bmatrix} -2l_p m_v m_p \sin(\theta) \dot{\theta}^2 \\ -2gm_v(m_v + m_p) + 2l_p m_v m_p \cos(\theta) \dot{\theta}^2 - 2gm_v(m_v + m_p) \end{bmatrix}.$$

Then, given system (19) and ignoring the effect of the disturbances, the following partial feedback control can be proposed [1, 9]:

$$\begin{bmatrix} r_1 \\ r_2 \end{bmatrix} = M_2^{-1} \left(-C_2 + \begin{bmatrix} v_1 \\ v_2 \end{bmatrix} \right), \quad (23)$$

where v_1 and v_2 are new auxiliary control inputs. Thus, the system defined by equation (19), in a closed loop with control model (23), leads us to obtain the following system:

$$\ddot{\hat{x}}_v = v_1 + a_x (2m_v + m_p + m_p \cos(2\theta)) \dot{\hat{x}}_v + a_y m_p \sin(2\theta) \dot{\hat{y}}_v, \quad (24a)$$

$$\ddot{\hat{y}}_v = v_2 + a_x m_p \sin(2\theta) \dot{\hat{x}}_v + a_y (2m_v + m_p - m_p \cos(2\theta)) \dot{\hat{y}}_v, \quad (24b)$$

$$\ddot{\theta} = \frac{\cos(\theta)(v_1 + 2a_x(m_v + m_p)\dot{\hat{x}}) + \sin(\theta)(2gm_v(m_v + m_p) + v_2 + 2a_y(m_v + m_p)\dot{\hat{y}})}{2(m_v + m_p)}. \quad (24c)$$

Notice that the above system is the reduced model for the PVTOL aircraft system with an inverted pendular load, with v_1 and v_2 as the control inputs.

takeoff and landing of the PVTOL aircraft system with an inverted pendular load.

3.3. Stabilization of Height y_v . A GPI controller with a saturation function is applied to obtain the height position control, allowing the tracking control to accomplish the

3.3.1. Control Statement. Consider the vertical displacement y_v described by (25), and let v_2 be the control input defined as (26):

$$v_2 = \sigma_a \left(\dot{y}_d - k_{y_4} \dot{e}_y - k_{y_3} e_y - k_{y_2} \int_{\tau_1=0}^t e_y d\tau_1 - k_{y_1} \int_{\tau_1=0}^t \int_{\tau_2=0}^{\tau_1} e_y d\tau_2 d\tau_1 - k_{y_0} \int_{\tau_1=0}^t \int_{\tau_2=0}^{\tau_1} \int_{\tau_3=0}^{\tau_2} e_y d\tau_3 d\tau_2 d\tau_1 \right) = \sigma_a(u_{gpi}), \quad (25)$$

where y_d is a smooth reference signal twice derivable and $e_y = y_d - \hat{y}_v$.

Also, $\sigma_L(q)$ is a saturation function defined as

$$\sigma_a(q) = \begin{cases} \text{if } q > a, & a, \\ \text{if } q < -a, & -a, \\ \text{if } -a < q < a, & q. \end{cases} \quad (26)$$

Thus, the tracking trajectory error e_y is exponentially asymptotically stable.

Proof. The proof is split into two parts. First, it is proven that a saturation function in finite time bounds the error dynamics e_y . Then, we demonstrate exponentially asymptotic stability. \square

3.3.2. Error Bounded. The tracking trajectory error is defined as

$$e_y = y_d - \hat{y}_v, \quad (27)$$

$$\dot{V}_y = e_1 e_2 + e_2 \dot{e}_2 = e_1 e_2 + e_2 (\ddot{y}_d - \sigma_a(u_{gpi}) - a_x m_p \sin(2\theta) \dot{\hat{x}}_v - a_y (2m_v + m_p - m_p \cos(2\theta)) \dot{\hat{y}}_v). \quad (31)$$

Thus, the first and second time derivatives of y_d are known and bounded as $|M_{y_d}|$. Besides, in a close neighbourhood where e_1 and e_2 are such that $|e_1| \leq \delta_{e_1}$ and $|e_2| \leq \delta_{e_2}$, the saturation function fulfills $\sigma_a(s) \leq 0$. So, parameters were designed as k_{y_i} in u_{gpi} such that e_2 is dominant, and $e_2 \sigma_a(u_{gpi}) > 0$. Finally, the last terms of equation (31) satisfy the following:

$$|a_x m_p \sin(2\theta)| \leq \delta_x, \quad (32)$$

$$|a_y (2m_v + m_p - m_p \cos(2\theta))| \leq \delta_y. \quad (33)$$

where y_d is the desired height position.

Let us define the following state variables as

$$e_1 = e_y; e_2 = \dot{e}_y. \quad (28)$$

Therefore, the dynamic error is transformed into the following system:

$$\dot{e}_1 = e_2, \quad (29a)$$

$$\dot{e}_2 = y_d - v_2 - a_x m_p \sin(2\theta) \dot{\hat{x}}_v - a_y (2m_v + m_p - m_p \cos(2\theta)) \dot{\hat{y}}_v, \quad (29b)$$

where v_2 is the control input.

Now, to use the second method of Lyapunov, consider the following candidate function:

$$V_y = \frac{e_1^2}{2} + \frac{e_2^2}{2}, \quad (30)$$

which is positive definite, with time derivative

Therefore, computing the time derivative of the candidate Lyapunov function leads to

$$\dot{V}_y = \delta_{e_1} \delta_{e_2} + \delta_{e_2} M_{y_d} - e_2 \sigma_a(u_{gpi}) - \delta_{e_2} \delta_x \dot{\hat{x}}_v - \delta_{e_2} \delta_y \dot{\hat{y}}_v, \quad (34)$$

and if $\dot{\hat{x}}_v$ and $\dot{\hat{y}}_v$ are small enough such that $e_2 \sigma_a(u_{gpi}) > \delta_{e_1} \delta_{e_2} + \delta_{e_2} M_{y_d} - \delta_{e_2} \delta_x \dot{\hat{x}}_v - \delta_{e_2} \delta_y \dot{\hat{y}}_v$, then $\dot{V}_y < 0$ and \hat{y}_v are bounded in finite time. Thus, after time T , when this condition is satisfied, control law (26) takes the following structure:

$$v_2 = y_d - k_{y_4} \dot{e}_y - k_{y_3} e_y - k_{y_2} \int_{\tau_1=0}^t e_y d\tau_1 - k_{y_1} \int_{\tau_1=0}^t \int_{\tau_2=0}^{\tau_1} e_y d\tau_2 d\tau_1 - k_{y_0} \int_{\tau_1=0}^t \int_{\tau_2=0}^{\tau_1} \int_{\tau_3=0}^{\tau_2} e_y d\tau_3 d\tau_2 d\tau_1. \quad (35)$$

From the above, equation (24b) is expressed as

$$\ddot{\hat{y}}_v = v_2 + \xi_1(t), \quad (36)$$

where $\xi_1(t)$ is a lumped generalized disturbance input.

Then, to overcome the lack of available measurements of $\dot{\hat{y}}_v$, the following integral reconstructor is introduced [31]:

$$\overline{\hat{y}}_v = \int_0^t v_2(\tau) d\tau. \quad (37)$$

Using the local approximation of the disturbance input, the relation between the actual value of $\dot{\hat{y}}_v$ and $\overline{\hat{y}}_v$ is expressed by

$$\dot{\hat{y}}_v = \overline{\hat{y}}_v + \int_0^t \xi(\tau) d\tau + \dot{\hat{y}}_v(0). \quad (38)$$

Now, differentiating equation (38) and substituting into (36), the control law v_2 takes the form

$$\begin{aligned}
v_2 = & \ddot{y}_d - k_{y_4} \dot{\bar{e}}_y - k_{y_3} \bar{e}_y - k_{y_2} \int_{\tau_1=0}^t \bar{e}_y d\tau_1 - k_{y_1} \int_{\tau_1=0}^t \int_{\tau_2=0}^{\tau_1} \bar{e}_y d\tau_2 d\tau_1 \\
& - k_{y_0} \int_{\tau_1=0}^t \int_{\tau_2=0}^{\tau_1} \int_{\tau_3=0}^{\tau_2} \bar{e}_y d\tau_3 d\tau_2 d\tau_1,
\end{aligned} \tag{39}$$

with $\bar{e}_y = y_v - y_d$ and $\dot{\bar{e}}_y = \dot{\bar{y}}_v - \dot{y}_d$.

Substituting (39) into (36) is possible to express the dynamic error \bar{e}_y as follows:

$$\bar{e}_y^{(5)} + k_{y_4} \bar{e}_y^{(4)} + k_{y_3} \bar{e}_y^{(3)} + k_{y_2} \ddot{\bar{e}}_y + k_{y_1} \dot{\bar{e}}_y + k_{y_0} \bar{e}_y = 0. \tag{40}$$

The coefficients k_{y_4} , k_{y_3} , k_{y_2} , k_{y_1} , and k_{y_0} are selected such that the polynomial $S^{(5)} + k_{y_4} S^{(4)} + k_{y_3} S^{(3)} + k_{y_2} S^2 + k_{y_1} S + k_{y_0}$ is Hurwitz, eliminating the nonlinear disturbances [33]. Then, tracking trajectory error \bar{e}_y is exponentially asymptotically stable to zero.

3.4. Control for (x_v, θ) . This section proposes a nested saturation-based controller strategy to stabilize the PVTOL-ASIPL horizontal position and roll angle. Notice that the nested saturation-based controller strategy allows stabilizing nonlinear systems that can be approximately expressed as a chain of integrators [35–37]. Thus, our stability problem will be solved as follows. First, we introduce a linear transformation for the stabilizing controller. Then, we demonstrate that the proposed controller guarantees boundedness and converges to zero, in finite time, of the whole state.

3.5. Expressing the PVTOL-ASIPL as a Chain of Integrators. After the application of the controller v_2 , system (25) can be reduced to the subsystem (\hat{x}_v, θ) as follows:

$$\begin{aligned}
\ddot{\hat{x}}_v &= v_1 + a_x(2m_v + m_p + m_p \cos(2\theta))\dot{\hat{x}}_v, \\
\ddot{\theta} &= \frac{2gm_v(m_v + m_p)\sin(\theta) + \cos(\theta)(v_1 + 2a_x(m_v + m_p)\dot{\hat{x}}_v)}{2(m_v + m_p)}.
\end{aligned} \tag{41}$$

Then, introduce the following coordinates' change:

$$\begin{aligned}
\hat{x}_v &= x_v(-2gm_v(m_v + m_p)), \\
\hat{\theta} &= \theta(gm_v), \\
v_1 &= 2(m_v + m_p)(gm_v(v \sec(\theta) - \tan(\theta)) - a_x \dot{\hat{x}}_v).
\end{aligned} \tag{42}$$

System (42) takes the following form:

$$\begin{aligned}
\ddot{\hat{x}}_v &= v \sec(\theta) - \tan(\theta) - \epsilon_x \sin(\theta)^2 \dot{\hat{x}}_v, \\
\ddot{\hat{\theta}} &= v,
\end{aligned} \tag{43}$$

where $\epsilon_x \sin(\theta)^2 \dot{\hat{x}}_v$ is considered as a nonlinear disturbance and ϵ_x is an unknown constant that depends on variables m_v, m_p, g , and a_x (Note that $\epsilon_x = (m_p/g * m_v * (m_v + m_p))a_x$). Notice that subsystem (43) is similar to the cart-pole system plus a nonlinear disturbance [38].

3.5.1. Control Statement. Based on work [3], we define the following state variables $x_1 = x_v, x_2 = \dot{x}_v, \theta_1 = \theta$, and $\theta_2 = \dot{\theta}$. Then, we express the dynamic system as

$$\begin{aligned}
\dot{x}_1 &= x_2, \\
\dot{x}_2 &= -v \sec(\theta_1) + \tan(\theta_1) + \epsilon_x \sin(\theta_1)^2 x_2, \\
\dot{\theta}_1 &= \theta_2, \\
\dot{\theta}_2 &= v.
\end{aligned} \tag{44}$$

To express system (44) as a chain of integrators with a nonlinear perturbation and propose a controller for the stabilization of the subsystem (x_v, θ) , applying the decoupling theorem [3, 39], the following global nonlinear transformation is introduced:

$$z_1 = \frac{1 + \tan(\theta_1/2)}{1 - \tan(\theta_1/2)} + x_1, \tag{45a}$$

$$z_2 = \frac{\theta_2}{\cos(\theta_1) + x_2}, \tag{45b}$$

$$\omega_1 = \tan(\theta_1), \tag{45c}$$

$$\omega_2 = \theta_2 \sec^2(\theta_1), \tag{45d}$$

$$v_f = \sec^2(\theta_1)v + 2\theta_2^2 \tan(\theta_1) \sec^2(\theta_1). \tag{45e}$$

Hence, the transformed system into a chain of integrators is given by

$$\begin{aligned}
\dot{z}_1 &= z_2, \\
\dot{z}_2 &= \omega_1 + \frac{\omega_1 \omega_1^2}{(1 + \omega_1^2)} + \frac{\epsilon_x \omega_2 \omega_1^2}{(1 + \omega_1^2)^{3/2}} - \frac{\epsilon_x z_2 \omega_1^2}{1 + \omega_1^2}, \\
\dot{\omega}_1 &= \omega_2, \\
\dot{\omega}_2 &= v_f.
\end{aligned} \tag{46}$$

3.6. Nested Saturation Function-Based Controller. Inspired by Teel [40], a linear transformation is proposed to obtain the stabilizing controller for system (46) as follows:

$$\begin{bmatrix} q_1 \\ q_2 \\ q_3 \\ q_4 \end{bmatrix} = \begin{bmatrix} 1 & 3 & 3 & 1 \\ 0 & 1 & 2 & 1 \\ 0 & 0 & 1 & 1 \\ 0 & 0 & 0 & 1 \end{bmatrix} \begin{bmatrix} z_1 \\ z_2 \\ \omega_1 \\ \omega_2 \end{bmatrix}. \tag{47}$$

Applying transformation (47) to system (46) leads to

$$\begin{aligned}
\dot{q}_1 &= v_f + q_2 + q_3 + q_4 + 3G_1(q_3 - q_4)q_4^2 \\
&\quad + 3G_2(q_3 - q_4)q_4e_x + 3G_3(q_3 - q_4)(q_2 - 2q_3 + q_4)e_x, \\
\dot{q}_2 &= v_f + q_3 + q_4 + G_1(q_3 - q_4)q_4^2 \\
&\quad + G_2(q_3 - q_4)q_4e_x + G_3(q_3 - q_4)(q_2 - 2q_3 + q_4)e_x, \\
\dot{q}_3 &= v_f + q_4, \\
\dot{q}_4 &= v_f,
\end{aligned} \tag{48}$$

for which the following nested saturation function-based stabilizing controller is proposed:

$$v_f = -\sigma_{c_1}(q_4 + \sigma_{c_2}(q_3 + \sigma_{c_3}(q_2 + \sigma_{c_4}(q_1))))), \tag{49}$$

where σ_{c_i} is defined by equation (26), and G_i with $i = 1, 2, 3$ is given by

$$G_1(s) = \frac{s}{(1+s^2)^{3/2}}, \tag{50a}$$

$$G_2(s) = \frac{s^2}{(1+s^2)^{3/2}}, \tag{50b}$$

$$G_3(s) = \frac{s^2}{1+s^2}. \tag{50c}$$

Remark 1. Note that $\max(G_1(s)) = K_1 = 2/(3\sqrt{3})$ when $s = 1/\sqrt{2}$ and $\min(G_1(s)) = -2/(3\sqrt{3})$ when $s = -1/\sqrt{2}$ and $\lim_{s \rightarrow \inf} G_1(s) = 0$. Besides, $\max(G_2(s)) = K_2 = 2/(3\sqrt{3})$ when $s = \pm\sqrt{2}$ and $\min(G_1(s)) = 0$ when $s = 0$ and $\lim_{s \rightarrow \inf} G_2(s) = 0$. Additionally, $\min(G_3(s)) = 0$ when $s = 0$ and $\lim_{s \rightarrow \inf} G_3(s) = K_3 = 1$.

3.7. Whole State Boundedness. Now, we prove that the proposed controller (49) ensures whole state boundedness. Moreover, the bound of each state directly depends on the designed parameters of the controller.

Step 1. A positive definite function is defined as

$$V_4 = \frac{q_4^2}{2}. \tag{51}$$

The time derivative of V_4 is expressed by

$$\dot{V}_4 = q_4\dot{q}_4 = q_4v_f = -q_4\sigma_{c_1}(q_4 + \sigma_{c_2}(q_3 + \sigma_{c_3}(q_2 + \sigma_{c_4}(q_1))))), \tag{52}$$

where c_1 and c_2 are selected such that $c_1 > 2c_2$. It is clear that $\dot{V}_4 < 0$ when $|q_4| \geq c_2$; therefore, there exists a finite time $T_1 > 0$ such that

$$|q_4| \leq c_2, \quad \forall t > T_1. \tag{53}$$

Thus, when this condition is satisfied, the control law (49) takes the following structure:

$$v_f = -q_4 - \sigma_{c_2}(q_3 + \sigma_{c_3}(q_2 + \sigma_{c_4}(q_1))). \tag{54}$$

Step 2. Behaviour analysis of q_3 : let us consider the following positive definite function:

$$V_3 = \frac{q_3^2}{2}. \tag{55}$$

Differentiating it with respect to time and after substituting (54) into \dot{q}_3 , the following expression is obtained:

$$\dot{V}_3 = q_3\dot{q}_3 = q_3(v_f + q_4) = -q_3\sigma_{c_2}(q_3 + \sigma_{c_3}(q_2 + \sigma_{c_4}(q_1))). \tag{56}$$

To ensure that $\dot{V}_3 < 0$ is achieved, the following conditions must be satisfied:

$$c_2 > 2c_3, \quad |q_3| \geq c_3. \tag{57}$$

Then, there exists a finite time $T_2 > T_1$ after which

$$|q_3| \leq c_3, \quad \forall t > T_2. \tag{58}$$

Therefore, q_3 is bounded, and the control law takes the following form:

$$v_f = -q_4 - q_3 - \sigma_{c_3}(q_2 + \sigma_{c_4}(q_1)). \tag{59}$$

Step 3. The following positive definite function is introduced:

$$V_2 = \frac{q_2^2}{2}. \tag{60}$$

Differentiating V_2 and after substituting (60) into the second equation of (48), the following is obtained:

$$\begin{aligned}
\dot{V}_2 = q_2\dot{q}_2 &= -q_2[\sigma_{c_3}(q_2 + \sigma_{c_4}(q_1)) - G_1(q_3 - q_4)q_4^2 \\
&\quad - G_2(q_3 - q_4)q_4e_x - G_3(q_3 - q_4)(q_2 - 2q_3 + q_4)],
\end{aligned} \tag{61}$$

where c_3 and c_2 must satisfy the relation $c_3 > 2c_4 + G_1(q_3 - q_4)q_4^2 + G_2(q_3 - q_4)q_4e_x + G_3(q_3 - q_4)(q_2 - 2q_3 + q_4)$. It is easy to observe that if $|q_2| > c_4 + G_2(q_3 - q_4)q_4e_x + G_3(q_3 - q_4)(q_2 - 2q_3 + q_4)$, $\dot{V}_2 < 0$. Hence, there exists a finite time $T_3 > T_2$ after which

$$\begin{aligned}
|q_2| &\leq c_4 + G_2(q_3 - q_4)q_4e_x \\
&\quad + G_3(q_3 - q_4)(q_2 - 2q_3 + q_4); \quad \forall t > T_3.
\end{aligned} \tag{62}$$

Therefore, q_2 is bounded, and the control v_f is revealed to be

$$v_f = -q_4 - q_3 - q_2 - \sigma_{c_4}(q_1). \tag{63}$$

Step 4. Substituting (63) into the first equation of (48), we obtain

$$\dot{q}_1 = -\sigma_{c_4}(q_1) + 3G_1(q_3 - q_4)q_4^2 + 3G_2(q_3 - q_4)q_4\epsilon_x + 3G_3(q_3 - q_4)(q_2 - 2q_3 + q_4)\epsilon_x. \quad (64)$$

To demonstrate that q_1 is bounded, a positive definite function is defined as follows:

$$V_1 = \frac{q_1^2}{2}. \quad (65)$$

Differentiating V_1 along the trajectories of (66) leads to

$$\begin{aligned} \dot{V}_1 = q_1\dot{q}_1 = & -q_1(\sigma_{c_4}(q_1) - 3G_1(q_3 - q_4)q_4^2 \\ & - 3G_2(q_3 - q_4)q_4\epsilon_x - 3G_3(q_3 - q_4)(q_2 - 2q_3 + q_4)), \end{aligned} \quad (66)$$

where c_4 must be selected so that $c_4 > 3G_1(q_3 - q_4)q_4^2 + 3G_2(q_3 - q_4)q_4\epsilon_x + 3G_3(q_3 - q_4)(q_2 - 2q_3 + q_4)$ and $|q_1| > 3G_1(q_3 - q_4)q_4^2 + 3G_2(q_3 - q_4)q_4\epsilon_x + 3G_3(q_3 - q_4)(q_2 - 2q_3 + q_4)$ to achieve $V_1 < 0$. Therefore, there exists a finite time $T_4 > T_3$ such that

$$|q_1| < 3G_1(q_3 - q_4)q_4^2 + 3G_2(q_3 - q_4)q_4\epsilon_x + 3G_3(q_3 - q_4)(q_2 - 2q_3 + q_4), \quad \forall t > T_4. \quad (67)$$

Consequently, q_1 is also bounded. Finally, the values of parameters c_1, c_2, c_3 , and c_4 can be determined by the following inequalities:

$$\begin{aligned} c_1 &> 2c_2, \\ c_2 &> 2c_3, \\ c_3 &> 2c_4 + G_1(q_3 - q_4)q_4^2 + G_2(q_3 - q_4)q_4\epsilon_x + G_3(q_3 - q_4)(q_2 - 2q_3 + q_4), \\ c_4 &> 3G_1(q_3 - q_4)q_4^2 + 3G_2(q_3 - q_4)q_4\epsilon_x + 3G_3(q_3 - q_4)(q_2 - 2q_3 + q_4). \end{aligned} \quad (68)$$

From the above conditions, the set of control parameters can be selected as

$$\begin{aligned} c_1 &= 28r, \\ c_2 &= 14r, \\ c_3 &= 7r, \\ c_4 &= 3r, \end{aligned} \quad (69)$$

where r is directly related to the magnitude of the system disturbances.

3.8. Whole State Convergence to Zero. Here, we prove that the closed-loop system, provided by (48) and (49) and satisfying (70), is asymptotically stable.

Notice that, after $t > T_4$, the control law (49) is no longer saturated; that is,

$$v_f = -q_4 - q_3 - q_2 - q_1, \quad (70)$$

and the closed-loop system turns out to be

$$\begin{aligned} \dot{q}_1 &= -q_1 + 3G_1(q_3 - q_4)q_4^2 \\ &+ 3G_2(q_3 - q_4)q_4\epsilon_x + 3G_3(q_3 - q_4)(q_2 - 2q_3 + q_4)\epsilon_x, \\ \dot{q}_2 &= -q_1 - q_2 + G_1(q_3 - q_4)q_4^2 \\ &+ G_2(q_3 - q_4)q_4\epsilon_x + G_3(q_3 - q_4)(q_2 - 2q_3 + q_4)\epsilon_x, \\ \dot{q}_3 &= -q_1 - q_2 - q_3, \\ \dot{q}_4 &= -q_1 - q_2 - q_3 - q_4. \end{aligned} \quad (71)$$

To demonstrate whole state convergence to zero, the following Lyapunov function is used:

$$V = \frac{1}{2}q^T q, \quad (72)$$

where $q = [q_1, q_2, \dots, q_3, q_4]^T$, and differentiating V along the trajectories of equation (72), it is obtained that

$$\begin{aligned} \dot{V} = & -q^T M q + (3q_1 + q_2)(G_1(q_3 - q_4)q_4^2 \\ & + G_2(q_3 - q_4)q_4\epsilon_x + G_3(q_3 - q_4)(q_2 - 2q_3 + q_4)\epsilon_x), \end{aligned} \quad (73)$$

and

$$M = \begin{bmatrix} 1 & \frac{1}{2} & \frac{1}{2} & \frac{1}{2} \\ \frac{1}{2} & 1 & \frac{1}{2} & \frac{1}{2} \\ \frac{1}{2} & \frac{1}{2} & 1 & \frac{1}{2} \\ \frac{1}{2} & \frac{1}{2} & \frac{1}{2} & 1 \end{bmatrix}, \quad (74)$$

with M being positive definite with $\lambda_{\min}(M)1/2$.

From Remark 1, it is shown that the following relations are satisfied:

$$\begin{aligned} |(3q_1 + q_2)G_1(q_3 - q_4)q_4^2| &< \frac{K_1}{2} |(3q_1 + q_2)q_4^2| < \frac{K_1}{2} ((3q_1 + q_2)^2 + q_4^4), \\ |(3q_1 + q_2)G_2(q_3 - q_4)q_4\epsilon_x| &< \frac{K_2\epsilon_x}{2} |(3q_1 + q_2)q_4| < \frac{K_2\epsilon_x}{2} ((3q_1 + q_2)^2 + q_4^2), \\ |(3q_1 + q_2)G_3(q_3 - q_4)q_2\epsilon_x| &< \frac{K_3\epsilon_x}{2} |(3q_1 + q_2)q_2| < \frac{K_3\epsilon_x}{2} ((3q_1 + q_2)^2 + q_2^2), \\ |(3q_1 + q_2)G_3(q_3 - q_4)q_4\epsilon_x| &< \frac{K_3\epsilon_x}{2} |(3q_1 + q_2)q_4| < \frac{K_3\epsilon_x}{2} ((3q_1 + q_2)^2 + q_4^2). \end{aligned} \quad (75)$$

So, \dot{V} fulfills

$$\begin{aligned} \dot{V} &< -\frac{1}{2} [q_1^2 - K_1(3q_1 + q_2)^2 - K_2\epsilon_x(3q_1 + q_2)^2 - 2K_3\epsilon_x(3q_1 + q_2)^2] \\ &\quad - \frac{1}{2} q_4^2 [1 - K_1q_4^2 - K_3\epsilon_x] - \frac{1}{2} q_2^2 [1 - K_2\epsilon_x]. \end{aligned} \quad (76)$$

Hence, the previous inequality is strictly negative definite, and the following constraints are obtained:

$$\begin{aligned} q_1^2 - K_1(3q_1 + q_2)^2 - K_2\epsilon_x(3q_1 + q_2)^2 - 2K_3\epsilon_x(3q_1 + q_2)^2 &> 0, \\ 1 - K_1q_4^2 - K_3\epsilon_x &> 0, \\ 1 - K_2\epsilon_x &> 0. \end{aligned} \quad (77)$$

Therefore, if the restrictions of (77) are fulfilled, \dot{V} is strictly negative, and the state vector q exponentially converges to zero after $t > T_4$.

The following proposition summarizes the previous discussion, which is the main result of our study.

Proposition 1. *Consider the PVTOL aircraft system with an inverted pendular load as described in (9) and in a closed loop with controllers (12), (17a) and (17b), (23), (25), and (49). Then, the closed-loop system is exponentially asymptotically stable provided that the control parameters c_1 , c_2 , c_3 , and c_4 satisfy inequalities (69), and k_{α_i} and k_{γ_i} are selected such that the characteristic polynomial is Hurwitz.*

Finally, in Figure 3, the steps' sequence is shown, obtained from the control laws u_1 and u_2 .

Having designed the control scheme for the PVTOL aircraft system with an inverted pendular load and carried out its convergence analysis, we test its effectiveness through numerical simulations in the following section. It is worth mentioning that it would be ideal for testing the scheme by conducting actual experiments—unfortunately, the construction of the needed prototype is still in progress.

4. Numerical Simulations

To test the controllers' performance, we carried out some numerical simulations using the MATLAB-Simulink program, and the results were obtained based on the numerical method of Runge–Kutta of the fourth order with a fixed step of 0.01 s. The physical parameters of the system are $m_p = 0.2$ kg, $m_v = 0.8$ kg, $l_p = 0.2$ m, and $g = 9.8$ m/s². Also, the tuning parameters proposed for each controller are listed in Table 1. Notice that the controller parameter values u_2 and v_2 were selected such that the error dynamics is equal to the desired closed-loop polynomial $(s^2 + 2\zeta\omega_n s + \omega_n^2)(s + \beta)$.

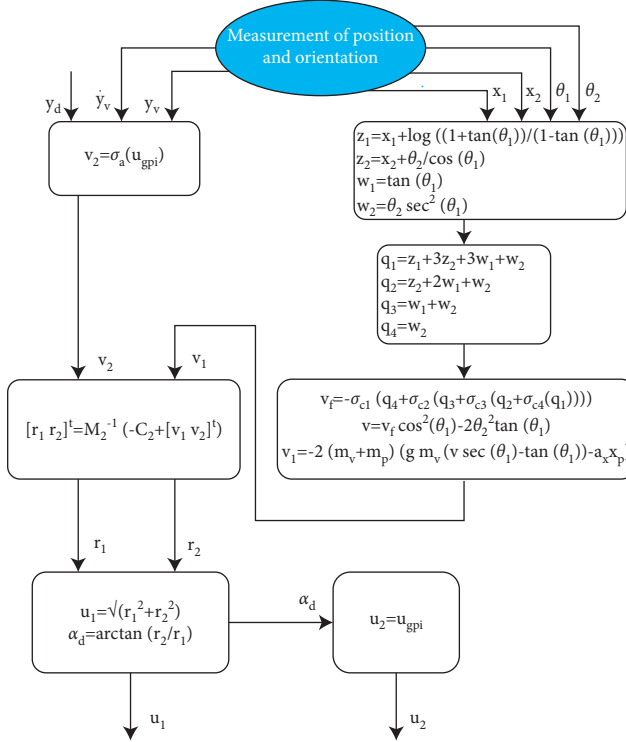


FIGURE 3: Control strategy sequence.

TABLE 1: Tuning parameters for controllers.

Controller	Control parameter	Gain
u_2	L	3
	k_{α_0}	167
	k_{α_1}	299
	k_{α_2}	183
	k_{α_3}	62
	k_{α_4}	11
	a	1.45
	k_{y_0}	167
	k_{y_1}	299
	k_{y_2}	183
v_2	k_{y_3}	62
	k_{y_4}	1
	c_1	0.11
v_f	c_2	0.24
	c_3	0.49
	c_4	0.99

Besides, the parameters of v_f were chosen such that $c_i < 1/2c_{i+1}$ [40]. Finally, the initial conditions were set as follows: $x_v(0) = 0.2$ m, $y_v(0) = 0$ m, $\alpha = 0$ rad, $\theta = 0.1$ rad, $\dot{x}_v = 0.15$ m/s, $\dot{y}_v = 0$ m/s, $\dot{\alpha} = 0$ rad/s, and $\dot{\theta} = 0.05$ rad/s.

In the first experiment, the control strategy simultaneously carries out height position by performing trajectory regulation, stabilizing the horizontal position and roll angle for the PVTOL and the pendulum angle. In this case, the desired trajectory, y_d , was proposed as

$$y_d = \frac{1}{(1 + e^{-20-2t})(1 + e^{-60+2t})}. \quad (78)$$

To test the effectiveness of the control strategy introduced in this study, we carried out a comparison test against the classical PD controller, with gains tuned as $k_p = 1$ and $k_d = 4$. Figure 4 shows the outcome of this experiment, where we can observe that both strategies successfully achieve the height position regulation through the trajectory tracking task and the stabilization of the horizontal position, the roll angle, and the pendulum angle. Also, the plot in this figure shows that our controller converges to the desired values faster than the PD controller does. Figure 5 shows the behaviours of the angular velocities, and Figure 6 shows the tracking error between α and α_d and the control inputs u_1 and u_2 .

Using the same setup as before, we run a second experiment, but in this case, the system is affected by external disturbances with parameters fixed as $a_x = 1.4$, $a_y = 0.8$, and $a_\theta = 2$. Figure 7 shows the corresponding plots, where we can see that our controller is capable of accomplishing height tracking and position regulation and, simultaneously, stabilizing the horizontal position, roll angle, and pendulum angle. Also, it can be seen that the PD controller used in the first experiment regulates the system slower than our controller does and exhibits undesirable oscillations. Therefore, our controller has better performance, maneuverability, and whole stabilization, even when the system is affected by external disturbances. Figure 8 shows the system angular velocities, and Figure 9 shows the tracking error behaviour between α and α_d and the control inputs u_1 and u_2 . Please notice that the proposed control has adequate energy management, according to the obtained performance index $\int u_i^2$ shown in Figure 10.

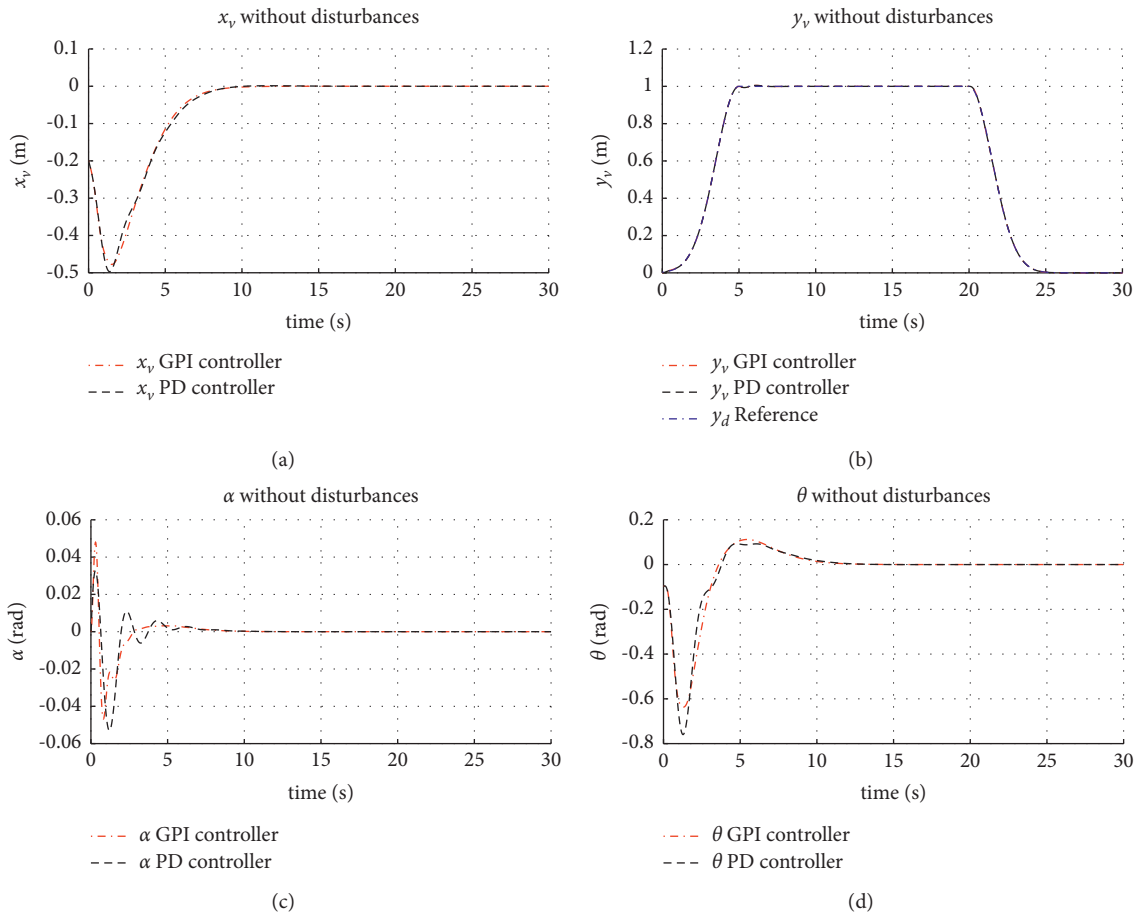


FIGURE 4: Comparison between the position closed-loop responses of the proposed controller and PD controller. (a) Behaviour of state x_v . (b) Behaviour of state y_v . (c) Behaviour of state α . (d) Behaviour of state θ .

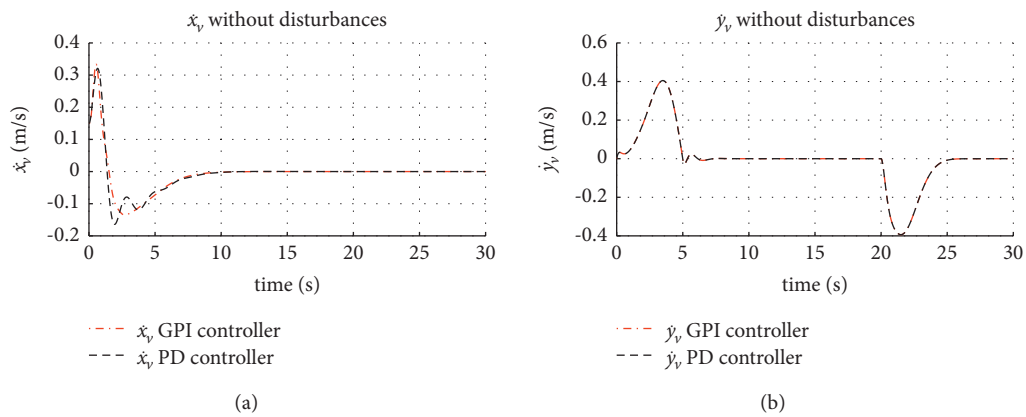


FIGURE 5: Continued.

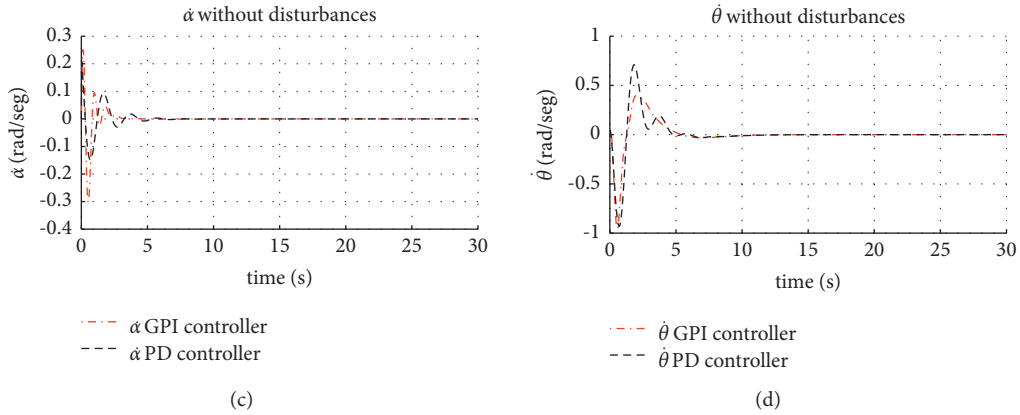


FIGURE 5: Angular velocities' closed-loop response of the proposed controller. (a) Behaviour of state \dot{x}_v . (b) Behaviour of state \dot{y}_v . (c) Behaviour of state $\dot{\alpha}$. (d) Behaviour of state $\dot{\theta}$.

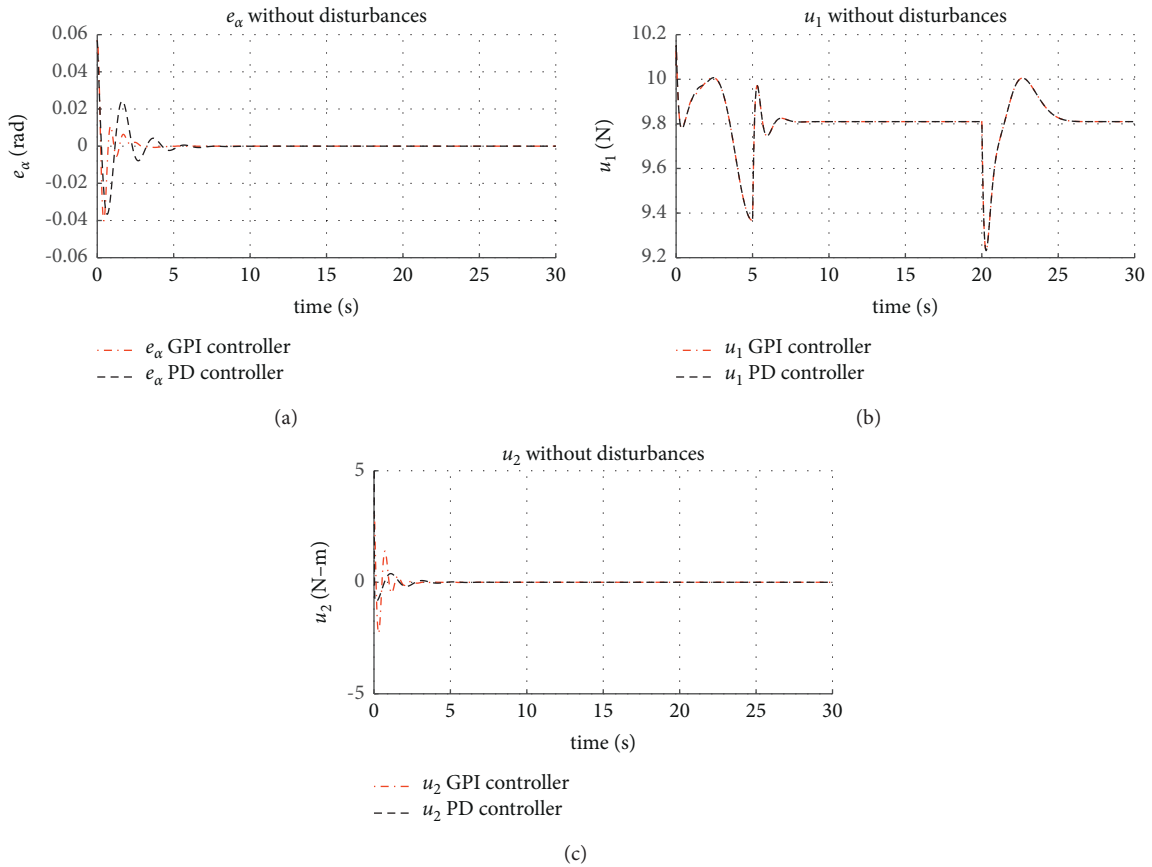


FIGURE 6: Tracking error of the state α and behavior of controllers u_1 and u_2 . (a) Error tracking dynamics for α . (b) Control action u_1 . (c) Control action u_2 .

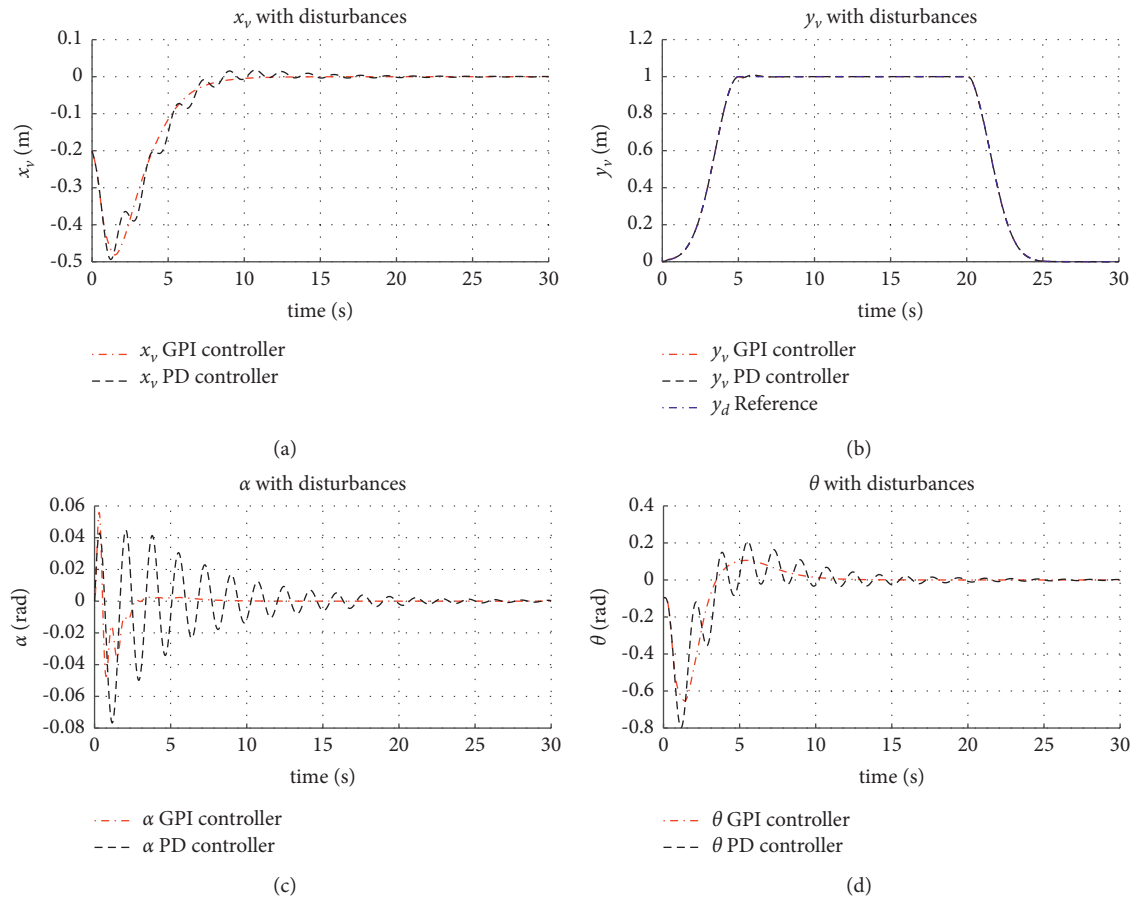


FIGURE 7: Position closed-loop response of the proposed controller in the presence of external disturbances. (a) Behaviour of state \dot{x}_v . (b) Behaviour of state \dot{y}_v . (c) Behaviour of state $\dot{\alpha}$. (d) Behaviour of state $\dot{\theta}$.

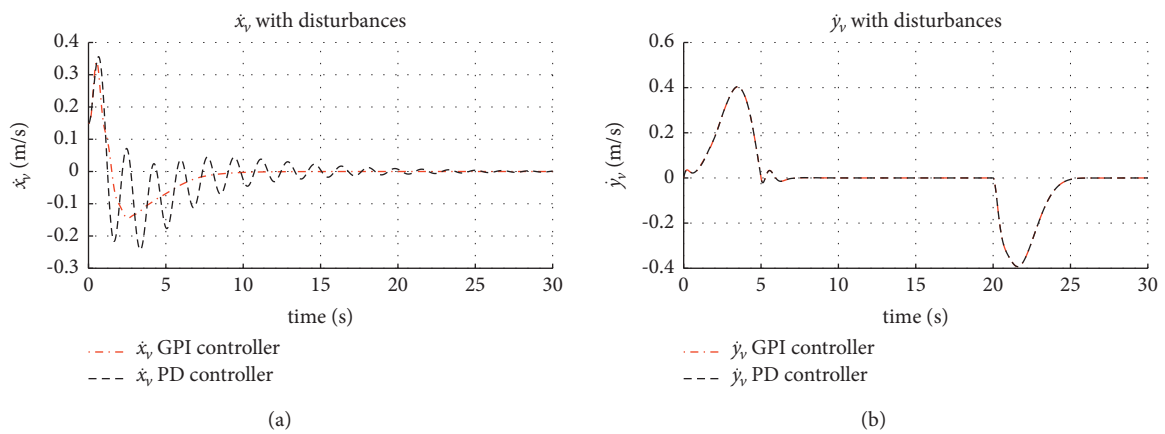


FIGURE 8: Continued.

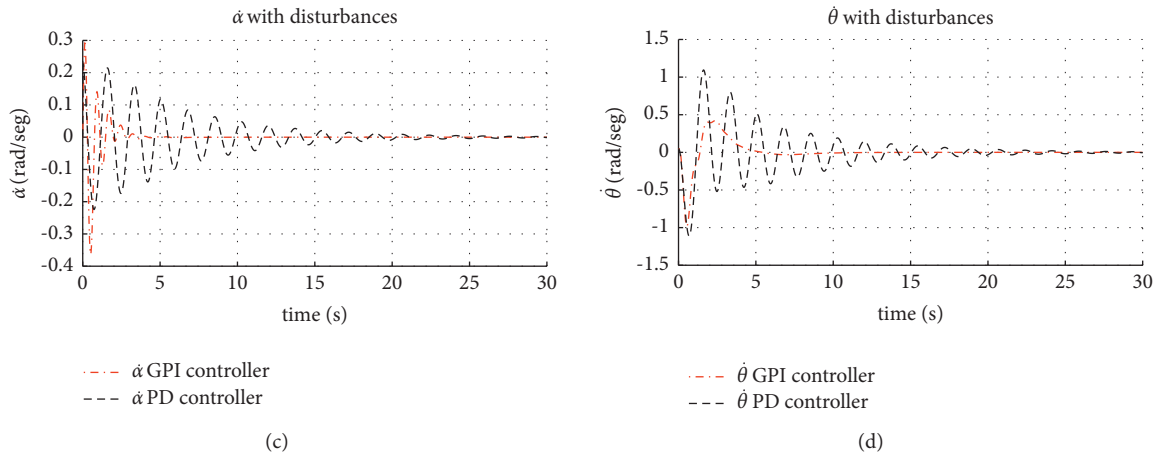


FIGURE 8: Angular velocities' closed-loop responses of the proposed controller in the presence of external disturbances. (a) Behaviour of state \dot{x}_v . (b) Behaviour of state \dot{y}_v . (c) Behaviour of state $\dot{\alpha}$. (d) Behaviour of state $\dot{\theta}$.

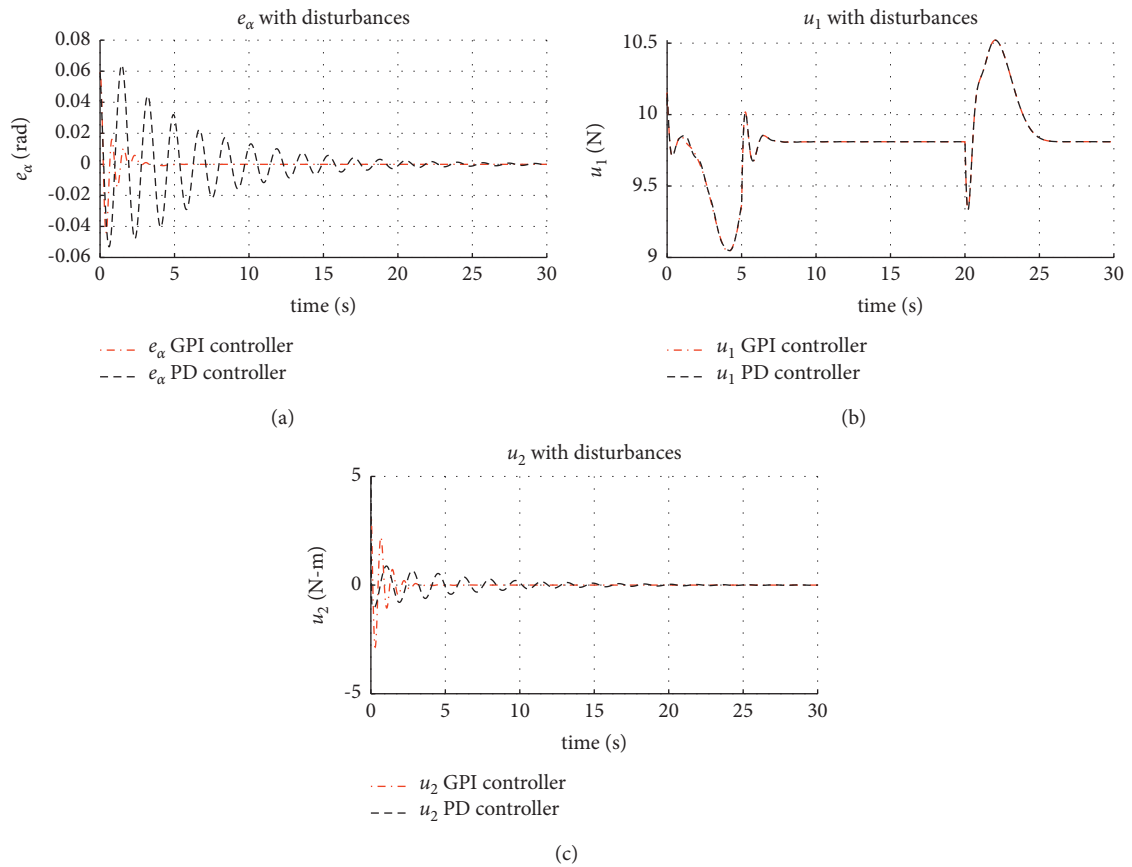


FIGURE 9: The behaviour of the error tracking of the state α and controllers u_1 and u_2 , respectively, owing to external disturbances. (a) Error tracking dynamics for α . (b) Control action u_1 . (c) Control action u_2 .

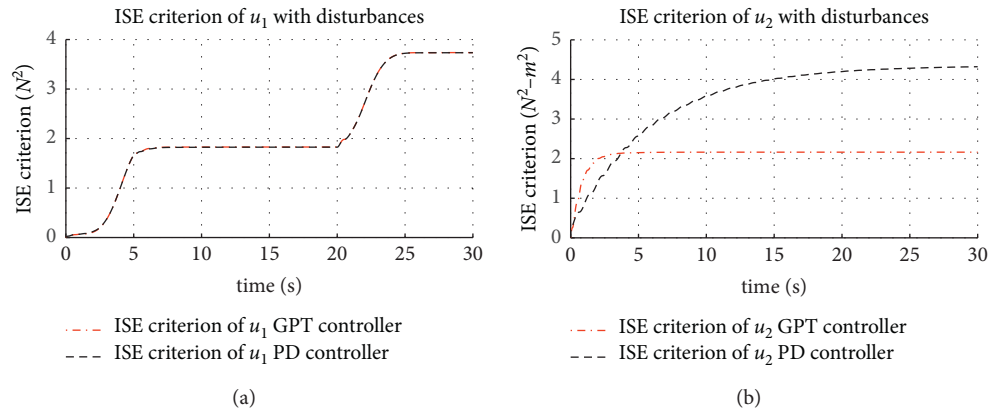


FIGURE 10: The performance index of the controllers u_1 and u_2 , respectively, owing to external disturbances. (a) Performance index of the controller u_1 . (b) Performance index of the controller u_2 .

5. Conclusions

This work presents a nested saturation function-based controller, combined with a GPI controller, to stabilize the PVTOL aircraft system with an inverted pendular load. The model of this system was derived using Euler–Lagrange formalism. The main contribution consists of using a fictitious control, and then a GPI controller is proposed for the aircraft angle (α). Several linear transformations and coordinate changes were introduced to express the original system to a minimal representation. To accomplish the takeoff and landing maneuvers, we propose a GPI controller to track the desired trajectory. After stabilizing the PVTOL height, the system was represented as a chain of integrators plus nonlinear disturbance, allowing us to use nested saturation functions to design a controller to stabilize the horizontal position and pendulum angle. The stability analysis was carried out using the second method of Lyapunov, using a simple candidate function. Designing the control scheme was not an easy task because the PVTOL system with an inverted pendular load is underactuated, and ensuring the pendulum's upright position makes this problem even harder to solve. We ran numerical simulations to assess the performance of our control scheme, having obtained convincing results. These simulations included a comparison against the well-established PD control strategy. The performance index of both controllers was computed to compare them, and the outcome revealed that our strategy has a better performance than the PD controller. It is important to note that the performance indexes were estimated in the presence of nonlinear perturbations, which means that the proposed controller behaves well even in this undesirable yet unavoidable realistic scenario. It is important to note that the controller, based on a GPI controller and nested saturation functions, allows us to perform takeoff maneuvers in the presence of exogenous disturbances.

In future work, we will explore a design to estimate the disturbance due to wind or robust techniques for parametric uncertainties of the system. In addition, it is worth mentioning that an experimental platform that allows configuring the PVTOL with an inverted pendular load system has been designed, whose construction is in process. Thus,

experimental implementation of the control scheme proposed herein is considered.

Data Availability

No data were used to support this study.

Conflicts of Interest

The authors declare that there are no conflicts of interest regarding the publication of this article.

Acknowledgments

This research was funded by Secretaria de Investigación y Posgrado-Instituto Politécnico Nacional grants nos. 20210268, 20210253, and 20211168. C. Alejandro Villaseñor Rios thanks the support from the CONACYT. Cesar Alejandro Villaseñor Rios, Octavio Gutiérrez-Frías, Carlos Aguilar-Ibanez, and Miguel S. Suarez-Castanon are at Instituto Politécnico Nacional and they are the ones to express their gratitude for the support received.

References

- [1] D. J. Block and M. W. Spong, "Mechanical design and control of the pendubot," *SAE Transactions*, pp. 36–43, 1995.
- [2] I. Fantoni and R. Lozano, "Global stabilization of the cart-pendulum system using saturation functions," *42nd IEEE International Conference on Decision and Control*, vol. 5, pp. 4393–4398, 2003.
- [3] C. A. Ibañez and O. G. Frias, "Controlling the inverted pendulum by means of a nested saturation function," *Nonlinear Dynamics*, vol. 53, no. 4, pp. 273–280, 2008.
- [4] C. Aguilar-Ibañez, M. S. Suárez-Castañón, and O. O. Gutiérrez-Frías, "The direct lyapunov method for the stabilisation of the furuta pendulum," *International Journal of Control*, vol. 83, no. 11, pp. 2285–2293, 2010.
- [5] M. Ramirez-Neria, Z. Gao, H. Sira-Ramirez, R. Garrido-Moctezuma, and A. Luviano-Juarez, "Trajectory tracking for an inverted pendulum on a cart: an active disturbance rejection control approach," in *Proceedings of the 2018 Annual American Control Conference (Acc)*, pp. 4881–4886, Milwaukee, Wisconsin, June 2018.

- [6] M. Nakamura, K. Takaya, H. Ohta, K. Shibayama, and V. Kroumov, "Quadrotor modeling and simulation for industrial application," in *Proceedings of the 2019 23rd International Conference on System Theory, Control and Computing (ICSTCC)*, pp. 37–42, Sinaia, Romania, October 2019.
- [7] S. Saeedi, C. Thibault, M. Trentini, and H. Li, "3d mapping for autonomous quadrotor aircraft," *Unmanned Systems*, vol. 5, no. 3, pp. 181–196, 2017.
- [8] A. Salih, M. Moghavvemi, H. Mohamed, and K. Gaeid, "Flight pid controller design for a uav quadrotor," *Scientific Research and Essays*, vol. 5, no. 23, pp. 3660–3667, 2010.
- [9] J. Hauser, S. Sastry, and G. Meyer, "Nonlinear control design for slightly non-minimum phase systems: application to v/stol aircraft," *Automatica*, vol. 28, no. 4, pp. 665–679, 1992.
- [10] C. Aguilar-Ibanez, M. S. Suarez-Castanon, J. Meda-Campaña, O. Gutierrez-Frias, C. Merlo-Zapata, and J. A. Martinez-Castro, "A simple approach to regulate a pvtol system using matching conditions," *Journal of Intelligent & Robotic Systems*, vol. 98, pp. 1–14, 2019.
- [11] I. Fantoni, A. Zavala, and R. Lozano, "Global stabilization of a pvtol aircraft with bounded thrust," *Proceedings of the 41st IEEE conference on decision and control*, vol. 4, pp. 4462–4467, 2002.
- [12] A. Zavala-Río, I. Fantoni, and R. Lozano, "Global stabilization of a pvtol aircraft model with bounded inputs," *International Journal of Control*, vol. 76, no. 18, pp. 1833–1844, 2003.
- [13] L. Zou, H. Li, W. Zhao, and L. Zhu, "Imaged-based visual servo control for a Vtol aircraft," *Mathematical Problems in Engineering*, vol. 2017, Article ID 4806769, 6 pages, 2017.
- [14] R. Czyba, M. Lemanowicz, Z. Gorol, and T. Kudala, "Construction prototyping, flight dynamics modeling, and aerodynamic analysis of hybrid vtol unmanned aircraft," *Journal of Advanced Transportation*, vol. 2018, Article ID 7040531, 17 pages, 2018.
- [15] L. Wang and J. Cheng, "Finite-time terminal sliding mode tracking control of a vtol uav via the generalized ndob," *Mathematical Problems in Engineering*, vol. 2020, Article ID 4651475, 13 pages, 2020.
- [16] M. Hehn and R. D'Andrea, "A flying inverted pendulum," in *Proceedings of the 2011 IEEE International Conference on Robotics and Automation*, pp. 763–770, Shanghai, China, May 2011.
- [17] R. Figueroa, A. Faust, P. Cruz, L. Tapia, and R. Fierro, "Reinforcement learning for balancing a flying inverted pendulum," in *Proceedings of the 11th World Congress on Intelligent Control and Automation*, pp. 1787–1793, Shenyang, China, June 2014.
- [18] D. S. Maughan, I. Erekson, and R. Sharma, "Using extended kalman filter for robust control of a flying inverted pendulum," in *Proceedings of the 2015 IEEE Signal Processing and Signal Processing Education Workshop (sp/spe)*, pp. 101–106, Snowbird, UT, USA, August 2015.
- [19] D. S. Maughan, I. T. Erekson, and R. Sharma, "Flying inverted pendulum trajectory control on robust intelligent sensing and control multi-agent analysis platform," in *Proceedings of the 2015 International Conference on Unmanned Aircraft Systems (ICUAS)*, pp. 1279–1284, Denver, CO, USA, June 2015.
- [20] C. Zhang, H. Hu, D. Gu, and J. Wang, "Cascaded control for balancing an inverted pendulum on a flying quadrotor," *Robotica*, vol. 35, no. 6, pp. 1263–1279, 2017.
- [21] M. M. Nicotra, E. Garone, R. Naldi, and L. Marconi, "Nested saturation control of an uav carrying a suspended load," in *Proceedings of the 2014 American Control Conference*, pp. 3585–3590, Portland, OG, USA, June 2014.
- [22] I. H. Pizetta, A. Brandão, and M. Sarcinelli-Filho, "Modelling and control of a pvtol quadrotor carrying a suspended load," in *Proceedings of the 2015 International Conference on Unmanned Aircraft Systems (ICUAS)*, pp. 444–450, Denver, CO, USA, June 2015.
- [23] C. Merlo-Zapata, C. Aguilar-Ibanez, O. Gutiérrez-Frias, M. Antonio-Cruz, C. Márquez-Sánchez, and M. Suarez-Castanon, "A robust control scheme for a pvtol system subject to wind disturbances," *Complexity*, vol. 2020, Article ID 3510396, 11 pages, 2020.
- [24] A. Moeini, A. F. Lynch, and Q. Zhao, "A backstepping disturbance observer control for multirotor uavs: theory and experiment," *International Journal of Control*, vol. 21, pp. 1–15, 2021.
- [25] B. Chen, C. Lin, X. Liu, and K. Liu, "Adaptive fuzzy tracking control for a class of mimo nonlinear systems in nonstrict-feedback form," *IEEE Transactions on Cybernetics*, vol. 45, no. 12, pp. 2744–2755, 2014.
- [26] M. A. Jaradat, M. Al-Fandi, O. Alkhatib, and Y. Sardahi, "Intelligent control of miniature holonomic vertical take-off and landing robot," *Journal of Intelligent & Fuzzy Systems*, vol. 29, no. 3, pp. 1209–1217, 2015.
- [27] S. C. Tong, "Adaptive fuzzy control for uncertain nonlinear systems," *Journal of Control and Decision*, vol. 6, no. 1, pp. 30–40, 2019.
- [28] C. Aguilar-Ibanez, H. Sira-Ramirez, M. Suarez-Castanon, and R. Garrido, "Robust trajectory-tracking control of a pvtol under crosswind," *Asian Journal of Control*, vol. 21, no. 3, pp. 1293–1306, 2019.
- [29] Q. Yao, "Robust constrained trajectory tracking control for a pvtol aircraft subject to external disturbances," *International Journal of Systems Science*, vol. 52, pp. 1–13, 2021.
- [30] S. Bouabdallah, "Design and control of quadrotors with application to autonomous flying," Technical Report, Epfl, Lausanne, Switzerland, 2007.
- [31] Y. Lozano Hernández, O. Gutiérrez Frías, N. Lozada-Castillo, and A. Luviano Juárez, "Control algorithm for taking off and landing manoeuvres of quadrotors in open navigation environments," *International Journal of Control, Automation and Systems*, vol. 17, no. 9, pp. 2331–2342, 2019.
- [32] M. Fliess, R. Marquez, and E. Delaleau, "State feedbacks without asymptotic observers and generalized pid regulators," in *Nonlinear Control in the Year 2000*, pp. 367–384, Springer, Berlin, Germany, 2001.
- [33] B. R. Angara and M. Tripathi, "Design of gpi controller for current feedback multilevel cascaded inverter," in *Proceedings of the 2016 Biennial International Conference on Power and Energy Systems: Towards Sustainable Energy (PESTSE)*, pp. 1–5, Bangalore, India, January 2016.
- [34] H. Sira-Ramírez, A. Luviano-Juárez, M. Ramírez-Neria, and E. W. Zurita-Bustamante, *Active Disturbance Rejection Control of Dynamic Systems: A Flatness Based Approach*, Butterworth-Heinemann, Oxford, UK, 2018.
- [35] C. Aguilar Ibanez, O. Gutiérrez Frías, and M. S. Suarez Castanon, "Controlling the strongly damping inertia wheel pendulum via nested saturation functions," *Computación Y Sistemas*, vol. 12, no. 4, pp. 436–449, 2009.
- [36] C. Aguilar Ibanez, J. C. Martinez Garcia, A. Soria Lopez, J. d. J. Rubio, and M. S. Suarez Castanon, "Stabilization of the inverted cart-pendulum system with linear friction," *IEEE Latin America Transactions*, vol. 16, no. 6, pp. 1650–1657, 2018.
- [37] P. Castillo, A. Dzul, and R. Lozano, "Real-time stabilization and tracking of a four-rotor mini rotorcraft," *IEEE*

- Transactions on Control Systems Technology*, vol. 12, no. 4, pp. 510–516, 2004.
- [38] C. Aguilar-Ibañez, J. C. Martínez-García, A. Soria-López, and J. Rubio, “On the stabilization of the inverted-cart pendulum using the saturation function approach,” *Mathematical Problems in Engineering*, vol. 2011, Article ID 856015, 14 pages, 2011.
- [39] R. Olfati-Saber, “Fixed point controllers and stabilization of the cart-pole system and the rotating pendulum,” in *Proceedings of the 38th IEEE Conference on Decision and Control*, pp. 1174–1181, Phoenix, AZ, USA, December 1999.
- [40] A. R. Teel, “Global stabilization and restricted tracking for multiple integrators with bounded controls,” *Systems & Control Letters*, vol. 18, no. 3, pp. 165–171, 1992.

Research Article

Analysis of Dynamic Characteristics of Tristable Piezoelectric Energy Harvester Based on the Modified Model

Dawei Man,^{1,2} Deheng Xu,¹ Xingchen Kuang,³ Xiaofang Kang ,^{1,2} Qinghu Xu,^{1,2} and Yu Zhang⁴

¹School of Civil Engineering, Anhui Jianzhu University, Hefei 230601, China

²BIM Engineering Center of Anhui Province, Hefei 230601, China

³School of Civil and Hydraulic Engineering, Hefei University of Technology, Hefei 230009, China

⁴School of Engineering, Anhui Agricultural University, Hefei 230036, China

Correspondence should be addressed to Xiaofang Kang; xiaofangkang@ahjzu.edu.cn

Received 24 July 2021; Accepted 1 October 2021; Published 22 October 2021

Academic Editor: Raúl Villafuerte-Segura

Copyright © 2021 Dawei Man et al. This is an open access article distributed under the Creative Commons Attribution License, which permits unrestricted use, distribution, and reproduction in any medium, provided the original work is properly cited.

Taking into account the gravitational potential energy of the piezoelectric energy harvester, the size effect, and the rotary inertia of tip magnet, a more accurate distributed parametric electromechanical coupling equation of tristable cantilever piezoelectric energy harvester is established by using the generalized Hamilton variational principle. The effects of magnet spacing, the mass of tip magnet, the thickness ratio of piezoelectric layer and substrate, and the load resistance and piezoelectric material on the performance of piezoelectric energy capture system are studied by using multiscale method. The results show that the potential well depth can be changed by reasonably adjusting the magnet spacing, so as to improve the energy capture efficiency of the system. Increasing the mass of tip magnet can enhance the output power and frequency bandwidth of the interwell motion. When the thickness of the piezoelectric beam remains unchanged, the optimal load impedance of the system increases along with the increase of thickness ratio of piezoelectric layer and substrate. Compared with the traditional model, which neglects the system gravitational potential energy, the eccentricity, and the rotary inertia of the tip magnet, the calculation results of the frequency bandwidth and the peak power of the modified model have significantly increased.

1. Introduction

The extensive application of wireless sensors in building structural health monitoring, environmental monitoring, and military fields has put forward higher requirements for the cleanliness and sustainability of the power supply. The piezoelectric energy harvester (PEH) can collect vibration energy in the surrounding environment and convert it into sustainable and clean electricity. Due to its simple structure and compact and easy integration, it has great potential to implement wireless sensor nodes and has received extensive attention in recent years [1–4]. The primary structure of the PEH initially is a linear resonator that mainly consists of a piezoelectric cantilever beam with a tip mass. Such linear PEH has a narrow frequency bandwidth that can achieve a peak value only when the external excitation frequency is in

agreement with its resonant frequency [5–7]. This makes such linear PEH difficult to meet the requirements of the practical application [8, 9]. To make it more applicable, a variety of complex energy capture systems with active or adaptive techniques have been developed. Among these techniques, nonlinear techniques have been proved to be more suitable for energy harvesting from ambient vibrations in practical applications due to the less sensitivity to variations in the excited frequency of the realistic operational conditions [10,11].

The nonlinearity of the PEHs caused by the magnetic force can be generally classified into three main categories, namely, monostable [12, 13], bistable [14–17], and tristable [18–20] PEHs. Bistable piezoelectric energy harvester (BPEH) has two symmetric potential wells and can oscillate between these two potential wells under low-frequency external

excitations, which can greatly enhance the power outputs. Stanton et al. [21] established the distribution parameter model of the cantilever BPEH. Based on the harmonic balance method, the analytical expression of the steady-state response of the energy capture system is obtained and its working characteristics are analyzed. Tang et al. [22] investigated the voltage output of a bistable cantilever piezoelectric energy harvesting system under different excitations and analyzed the influence of magnet spacing on the system response. Kim et al. [23] proposed an electromechanical coupling equation for a hysteresis reversible cantilever-type magnetoelastic BPEH. Wang et al. [24] designed an asymmetric bistable piezoelectric energy harvester composed of a piezoelectric cantilever beam and rotatable magnets and further proposed a method for compensating asymmetric potential wells by appropriately changing the magnet's declination angle. These investigations have shown that the working bandwidth and output power of the BPEH can be greatly improved after oscillating into an interwell motion. However, when the external excitation is low, it is difficult for the BPEH to get rid of the confinement of the potential well and move into the large interwell motion.

In order to overcome this challenge and to produce high energy output at low excitation intensity, tristable piezoelectric energy harvesters (TPEHs) are proposed. Zhu et al. [25] established a TPEH based on the magnetic bistable piezoelectric cantilever beam model, when the angle and distance between two fixed magnets are appropriate, the potential energy function of the energy capture system presents a three-steady state and the potential barrier decreases. Numerical simulation and experimental results show that the TPEH can generate higher output power than the bistable piezoelectric energy harvester in a wider frequency range under lower excitation intensity. Li et al. [26] analyzed a tristable energy harvester which can obtain a high harvesting efficiency at low-frequency base excitation by tristable coherence resonance. Panyam et al. [27] theoretically and experimentally studied the influence of the electromechanical coupling coefficient on the effective bandwidth of the TPEH. Kim et al. [28] proposed potential energy diagrams and found that the tristability of the TPEH is initiated by a new pitchfork bifurcation or a degenerate pitchfork bifurcation that leads to a pair of saddle-node bifurcations. Leng et al. [29] obtained a more precise magnetic force model for the TPEH using equivalent magnetizing current method and the calculation results of magnetic force are in good agreement with experimental data. Yang et al. [18,19] investigated the energy harvesting of the tristable hybrid vibration energy harvester by using geometric nonlinearity to tune the resonant frequency.

In this paper, considering the gravitational potential energy of the system, the eccentricity, and rotary inertia of the tip magnet, a more accurate nonlinear three-steady-state distribution parameter model of the piezoelectric cantilever energy harvester is established based on the generalized Hamilton variational principle, and the analytic solution of the motion equation of the system is obtained by using the multiscale method. In the magnetic dipole model, the influence of eccentricity of the tip magnet is taken into account

and the magnetic potential energy expressed by polynomial is obtained. The effects of the distance between the magnets, the mass of the tip magnet, the load resistance, the thickness ratio of the piezoelectric layer to the substrate layer, and the piezoelectric materials on the performance of the energy capture system were studied.

2. Theoretical Model of the TPEH

Figure 1 shows the configuration of the TPEH with magnetic coupling considered in this paper. It mainly consists of a piezoelectric cantilever beam and three magnets (denoted as A, B, and C). The piezoelectric cantilever beam is fixed at the base and is composed of a metal substrate and a pair of piezoelectric layers (PZTs). Two identical PZTs, poled oppositely in the thickness direction, are tightly bonded on the upper and lower surfaces of the substrate. The two PZTs are electrically connected in series with an equivalent load resistance (R) represented as a low power electronic device. Magnet A (named tip magnet) is attached at the tip of the cantilever beam and two external magnets (B and C) are fixed at the frame. The horizontal gap between the tip magnet and magnets B and C is d_h . The vertical gap between magnet B and magnet C is $2d_v$. Here, l and b denote the length and width of the piezoelectric cantilever beam, respectively; h_s and t_p denote the thickness of the metal substrate and the PZTs, respectively; e is the eccentricity of the tip magnet.

$v_b(t)$ represents the vibration displacement of the base, and s is the coordinate along the neutral axis of the piezoelectric cantilever beam. $v(s, t)$ represents the displacement of the beam at s relative to its fixed end. The modeling of the PEH is based on the linear Euler-Bernoulli beam theory and the linear constitutive equations of the piezoelectric beam are assumed as follows:

$$\left. \begin{aligned} T_1^s &= Y_s S_1^s \\ T_1^p &= Y_p (S_1^p - d_{31} E_3) \\ D_3 &= d_{31} T_1 + \epsilon_{33}^T E_3 \end{aligned} \right\}, \quad (1)$$

where Y is Young's modulus, subscript/superscript p and s represent the piezoelectric layers and substrate layer, S_1 and T_1 are the strain and the stress of the piezoelectric cantilever beam, respectively. 1 and 3 indicate x and y directions, D_3 is the electric displacement, d_{31} is the piezoelectric constant, and ϵ_{33}^T is the dielectric constant. E_3 is the electric field.

The strain generated in the piezoelectric cantilever beam can be expressed as

$$E_3 = -\frac{V(t)}{(2t_p)}, \quad (2)$$

$$S_1^s = S_1^p = -yv''. \quad (3)$$

The Lagrange function of the piezoelectric energy harvesting system is as follows:

$$L = T_k + W_e - U_e - U_g - U_m, \quad (4)$$

where T_k is the kinetic energy, U_e is the potential energy, W_e is the electrical energy, U_g is the gravitational potential

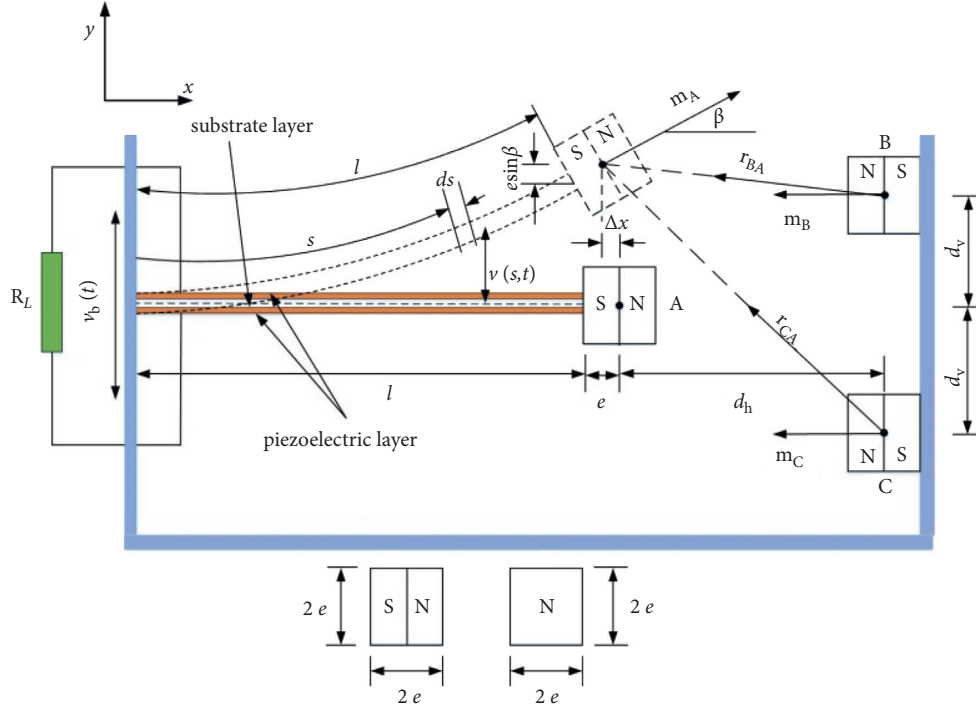


FIGURE 1: Schematic of the considered TPEH.

energy, and U_m is the magnetic potential energy. T_k and W_e are as follows:

$$T_k = \frac{1}{2} \int_0^l m (\dot{v} + \dot{v}_b(t))^2 ds + \frac{1}{2} M_t \cdot (\dot{v}(l, t) + e\dot{v}'(l, t) + \dot{v}_b(t))^2 + \frac{1}{2} J \dot{v}'(l, t)^2, \quad (5)$$

$$W_e = \frac{1}{2} Y_p b d_{31} \left(h + \frac{t_p}{2} \right) V(t) \int_0^l v'' ds + b l \epsilon_{33}^s \frac{V(t)^2}{4t_p},$$

where $m = 2\rho_p t_p b + \rho_s h_s b$, in which ρ_p and ρ_s are the density of the piezoelectric layers and substrate layer, respectively. M_t and J are mass and the rotary inertia of the tip mass, respectively. ϵ_{33}^s is the permittivity at constant strain.

U_e is expressed as

$$U_e = \frac{1}{2} \int_0^l \left\{ YI v''^2 - Y_p b d_{31} \left(h + \frac{t_p}{2} \right) V(t) v'' \right\} ds, \quad (6)$$

where $h = h_s/2$, $YI = (2/3)[Y_s b h^3 + Y_p b (3h^2 t_p + 3ht_p^2 + t_p^3)]$.

U_g can be expressed as

$$U_g = mg \int_0^l (v + v_b(t)) ds + M_t g (v(l, t) + v_b(t)). \quad (7)$$

According to the magnetic dipole model [25] and considering the eccentricity of the tip magnet, the magnetic potential energy can be given by

$$U_m = \frac{\mu_0}{4\pi} \left[\frac{\mathbf{m}_B}{\|\mathbf{r}_{BA}\|^3} + \frac{\mathbf{m}_C}{\|\mathbf{r}_{CA}\|^3} - \frac{(\mathbf{m}_B \cdot \mathbf{r}_{BA}) 3\mathbf{r}_{BA}}{\|\mathbf{r}_{BA}\|^5} - \frac{(\mathbf{m}_C \cdot \mathbf{r}_{CA}) 3\mathbf{r}_{CA}}{\|\mathbf{r}_{CA}\|^5} \right] \cdot \mathbf{m}_A, \quad (8)$$

where $\mu_0 = 4\pi \times 10^{-7} \text{H} \cdot \text{m}^{-1}$ is the magnetic permeability constant. As shown in Figure 1, the horizontal displacement can be evaluated by $\Delta x \approx e(1 - \cos \beta)$, where $\beta = \arctan v'(l)$ is the rotation angle of the tip magnet A. $\mathbf{r}_{BA} = [-d_h - \Delta x, v(l, t) + e \sin \beta - d_v]$ and $\mathbf{r}_{CA} = [-d_h - \Delta x, v(l, t) + e \sin \beta + d_v]$ are the vector directed from the magnetic moment source of magnet B and C to that of magnet C, respectively.

$\mathbf{m}_A = [M_A V_A \cos \beta, M_A V_A \sin \beta]$, $\mathbf{m}_B = [-M_B V_B, 0]$ and $\mathbf{m}_C = [-M_C V_C, 0]$ represent the magnetic moment vectors of magnet A, B, and C, respectively, where M_A (M_B or M_C) and V_A (V_B or V_C) are the magnetization intensity and material volume of the magnet A (B or C), respectively.

Using the Galerkin approach, the displacement $v(s, t)$ is assumed as the following form:

$$v(s, t) = \varphi_r(s) \eta_r(t), \quad (9)$$

where $\varphi_r(s)$ and $\eta_r(t)$ are the R-order mode shape function and the generalized mode coordinates of the cantilever beam, respectively.

The modal shape function satisfies the following orthogonal relations:

$$\int_0^l \varphi_s(s) m \varphi_r(s) ds + \varphi_s(l) M_t \varphi_r(l) + \varphi_s(l) M_t e \varphi_r'(l) + \varphi_s'(l) (J + M_t e^2) \varphi_r'(l) + \varphi_s'(l) M_t e \varphi_r(l) = \delta_{rs}, \quad (10)$$

$$\int_0^l \frac{d^2 \varphi_s(s)}{ds^2} YI \frac{d^2 \varphi_r(s)}{ds^2} ds = \omega_r^2 \delta_{rs}, \quad (11)$$

where δ_{rs} is the Kronecker delta, $\omega_r = \lambda_r^2 \sqrt{YI/(m l^4)}$ represents the resonance frequency of the r -th mode, and λ_r is

the eigenvalue. The calculation of the oscillation function and eigenvalues is described in the literature [6].

Substituting equation (9) into (8) and considering only the 1st order mode, Taylor's expansion of U_m at $\eta(t) = 0$ can be written as

$$k_1 = \frac{4\kappa}{(d_h^2 + d_v^2)^{5/2}} [q_1(2.5q_2 - 17.5q_3^2) - 5q_3q_4(d_h^2 + d_v^2) - q_5]$$

$$k_2 = \frac{8\kappa}{(d_h^2 + d_v^2)^{5/2}} [(q_1 - 2.5q_6 - 17.5q_3q_7 + 4.38q_2^2 - 78.75q_2q_3^2 + 144.375q_3^4) + q_4(-2.5q_7 - 17.5q_2q_3 + 52.5q_3^3)](d_h^2 + d_v^2) \\ [+q_5(-2.5q_2 + 17.5q_3^2) + 5q_3q_8 + q_9]$$

$$k_3 = \frac{12\kappa}{(d_h^2 + d_v^2)^{5/2}} [(q_1 - 2.5q_{10} + 13.125q_3q_{11} + 8.75q_2q_6 + 4.375q_7^2 - 78.75q_3^2q_6 + 78.25q_2q_3q_7 - 288.75q_3^3q_7 + 216.55q_2^2q_3^2 \\ - 6.56q_3^2 - 938.44q_2q_3^4 + 938.44q_2^6) + q_4(1.875q_{11} - 17.5q_3q_6 + 8.75q_2q_7 - 78.75q_3^2q_7 + 39.38q_2^2q_3 - 288.75q_2q_3^2 + 375.375q_3^5) \\ + (q_5 - 2.5q_6 - 17.5q_3q_7 + 4.375q_2^2 - 78.75q_2q_3^2 + 144.375q_3^4) \\ + q_8(-2.5q_7 - 17.5q_2q_3 + 52.5q_3^3) + q_9(-2.5q_2 + 17.5q_3^2 + 5q_3q_{12} + q_{13})]. \quad (13)$$

Expressions for the coefficients κ and $q_{i=1...13}$ are shown in the appendix.

Considering only the 1st order mode, equation (2) is substituted into the following Lagrangian variational equation using equation (9).

$$\begin{cases} \frac{d}{dt} \left(\frac{\partial L}{\partial \dot{\eta}} \right) - \frac{\partial L}{\partial \eta} = F(t), \\ \frac{d}{dt} \left(\frac{\partial L}{\partial \dot{V}} \right) - \frac{\partial L}{\partial V} = Q(t), \end{cases} \quad (14)$$

where $F_1(t) = -2\xi_1\omega_1\dot{\eta}_1(t)$ is the generalized dissipative force, ω_1 denotes the 1st order resonance frequency, ξ_1 is the damping ratio, and $Q(t)$ represents the generalized output charge. $Q(t) = V(t)/R$, where R denotes the load impedance. The electromechanical coupling equations of the piezoelectric beam energy harvesting system can be obtained by using equation (13):

$$\ddot{\eta}_1 + 2\xi_1\omega_1\dot{\eta}_1 + \omega_1^2\eta_1 + g_0 - k_1\eta_1 \quad (15)$$

$$+ k_2\eta_1^3 + k_3\eta_1^5 - \theta_1 V(t) = -\Gamma_1 v_b(t),$$

$$C_p \dot{V}(t) + \frac{V(t)}{R} + \theta_1 \dot{\eta}_1 = 0, \quad (16)$$

where $\omega_1^2 = YI \int_0^l \varphi_1'' ds$, $g_0 = mg \int_0^l \varphi_1(s) ds + M_t g \varphi_1(l)$, $\Gamma_1 = m \int_0^l \varphi_1(s) ds + M_t(\varphi_1(l) + e\varphi_1'(l))$, $\theta_1 = Y_p b d_{31}(h + (t_p/2)) \int_0^l \varphi_1'' ds$, and $C_p = bl\epsilon_{33}^s/2t_p$.

$$U_m = k_0 - \frac{1}{2}k_1\eta_1^2 + \frac{1}{4}k_2\eta_1^4 + \frac{1}{6}k_3\eta_1^6 + o(\eta_1^7), \quad (12)$$

where, $k_0 = 2\kappa q_1/(d_h^2 + d_v^2)^2$,

Assume that the excitation acceleration is $\ddot{v}_b(t) = \bar{v}_b \cos(\omega_e t)$, where \bar{v}_b denotes the amplitude of the excitation, ω_e denotes the circular frequency, and C_p denotes the capacitance. Introducing the dimensionless parameters shown in equation (17), the electromechanical coupling equations (14) and (16) can be rewritten as equations (18) and (19) in the dimensionless form.

$$x = \frac{\eta_1}{l},$$

$$\bar{V} = \frac{VC_p}{l\theta_1}, \quad (17)$$

$$\tau = \omega_1 t,$$

$$x + 2\xi_1 \dot{x} + G_0 + (1 - K_1)x + K_2 x^3 \\ + K_3 x^5 - \Theta \bar{V} = f \cos(\omega \tau), \quad (18)$$

$$\dot{\bar{V}} + \alpha \bar{V} + \dot{x} = 0, \quad (19)$$

where $G_0 = G_0/(\omega_1^2 l)$, $K_1 = k_1/\omega_1^2$, $K_2 = k_2 l^2/\omega_1^2$, $K_3 = k_3 l^4/\omega_1^2$, $\Theta = \theta_1^2/C_p \omega_1^2$, $f = -\Gamma_1 \bar{v}_b/\omega_1^2 l$, and $\omega = \omega_e/\omega_1$, $\alpha = 1/C_p R \omega_1$.

3. Multiscale Method Analysis

The total potential energy function of the system can be expressed as

$$U = G_0 x + \frac{1}{2}(1 - K_1)x^2 + \frac{1}{4}K_2 x^4 + \frac{1}{6}K_3 x^6. \quad (20)$$

Figure 2 shows the potential energy curve of the system at different magnet spacing. For the traditional model ($G_0 = 0$), when $1 - K_1 > 0$, $K_2 < 0$, $K_3 > 0$ and $K_2^2 - 4(1 - K_1)K_3 > 0$, the two symmetric potential wells associated with the equilibria at $x_s = \mp \sqrt{(-K_2 + \sqrt{K_2^2 - 4(1 - K_1)K_3})/(2K_3)}$ are separated by the potential well associated with the trivial equilibrium, $x_s = 0$. In this scenario, the potential energy function is symmetrically tristable. With the increase of d_v , the middle potential well depth increases while the outer potential well depth decreases when d_h remains constant. When the d_v is constant, the middle and outer middle potential well depths decrease with the increase of d_h . When the modified model ($G_0 \neq 0$) is used, the potential energy curve will no longer be symmetric, but the variation pattern of potential well depth with magnet spacing is consistent with that of the conventional model.

Introducing a small perturbation parameter ε , a new independent time variable T_n can be expressed as

$$T_n = \varepsilon^n \tau. \quad (21)$$

The derivative with respect to τ is

$$\frac{d}{d\tau} = \sum_{n=0}^m \varepsilon^n D_n. \quad (22)$$

The displacement and output voltage response of the system can be respectively expressed as

$$\begin{cases} x(\tau, \varepsilon) = \sum_{n=0}^m \varepsilon^n x_n(T_0, T_1, \dots, T_n), \\ \bar{V}(\tau, \varepsilon) = \sum_{n=0}^m \varepsilon^n \bar{V}_n(T_0, T_1, \dots, T_n). \end{cases} \quad (23)$$

The constant parameters such as nonlinear term coefficients, electromechanical coupling coefficients, and the excitation forcing in equation (18) are scaled so that the viscous damping effect appears at the same order of the perturbation problem. That is, we let

$$\begin{aligned} \xi_1 &= \varepsilon \bar{\xi}_1, \\ K_2 &= \varepsilon \bar{K}_2, \\ K_3 &= \varepsilon \bar{K}_3, \\ \Theta &= \varepsilon \bar{\Theta}, \\ f &= \varepsilon \bar{f}. \end{aligned} \quad (24)$$

Substituting equation (24) into equation (18), we get

$$x + \bar{\omega}_1^2 x + G_0 + \varepsilon [2\bar{\xi}_1 \dot{x} + \bar{K}_2 x^3 + \bar{K}_3 x^5 - \bar{\Theta} \bar{V}] = \varepsilon \bar{f} \cos(\omega \tau), \quad (25)$$

where $\bar{\omega}_1 = \sqrt{1 - \bar{K}_1}$ represents the linearized oscillation frequency within the middle potential well.

To express the nearness of the excitation frequency to the linearized resonance frequency within the middle potential well, we let

$$\omega^2 = \bar{\omega}_1^2 + \varepsilon \sigma. \quad (26)$$

Substituting equations (22)–(26) into equation (25) and truncating at order ε and separating the terms of ε and equating them to zero, we obtain

$$O(\varepsilon^0): D_0^2 x_0 + \omega^2 x_0 = -G_0, \quad (27a)$$

$$D_0 \bar{V}_0 + \alpha \bar{V}_0 = -D_0 x_0, \quad (27b)$$

$$\begin{aligned} O(\varepsilon^1): D_0^2 x_1 + \omega^2 x_1 &= -2D_0 D_1 x_0 - 2\bar{\xi}_1 D_0 x_0 - \bar{K}_2 x_0^3 \\ &\quad - \bar{K}_3 x_0^5 + \sigma x_0 + \bar{\Theta} \bar{V}_0 + \bar{f} \cos(\omega \tau), \end{aligned} \quad (28a)$$

$$D_0 \bar{V}_1 + \alpha \bar{V}_1 = -D_0 x_1 - D_1 x_0 - D_1 \bar{V}_0. \quad (28b)$$

The solutions of equations (27a) and (27b) can be written as

$$x_0 = A(T_1) \exp(i\omega T_0) - \frac{G_0}{\omega^2} + cc, \quad (29)$$

$$\bar{V}_0 = -\frac{\omega^2 + i\omega\alpha}{\alpha^2 + \omega^2} A(T_1) \exp(i\omega T_0) + cc, \quad (30)$$

where $A(T_1)$ is a complex-valued function, \bar{A} is the complex conjugate of A , and cc is the complex conjugate of the preceding term. Substituting equations (29) and (30) into equation (28a) and eliminating the secular terms, we get

$$\begin{aligned} &-2i\omega D_1 A - 2i\omega \bar{\xi}_1 A - \frac{\omega^2 + i\omega\alpha}{\alpha^2 + \omega^2} \bar{\Theta} A - 3\left(\frac{G_0}{\omega^2}\right)^2 \bar{K}_2 A \\ &- 5\left(\frac{G_0}{\omega^2}\right)^4 \bar{K}_3 A - 3\bar{K}_2 A^2 \bar{A} - 30\left(\frac{G_0}{\omega^2}\right)^2 \bar{K}_3 A^2 \bar{A} \\ &- 10\bar{K}_3 A^3 \bar{A}^2 + \sigma A + \frac{\bar{f}}{2} \exp(i\sigma T_1) = 0. \end{aligned} \quad (31)$$

A can be expressed in the polar form $A = 1/2ae^{i\theta}$, where a represents the steady-state displacement response amplitude and θ is the argument. Introducing $\gamma = \sigma T_1 - \theta$, substituting it into equation (29) and then separating the real and imaginary parts, we obtain

$$D_1 a = -c_1 a + c_2 \sin \gamma, \quad (32a)$$

$$a D_1 \gamma = c_3 a - c_4 a^3 - c_5 a^5 + c_2 \cos \gamma. \quad (32b)$$

where $c_1 = \bar{\xi}_1 + \alpha \bar{\Theta}/2(\omega^2 + \alpha^2)$, $c_2 = \bar{f}/2\omega$, $c_3 = \sigma + (\sigma/2\omega) - (\bar{\Theta}\omega/2(\omega^2 + \alpha^2)) - (3\bar{K}_2/2\omega)(G_0/\omega^2)^2 - (5\bar{K}_3/2\omega)(G_0/\omega^2)^4$, $c_4 = (3\bar{K}_2/8\omega) + (15\bar{K}_3/4\omega)(G_0/\omega^2)^2$, and $c_5 = (5\bar{K}_3/16\omega)$.

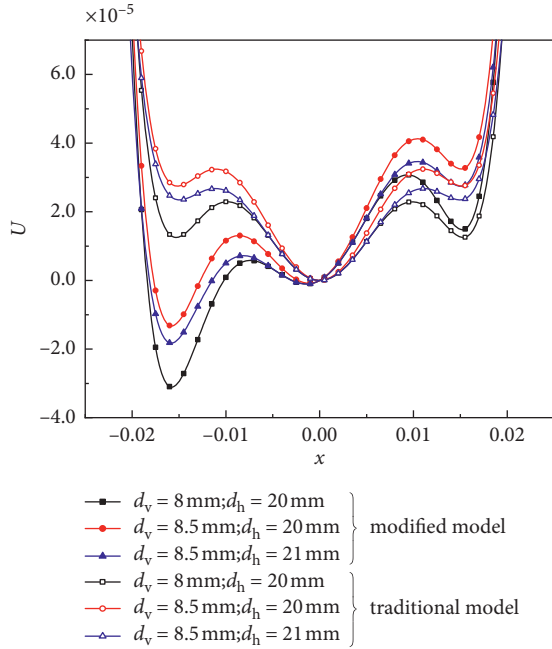


FIGURE 2: Tristable potential energy curve.

For the steady-state response, let the time derivatives in equations (32a) and (32b) be equal to zero, and square and add the resulting equations to obtain

$$\begin{aligned} c_5^2 a^{10} + 2c_4 c_5 a^8 + (c_4^2 - 2c_3 c_5) a^6 - 2c_3 c_4 a^4 \\ + (c_1^2 + c_3^2) a^2 - c_2^2 = 0 \end{aligned} \quad (33)$$

where the steady-state displacement response amplitude a can be obtained by equation (33). The steady-state solutions for the displacement and the voltage can then be expressed in the following form:

$$x(\tau) = a \cos(\omega\tau + \phi_0), \quad (34a)$$

$$\bar{V}(\tau) = u \cos(\omega\tau + \phi_0 + \varphi), \quad (34b)$$

where $u = \omega / \sqrt{\alpha^2 + \omega^2} a$ is the steady-state voltage response amplitude $\phi_0 = \arccos(c_1/c_3 - c_4 a^2 - c_5 a^4)$, and $\varphi = \arctan(\alpha/\omega)$.

The steady-state solutions of output power can be written as follows:

$$P = \frac{l^2 \theta_1^2 u^2}{C_p^2 R}. \quad (35)$$

The stability of the solution can be determined according to the Routh–Hurwitz method.

4. Results and Discussion

In this section, we discuss the magnet spacing, the mass of tip magnet, thickness ratio of piezoelectric layer and substrate, load resistance, and piezoelectric material on the performance of TPEH for two different computational models. The geometric and material properties are as

follows: $l = 75$ mm, $b = 20$ mm, $h_s = 0.2$ mm, $Y_s = 70$ Gpa, $\rho_s = 2700$ kg/m³, $M_t = 14.9 \times 10^{-3}$ kg, $M_A = M_B = M_C = 1.22 \times 10^6$ A/m, $V_A = V_B = V_C = 1 \times 10^{-6}$ m³, $\xi_1 = 0.01$. PZT-5A: $Y_p = 60.98$ Gpa, $\rho_s = 7750$ kg/m³, $d_{31} = -1.71 \times 10^{-10}$ C/N, $\epsilon_{33}^s = 1.33 \times 10^{-8}$ F/m. PZT-5H: $Y_p = 60.61$ Gpa, $\rho_s = 7500$ kg/m³, $d_{31} = -2.74 \times 10^{-10}$ C/N, and $\epsilon_{33}^s = 2.56 \times 10^{-8}$ F/m. Figures 3 and 4 depict variations of displacement and output power versus excited frequency for different magnet spacing, respectively, in which $M_t = 14.9$ g, $R = 300$ k Ω . Figures 3 and 4 show that the displacement and output power amplitude of the interwell motion increase while the bandwidth decreases as d_h increases for a fixed d_v . The amplitude of the intrawell motion displacement of the conventional model decreases as d_h increases, while the amplitude of the intrawell motion displacement of the modified model is not sensitive to changes in d_h . With the d_v increasing, the displacement and output power amplitude of the interwell motion decreases, while the bandwidth and intrawell motion displacement amplitude increases in the case of the fixed d_h . The trend of interwell power varies with the distance between magnets being the same for the conventional model and the modified model, but the peak power and interwell bandwidth of the two models differ significantly. Taking $d_v = 7.5$ mm, $d_h = 20$ mm and $d_v = 7.5$ mm, $d_h = 21$ mm as examples, when the modified model is adopted, the corresponding peak power of the two cases is increased by 10.4% and 10.8%, respectively, compared with that of the traditional model, and the corresponding interwell bandwidth is increased by 25.8% and 27.3%, respectively, compared with that of the traditional model.

Figures 5 and 6 give the displacement and output power frequency response curves for different tip magnet masses M_t when $d_v = 7.5$ mm, $d_h = 20$ mm, and $R = 300$ k Ω . Figure 5 shows that increasing the tip magnet mass M_t can significantly increase the peak displacement and interwell bandwidth. When the excited frequency is low, the displacement amplitude of the interwell motion increases with tip magnet mass M_t increasing for the conventional model case while there is no significant change in interwell motion displacement amplitude for the modified model. As can be seen from Figure 6, the interwell motion output power amplitude and peak power for both computational model cases increase significantly with M_t increasing. The peak power calculated by the modified model is 0.13 W and 0.23 W, when $M_t = 9.9$ g and $M_t = 14.9$ g, respectively, which is 21.2% and 7.4% higher than the peak power of the conventional model, and the interwell motion bandwidth of the modified model is 38.1% and 25.5% higher than that of the conventional model, respectively.

Figures 7 and 8 show the steady-state amplitude response curves of the interwell motion output voltage with the variation of the excited acceleration amplitude for different tip magnet masses M_t when excited frequency $\omega = 0.5$ and $\omega = 1$. Figures 7 and 8 show that there is an excited acceleration threshold, and when the TPEH is excited by an excited amplitude greater than this threshold, it can cross the potential barrier and enter the high energy orbit. The excited acceleration threshold of interwell motion decreases with the

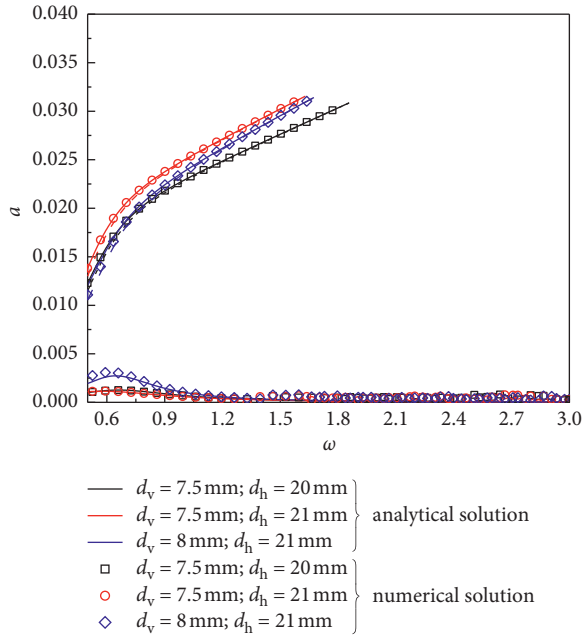


FIGURE 3: Displacement frequency response curve in different distance between three magnets.

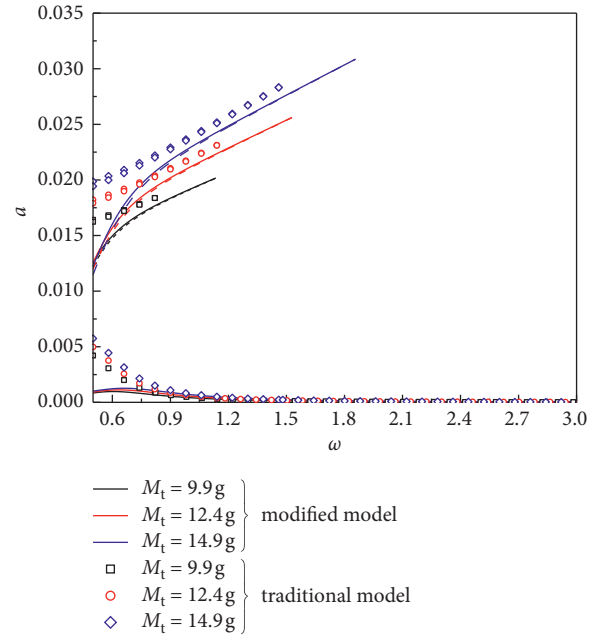


FIGURE 5: Displacement frequency response curve in different values of M_t .

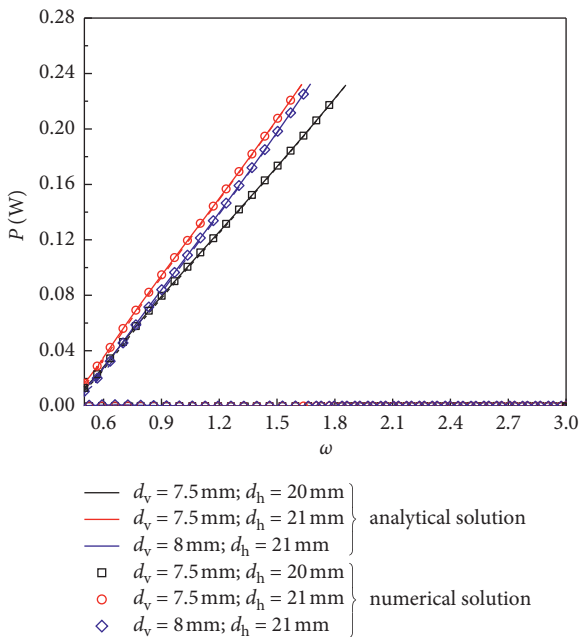


FIGURE 4: Power frequency response curve in different distance between three magnets.

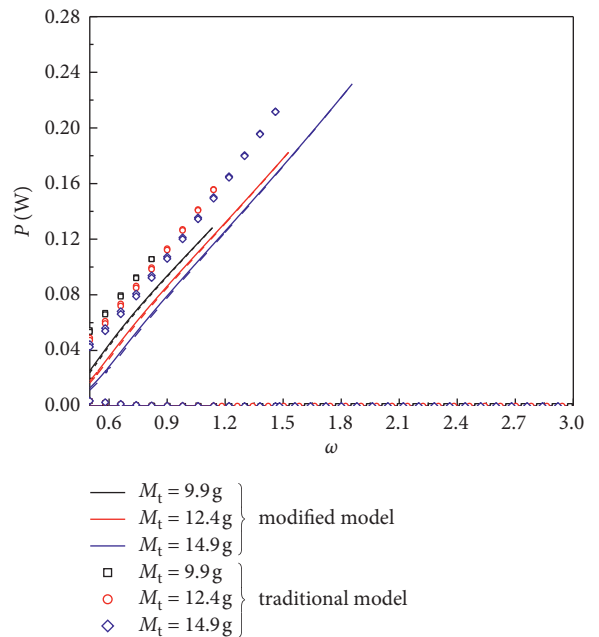


FIGURE 6: Power frequency response curve in different values of M_t .

increase of M_t when excited frequency $\omega = 0.5$ and $\omega = 1$. Compared to the conventional model, the modified model has a lower excitation acceleration threshold for interwell motion. In addition, the larger the excitation frequency, the larger the excitation acceleration amplitude required for the TPEH to generate interwell motion.

The variation of output power amplitude with load resistance for the two calculation models at low excited frequency is studied when $d_v = 7.5 \text{ mm}$, $d_h = 20 \text{ mm}$, and

$M_t = 14.9 \text{ g}$. Figure 9 shows that the output power amplitude at each excitation frequency tends to increase at the beginning and decrease afterwards with the increase of load resistance at each excited frequency. Each excitation frequency corresponds to an optimal load resistance to maximize the amplitude of output power of the TPEH, and the optimal load resistance decreases with the increase of excitation frequency. At lower excited frequencies (in the range of 0.6 to 1.1), the optimal load resistance of the modified model is higher than that of the conventional model, but the

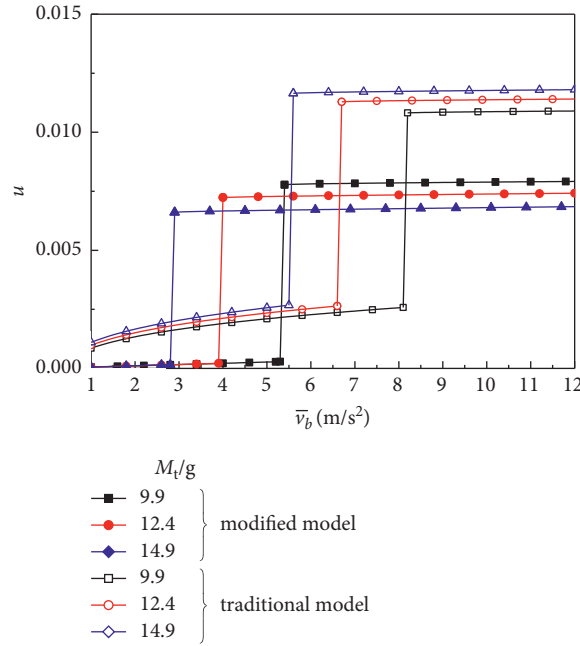


FIGURE 7: Voltage-excitation amplitude response curve in different values of M_t when $\omega = 0.5$.

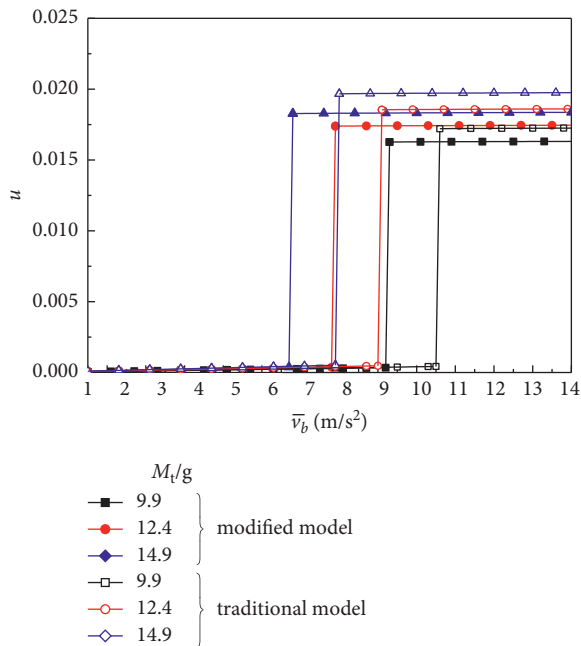


FIGURE 8: Voltage-excitation amplitude response curve in different values of M_t when $\omega = 1$.

corresponding peak power is significantly lower than that of the conventional model.

The effect of load resistance R on the peak displacement of the cantilever beam for two different piezoelectric materials (PZT-5A, PZT-5H) at $d_v = 7.5$ mm, $d_h = 20$ mm, and $M_t = 14.9$ g is shown in Figure 10. The results show that the load resistance R has little effect on the peak displacement of the system under the short circuit or open circuit conditions. The peak displacements of the two piezoelectric materials are

very similar to each other. The reason is that they have similar elastic modulus and density, the natural frequencies of short circuit and open circuit are close, and the flexibility under short circuit or open circuit resonance excitation is also very close.

Figure 11 depicts the peak power variation curve with load resistance R for the cantilever beam of two piezoelectric materials (PZT-5A, PZT-5H) when $d_v = 7.5$ mm, $d_h = 20$ mm, $M_t = 14.9$ g. The results show that the peak power of the system increases sharply with the increase of the load resistance (the first peak power maximum occurs, and the corresponding local optimal load resistance is R_{opt1}), then decreases slightly and continues to increase (the second peak power maximum occurs, and the corresponding local optimal load resistance is R_{opt2}), and then decreases gradually. Both local optimum load resistances of the PZT-5A cantilever beam are larger than those of the PZT-5H cantilever beam, but the maximum values of the system peak power with both piezoelectric materials are very close, due to the fact that the magnitude of the peak power depends on the flexibility of the piezoelectric cantilever beam. The peak power maximum values of the modified model for both piezoelectric materials are larger than those of the conventional model, and the corresponding local optimal load resistance R_{opt1} is larger than that of the conventional model, while R_{opt2} is smaller than that of the conventional model in both cases. Taking the PZT-5A cantilever beam as an example, the $R_{opt1} = 59K$ obtained by using the modified mode is 10.1% higher than that of the traditional model, and the $R_{opt2} = 281K$ is 21.6% lower than that of the traditional model. The maximum peak power of the modified model is 7% higher than that of the traditional model.

Figure 12 shows the variation curve of peak power of PZT-5A and PZT-5H cantilever beams with thickness ratio

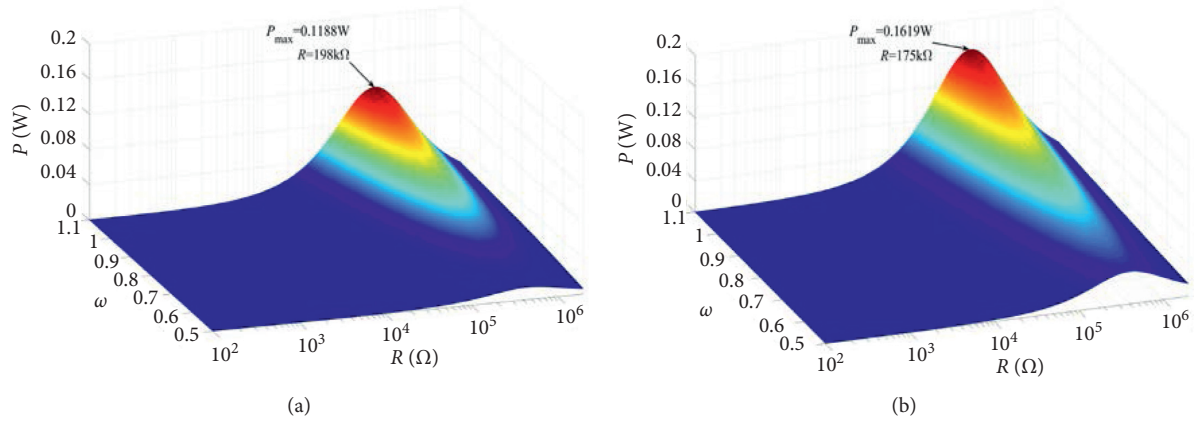


FIGURE 9: Output power amplitude response of the system with different load resistance: (a) modified model and (b) traditional model.

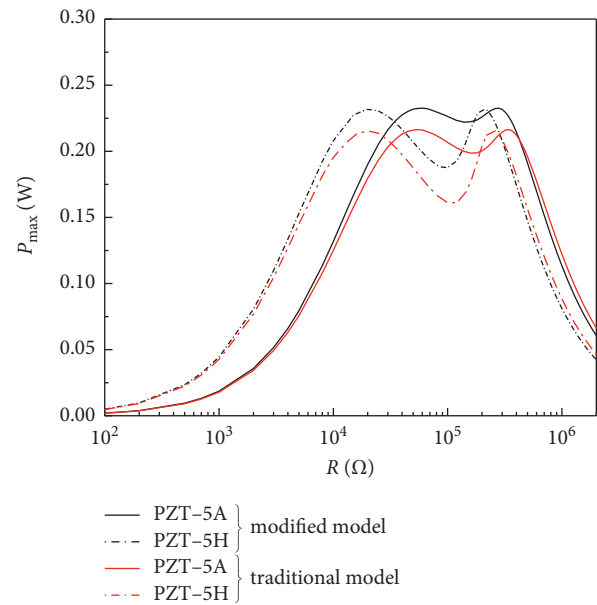
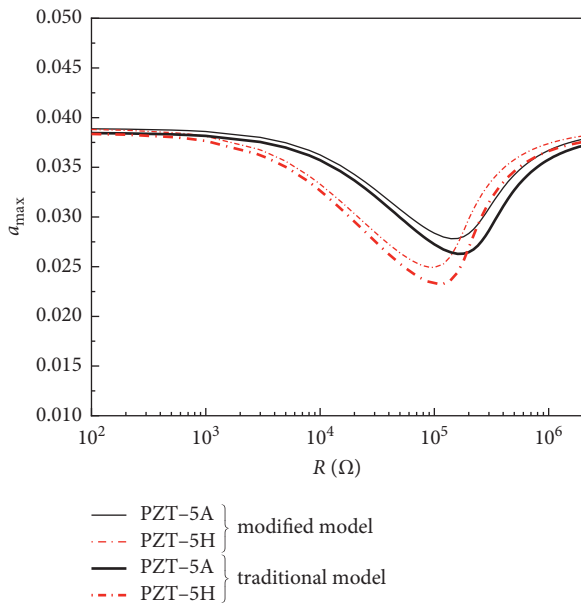


FIGURE 10: Peak displacement curves along with resistance change.

FIGURE 11: Peak power curves along with resistance change.

TP/HS of piezoelectric layer and substrate under the two calculation models when the thickness of piezoelectric beam ($2t_p + h_s$) is 0.6 mm. It can be seen from Figure 12 that the peak power of PZT-5A and PZT-5H cantilever beams under both calculation models show a trend of increasing sharply and then leveling off with the increase of t_p/h_s . Under the traditional model, when $t_p/h_s < 0.5$, the peak power of PZT-5H cantilever beam is significantly lower than that of PZT-5A cantilever beam; when t_p/h_s is between 0.5 and 1.1, the peak power of PZT-5H cantilever beam is slightly larger than that of PZT-5A cantilever beam. After that, with the continuous increase of t_p/h_s , the peak power of PZT-5H cantilever beam is lower than that of PZT-5A cantilever beam again. Under different piezoelectric materials, when t_p/h_s is small, the peak power obtained by the two models is close to each other, while when t_p/h_s exceeds a certain value, the peak

power obtained by the modified model is obviously higher than that obtained by the traditional model.

The optimal load resistance curves of PZT-5A and PZT-5H cantilever beams with two excitation frequencies ($\omega = 0.5, \omega = 0.5$) for $d_v = 7.5$ mm, $d_h = 20$ mm, $M_t = 14.9$ g, and piezoelectric beam thickness $2t_p + h_s = 0.6$ mm are given in Figure 13. It shows that the optimal load resistance of PZT-5A and PZT-5H cantilever beams under both calculation models decreases with increasing excited frequency and increases with increasing t_p/h_s , and the growth rate of optimal load resistance slows down with increasing t_p/h_s . The optimal load resistance of both calculated models is greater for the PZT-5A cantilever beam compared to the PZT-5H cantilever beam for the same excited frequency and t_p/h_s . Under the same conditions, the optimal load resistance of the modified model is larger than that of the conventional model.

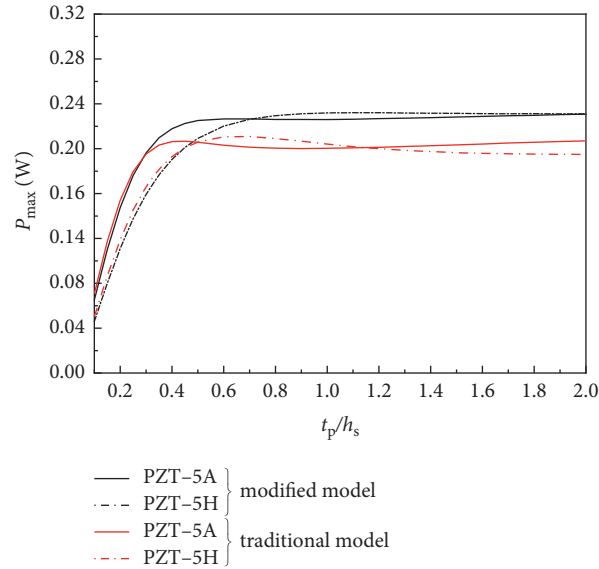


FIGURE 12: Peak power curves along with t_p/h_s change.

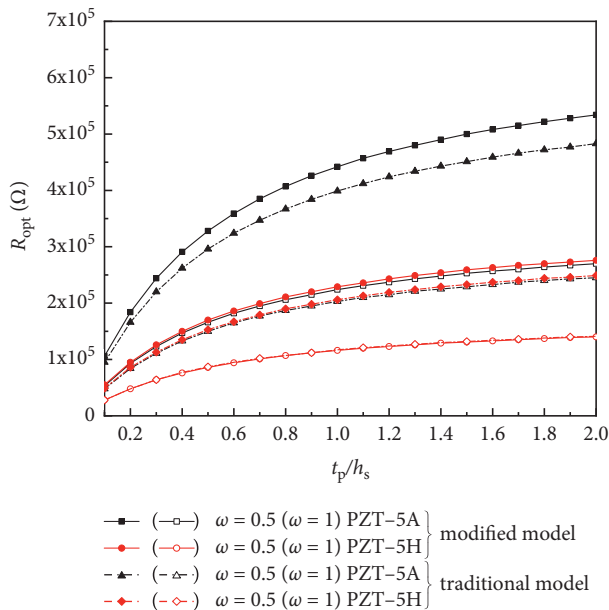


FIGURE 13: Optimal resistance curves along with t_p/h_s change.

5. Conclusions

In this paper, based on the generalized Hamilton variational principle, considering the gravity potential energy of the energy harvester, the size effect, and the rotary inertia of tip magnet, a more accurate electromechanical coupling equation of the nonlinear tristable piezoelectric cantilever energy harvester is obtained, and the analytical solution of the equation is obtained by using the multiscale method. The effects of magnet spacing, the mass of tip magnet, thickness ratio of piezoelectric layer and substrate, load resistance, and piezoelectric material on the performance of piezoelectric

energy capture system under the modified and conventional models were investigated and the following conclusions were obtained:

- (1) Increasing d_h or decreasing d_v can improve the interwell displacement and output power amplitude. The interwell bandwidth decreases with the increase of d_h and increases with the increase of d_v .
- (2) Increasing M_t can significantly increase the peak power and bandwidth of the system, but the excited acceleration threshold to generate interwell motion decreases with increasing M_t .
- (3) The maximum peak power of two piezoelectric cantilever beams (PZT-5A and PZT-5H) is very close. When t_p/h_s is very small or too large, the peak power of PZT-5A cantilever beam is slightly larger than that of PZT-5H cantilever beam, while when t_p/h_s is moderate, the peak power of PZT-5H cantilever beam is significantly larger than that of PZT-5A cantilever beam. The optimal load resistance of both piezoelectric material cantilever beams increases with t_p/h_s increasing. Under the same excited frequency and t_p/h_s , the optimal load resistance of PZT-5A cantilever beam is larger.
- (4) The effect on the optimal load resistance of the system is significant after introducing the gravitational potential energy of the TPEH, the eccentricity, and the rotational inertia of the tip magnet into the conventional calculation model. In addition, compared with the traditional model, the peak power and interwell motion bandwidth of the modified model are significantly increased. Therefore, it is of great significance to establish a modified model to improve the accuracy of predicting the energy harvesting efficiency of the TPEH.

Appendix

$$\begin{aligned}
 \kappa &= \frac{\mu M_A V_A M_B V_B}{4\pi} \\
 q_1 &= 2d_h^2 - d_v^3, \\
 q_2 &= \frac{(d_h e\varphi_1'(l)^2 + e^2 \varphi_1'(l)^2 + 2e\varphi_1(l)\varphi_1'(l) + \varphi_1(l)^2)}{(d_h^2 - d_v^3)}, \\
 q_3 &= \frac{d_v(e\varphi_1'(l) + \varphi_1(l))}{(d_h^2 - d_v^3)}, \\
 q_4 &= \frac{2d_v[(e\varphi_1'(l) + \varphi_1(l)) + 3d_h d_v \varphi_1'(l)]}{(d_h^2 - d_v^3)}, \\
 q_5 &= -0.5(2d_h^2 - d_v^3)\varphi_1'(l)^2 - (e\varphi_1'(l) + \varphi_1(l))^2 - d_h e\varphi_1'(l)^2 - 3d_h \varphi_1(l)\varphi_1'(l), \\
 q_6 &= \frac{(-0.75d_h e\varphi_1'(l)^4 - 0.75e^2 \varphi_1'(l)^4 - e\varphi_1(l)\varphi_1'(l)^3)}{(d_h^2 - d_v^3)}, \\
 q_7 &= \frac{d_v e\varphi_1'(l)^3}{(d_h^2 - d_v^3)}, \\
 q_8 &= -0.5[2d_v(e\varphi_1'(l) + \varphi_1(l)) + 3d_h d_v \varphi_1'(l)]\varphi_1'(l)^2 + 0.5d_v e\varphi_1'(l)^3, \\
 q_9 &= -0.375(2d_h^2 - d_v^3)\varphi_1'(l)^4 - [-(e\varphi_1'(l) + \varphi_1(l))^2 + 2d_h e\varphi_1'(l)^2 - 3d_h(e\varphi_1'(l) + \varphi_1(l))\varphi_1'(l)]\varphi_1'(l)^2 \\
 &\quad - 0.5e\varphi_1(l)\varphi_1'(l)^3, \\
 q_{10} &= \frac{(0.625d_h e\varphi_1'(l)^6 + 0.625e^2 \varphi_1'(l)^6 + 0.75e\varphi_1(l)\varphi_1'(l)^5)}{(d_h^2 - d_v^3)}, \\
 q_{11} &= \frac{d_v e\varphi_1'(l)^5}{(d_h^2 - d_v^3)}, \\
 q_{12} &= -0.375[2d_v(e\varphi_1'(l) + \varphi_1(l)) + 3d_h d_v \varphi_1'(l)]\varphi_1'(l)^4 - 0.625d_v e\varphi_1'(l)^5, \\
 q_{13} &= -0.313(2d_h^2 - d_v^3)\varphi_1'(l)^6 - 0.25e^2 \varphi_1'(l)^6 - 0.75e\varphi_1(l)\varphi_1'(l)^2 - 0.375\varphi_1(l)^2 \varphi_1'(l)^4, \\
 &\quad - 0.25d_h e\varphi_1'(l)^6 - 1.125d_h \varphi_1(l)\varphi_1'(l)^5 - 0.125e\varphi_1(l)\varphi_1'(l)^5.
 \end{aligned} \tag{A.1}$$

Data Availability

Requests for the data used to support the findings of this study will be considered by the corresponding author.

Conflicts of Interest

The authors declare that they have no conflicts of interest.

Acknowledgments

This research was funded by the Doctoral Startup Foundation of Anhui Jianzhu University (2020QDZ07, 2018QD28, and 2017QD05), the Natural Science Research Project of Higher Education Institutions in Anhui Province (KJ2019A0747 and KJ2019A0748), the Anhui Provincial Natural Science Foundation (grant no. 2008085QE245), the

Project of Science and Technology Plan of Department of Housing and Urban-Rural Development of Anhui Province (2020-YF15 and 2021-YF22), the ideological and political demonstration course for the Quality Engineering Project of Anhui Province (2020szsfkc0298), the ideological and political demonstration course of Anhui Jianzhu University (2020szkc05), and the research project of Anhui Agricultural University (rc412009).

References

- [1] Y. Zhang, C. S. Cai, and W. Zhang, "Experimental study of a multi-impact energy harvester under low frequency excitations," *Smart Materials and Structures*, vol. 23, no. 5, p. 055002, 2014.
- [2] M. Karimi, A. H. Karimi, R. Tikani, and S. Ziaei-Rad, "Experimental and theoretical investigations on piezoelectric-based energy harvesting from bridge vibrations under travelling vehicles," *International Journal of Mechanical Sciences*, vol. 119, pp. 1–11, 2016.
- [3] K. Takeya, E. Sasaki, and Y. Kobayashi, "Design and parametric study on energy harvesting from bridge vibration using tuned dual-mass damper systems," *Journal of Sound and Vibration*, vol. 361, pp. 50–65, 2016.
- [4] X. D. Xie and Q. Wang, "Design of a piezoelectric harvester fixed under the roof of a high-rise building," *Engineering Structures*, vol. 117, pp. 1–9, 2016.
- [5] A. Erturk and D. J. Inman, "An experimentally validated bimorph cantilever model for piezoelectric energy harvesting from base excitations," *Smart Materials and Structures*, vol. 18, no. 2, p. 25009, 2009.
- [6] L. Tang and J. Wang, "Size effect of tip mass on performance of cantilevered piezoelectric energy harvester with a dynamic magnifier," *Acta Mechanica*, vol. 228, no. 11, pp. 3997–4015, 2017.
- [7] C. R. McInnes, D. G. Gorman, and M. P. Cartmell, "Enhanced vibrational energy harvesting using nonlinear stochastic resonance," *Journal of Sound and Vibration*, vol. 318, no. 4–5, pp. 655–662, 2008.
- [8] H. Qing, S. Jeong, S. Y. Jeong, T. H. Sung, and H. H. Yoo, "Investigation of the energy harvesting performance of a Lambda-shaped piezoelectric energy harvester using an analytical model validated experimentally," *Smart Materials and Structures*, vol. 30, no. 7, p. 75017, 2021.
- [9] G.-Q. Wang and Y.-M. Lu, "An improved lumped parameter model for a piezoelectric energy harvester in transverse vibration," *Shock and Vibration*, vol. 2014, Article ID 935298, 12 pages, 2014.
- [10] J. Jung, P. Kim, J.-I. Lee, and J. Seok, "Nonlinear dynamic and energetic characteristics of piezoelectric energy harvester with two rotatable external magnets," *International Journal of Mechanical Sciences*, vol. 92, pp. 206–222, 2015.
- [11] A. H. Hosseinloo and K. Turitsyn, "Non-resonant energy harvesting via an adaptive bistable potential," *Smart Materials and Structures*, vol. 25, no. 1, pp. 15010–15018, 2015.
- [12] K. Fan, Q. Tan, Y. Zhang, S. Liu, M. Cai, and Y. Zhu, "A monostable piezoelectric energy harvester for broadband low-level excitations," *Applied Physics Letters*, vol. 112, no. 12, p. 123901, 2018.
- [13] A. Kumar, S. F. Ali, and A. Arockiarajan, "Exploring the benefits of an asymmetric monostable potential function in broadband vibration energy harvesting," *Applied Physics Letters*, vol. 112, no. 23, p. 123901, 2018.
- [14] A. Erturk, J. Hoffmann, and D. J. Inman, "A piezomagnetoelastic structure for broadband vibration energy harvesting," *Applied Physics Letters*, vol. 94, no. 25, p. 254102, 2009.
- [15] A. Erturk and D. J. Inman, "Broadband piezoelectric power generation on high-energy orbits of the bistable Duffing oscillator with electromechanical coupling," *Journal of Sound and Vibration*, vol. 330, no. 10, pp. 2339–2353, 2011.
- [16] G. Litak, M. I. Friswell, and S. Adhikari, "Magnetopiezoelectric energy harvesting driven by random excitations," *Applied Physics Letters*, vol. 96, no. 21, p. 214103, 2010.
- [17] P. Firoozy, S. E. Khadem, and S. M. Pourkiaee, "Broadband energy harvesting using nonlinear vibrations of a magnetopiezoelectric cantilever beam," *International Journal of Engineering Science*, vol. 111, pp. 113–133, 2017.
- [18] T. Yang and Q. Cao, "Dynamics and performance evaluation of a novel tristable hybrid energy harvester for ultra-low level vibration resources," *International Journal of Mechanical Sciences*, vol. 156, pp. 123–136, 2019.
- [19] T. Yang and Q. Cao, "Dynamics and energy generation of a hybrid energy harvester under colored noise excitations," *Mechanical Systems and Signal Processing*, vol. 121, pp. 745–766, 2019.
- [20] P. Kim, D. Son, and J. Seok, "Triple-well potential with a uniform depth: advantageous aspects in designing a multistable energy harvester," *Applied Physics Letters*, vol. 108, no. 24, p. 243902, 2016.
- [21] S. C. Stanton, C. C. McGehee, and B. P. Mann, "Nonlinear dynamics for broadband energy harvesting: investigation of a bistable piezoelectric inertial generator," *Physica D: Nonlinear Phenomena*, vol. 239, no. 10, pp. 640–653, 2010.
- [22] W. Tang, X. Wang Xiao-Pu, and J. Cao Jing-Jun, "Modeling and analysis of piezoelectric vibration energy harvesting system using permanent magnets," *Acta Physica Sinica*, vol. 63, no. 24, p. 240504, 2014, in Chinese.
- [23] P. Kim, Y.-J. Yoon, and J. Seok, "Nonlinear dynamic analyses on a magnetopiezoelectric energy harvester with reversible hysteresis," *Nonlinear Dynamics*, vol. 83, no. 4, pp. 1823–1854, 2016.
- [24] W. Wang, J. Cao, C. R. Bowen, Y. Zhang, and J. Lin, "Nonlinear dynamics and performance enhancement of asymmetric potential bistable energy harvesters," *Nonlinear Dynamics*, vol. 94, no. 2, pp. 1183–1194, 2018.
- [25] P. Zhu, X. Ren, W. Qin, Y. Yang, and Z. Zhou, "Theoretical and experimental studies on the characteristics of a tristable piezoelectric harvester," *Archive of Applied Mechanics*, vol. 87, no. 9, pp. 1541–1554, 2017.
- [26] H. Li, W. Qin, C. Lan, W. Deng, and Z. Zhou, "Dynamics and coherence resonance of tristable energy harvesting system," *Smart Materials and Structures*, vol. 25, p. 015001, 2016.
- [27] M. Panyam and M. F. Daqaq, "Characterizing the effective bandwidth of tristable energy harvesters," *Journal of Sound and Vibration*, vol. 386, pp. 336–358, 2017.
- [28] P. Kim and J. Seok, "Dynamic and energetic characteristics of a tristable magnetopiezoelectric energy harvester," *Mechanism and Machine Theory*, vol. 94, pp. 41–63, 2015.
- [29] Y. Leng, D. Tan, J. Liu, Y. Zhang, and S. Fan, "Magnetic force analysis and performance of a tristable piezoelectric energy harvester under random excitation," *Journal of Sound and Vibration*, vol. 406, pp. 146–160, 2017.